PROBING MECHANICAL AND CHEMICAL PROPERTIES OF BIOLOGICAL MATERIALS BY MULTIPLE MODALITIES

by

Tuna Pesen İnanç

B.S., Physics, Boğaziçi University, 2014

M.S., Physics, Boğaziçi University, 2016

Submitted to the Institute for Graduate Studies in
Science and Engineering in partial fulfillment of
the requirements for the degree of
Master of Science

Graduate Program in Physics

Boğaziçi University

2022

ACKNOWLEDGEMENTS

I would like to express my gratitude to my Ph.D. advisor Mehmet Burçin Ünlü for providing me an opportunity to study in his high-tech research laboratory and his friendly attitude towards me. I would also like to thank him for teaching me to orchestrate my research independently after having some experiences through my Ph.D.

I would like to acknowledge TUBITAK (Project No: 1003-118S113) and Bogazici University Higher Education Council Scientific Research Projects (Project No: 18143D) for providing me research grants through my studies.

I would like to thank all the group members of BUMILAB for their friendship and kind attitudes towards me.

Finally, I would like to thank my family for their unconditional support and love.

ABSTRACT

PROBING MECHANICAL AND CHEMICAL PROPERTIES OF BIOLOGICAL MATERIALS BY MULTIPLE MODALITIES

Mechanical and chemical alterations are the signature of most diseases, such as endometriosis, sickle cell, malaria, and cancer. Detecting such alterations has vital importance for early diagnosis and efficient treatments. In the first project, we aimed to establish a non-invasive diagnostic technique for endometriosis disease by detecting chemical changes in blood serum using Raman spectroscopy and machine learning algorithms. We measured 49 endometriosis patients' and 45 healthy women's blood sera for this project. A diagnostic tool was built-up by applying machine learning algorithms (kNN and SVM) to the Raman spectral data. The results of this study indicated diagnosis sensitivity and specificity values of 80.5% and 89.7%, respectively. In the following study, we investigated the effect of repetitive bi-axial stretch-relaxation cycles on the individual erythrocyte cells with optical tweezers to assess their mechanical response. According to the findings, the cells became stiffer with each stretch and became completely undeformable after several stretch-relaxation cycles. Also, we showed that stiffness changes with each stretching cycle as a sign of weak power law. Therefore, we showed that cell rheology is scale-free at a single and whole-cell level for the first time. In the last project, we studied the camel erythrocytes compared to the human erythrocytes in their mechanochemical features since camel erythrocytes have the most distinctive cell features among the vertebrates. Using optical tweezers, we quantified that camel erythrocytes are almost ten times more rigid than human erythrocytes. The chemical analysis by the Raman spectroscopy revealed the difference in the lipid:protein ratio of these two cell types.

ÖZET

BİYOLOJİK MALZEMELERİN MEKANİK VE KİMYASAL ÖZELLİKLERİNİN ÇEŞİTLİ MODALİTELERLE İNCELENMESİ

Mekanik ve kimyasal değişiklikler çoğu hastalığın imzasıdır, bunların arasında endometriozis, orak hücre, sıtma ve kanser sayılabilir. Bu tür değişikliklerin tespit edilmesi erken teşhis ve etkin tedavi uygulanması açısından hayati önem taşımaktadır. İlk projemizde Raman spektroskopisini kullanarak endometriosis hastalarının kan serumundaki kimyasal değişiklikleri saptadık ve bu hastalığa noninvaziv bir teşhis metodu geliştirdik. Ayrıca Raman spektral analizine makina öğrenmesi algoritmalarından olan kNN ve SVM uygulayarak teşhis başarısını daha da geliştirdik.

Bir sonraki projemizde, eritrositlere optik cımbız kullanarak tekrarlı gerdirme uyguladık ve bu hücrelerin mekanik davranışlarındaki değişimleri inceledik. Bulgularımıza göre, hücreler her bir esneme döngüsünden sonra daha da katılaştı ve belirli sayıda gerdirmeye maruz kaldıktan sonra tamamen esnekliğini yitirdi. Böylelikle, hücrelerde tekrarlı esnemeye bağlı deformabilitenin zayıf üstel değişimi gösterilmiş ve hücre reolojisinin ölçeksiz olduğu ilk kez bütün bir hücre düzeyinde ortaya konulmuştur.

Son projemizde ise memeliler içinde en farklı eritrosit özelliklerine sahip olan deve eritrositlerinin insan eritrositlerine kıyasla mekanik ve kimyasal özlelliklerinin ne gibi farklılıklar gösterdiğini araştırdık. Çalışmamızın sonucunda, deve hücrelerinin insana hücrelerine kıyasla on kat daha sert olduğunu gözlemledik. Ayrıca Raman spektral analizleri sonucunda insan ve deve eritrositlerinde lipid:protein oranlarının farklı olduğunu tespit ettik.

TABLE OF CONTENTS

LIST OF FIGURES

LIST OF TABLES

LIST OF SYMBOLS

a	Particle size
E	Electrical Field
E_0	Amplitude of Electrical Field
E_1	Energy of the ground state
E_2	Energy of the excited state
c	Speed of light
F_{gr}	Gradient force
F_{sc}	Scattering force
G'_n	Stiffness
h	Hysteresivity
n	Refractive index of a medium
n_p	Refractive index of a particle
P	Dipole moment
R	Reflection coefficient
S	Poynting vector
t	Time
T	Transmission coefficient
x	Displacement
x_0	Amplitude of the displacement
α	Wavelenght electric dipole polarizability
α_0	Polarizability at the equilibrium
ϵ_0	permittivity of free space
θ_{in}	Incident angle
θ_{sc}	Refraction angle
λ	Wavelenght
λ_{AS}	Wavelenght of anti-Stokes Scattering
λ_R	Wavelenght of Rayleigh Scattering
λ_S	Wavelenght of Stokes Scattering

λ_{laser}	Wavelenght of the laser
λ_{scat}	Wavelenght of the scattered light
$\tilde{\nu}$	Spectroscopic wavenumber
ν_0	Frequency of the laser
ν_m	Vibration frequency of a molecule
π	Pi number

LIST OF ACRONYMS/ABBREVIATIONS

AFM	Atomic force microscopy
BG	Background corrected spectrum
BC	Baseline corrected spectrum
BSA	Bovine serum albumin
DI	Deformability index
2D	Two dimensional
GUI	Graphical user interface
FN	False negative
FP	False positive
FWD	Free working distance
kNN	k-Nearest neighbor
MFD	Maximum Feret diameter
NPV	Negative predicted value
PBS	Phosphate-buffered saline
PCA	Principal component analysis
PPV	Positive predicted value
RBC	Red blood cell
RS	Raman scattering wawenumber
SVM	Support vector machines
TN	True negative
TP	True positive

1. INTRODUCTION

1.0.1. An Overview of Cell Mechanics Studies

Biophysical researches in different fields are crucial for understanding disease mechanisms. Especially cell mechanics studies, together with spectroscopic studies, are essential for relating the mechanical and chemical alterations with each other to discern how diseases progress in the body and what may be possible cures. Cells are complex organisms having, in most cases, organelles and a nucleus in the cytoplasm and covered by a cell membrane, which is responsible for regulating cells' osmotic and hydrostatic pressures by exchanging matter in and out of cells. Cell activities can not fall apart as mechanical and chemical interactions for such complex organisms. Instead, chemical alterations trigger some mechanical activities or vice versa. For instance, the hydrostatic pressure of cells is higher inside, and such a hydrostatic pressure difference mostly balances the protein meshwork embedded in the cell membrane. When this difference alters, the membrane tension changes. This difference triggers the opening/-closing of the ion channels and pumps on the membrane for re-adjusting the osmotic pressure and the membrane tension. Similarly, when a cell is exposed to mechanical stress, the hydrostatic pressure difference of the cell changes, and by the exact mechanism, the osmotic pressure is re-adjusted [1].

In most cases, diseases come with mechanical and chemical abnormalities in the related cells. For example, in sickle cell disease, red blood stiffness increases [2, 3], or in type 2 diabetes mellitus disease, red blood cells are found to be more deformable compared to healthy cells [4]. Such changes in cells' mechanical features can be detectable with different techniques, for example optical [4,5], and magnetic tweezers [6], atomic force microscopy (AFM) [7,8], scanning acoustic microscope (SAM) [9], Raman spectroscopy [10, 11], and acoustic force spectroscopy [12, 13]. In addition to detecting biomarkers of diseases for diagnosis, it is crucial to unveil the mechanical principles behind the scenes of the diseases. Before that, understanding healthy cells' mechanical behaviors is the first place we should look at. For this attempt, up until now,

different models to understand cells' mechanical behaviors have been established, such as power-law models [14, 15], soft glassy material models [16, 17], spring and dashpot models [18, 19], and dynamic cytoskeletal filament networks models [17]. Power-law models imply that there exist no characteristic relaxation times for dynamics of the cytoskeleton regulation after mechanical perturbation [14,15]. Rather, relaxation times distributes as a power-law (Figure 1.1a). Soft glassy material models explain that during the cytoskeletal rearrangement after mechanical perturbation, cytoskeletal elements are trapped in energy wells since thermal energy is not enough for the rearrangement (Figure 1.1b). Remodeling occurs when escaping from the energy well [16, 17]. According to the spring and dashpot models (Figure 1.1c), the viscous part of the cells is thought of as dashpots, whereas the elastic parts are thought of as springs [18, 19]. Hence, the viscoelastic behaviors of cells can be simulated. Single cytoskeletal filaments studies showed that the ability to sustain mechanical stress of the complex cytoskeletal network is not the sum of all the filaments' strength (Figure 1.1d). Rather, all the interactions of the filaments should be concerned dynamically to describe the cytoskeleton activities. Cell rheology is determined by this dynamic network of cytoskeletal filaments [17].

Since biological processes are mainly about protein interactions, it is important to link the mechanical processes with the protein interactions, which are generally chemical processes. For this purpose, spectroscopy measurements have vital importance in gathering information about the chemical content of the inspected sample. Since the molecular structures are built on chemical bonds of elements, physical interventions to these bonds, such as electromagnetic waves, cause detectable signals specific to the molecular contents. Hence these specific signals are used to get information about the chemical constituents of the sample.

In this thesis, Raman spectroscopy and optical tweezers were used for disease diagnostics and cell mechanics studies. The detailed theories of these two techniques can be found in the following sections.

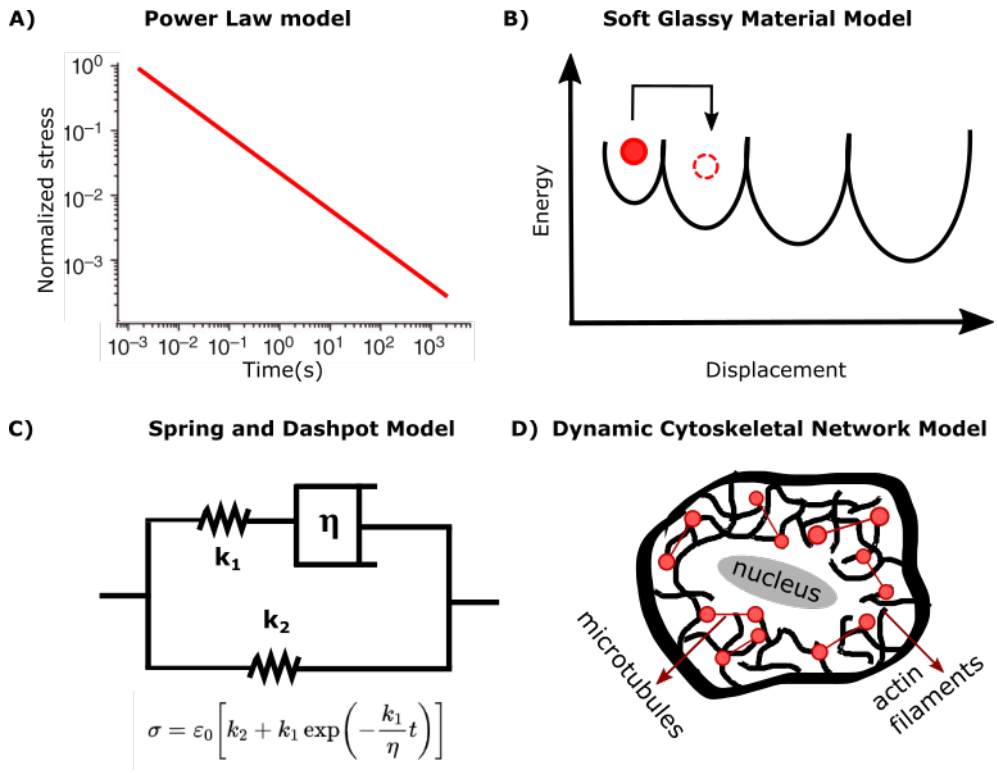

Figure 1.1. Different cell models for explaining mechanical cell behaviors; a) power law model, b) soft glassy material model, c) spring and dashpot model, d) dynamic cytoskeletal network model.

1.1. Raman Spectroscopy

Sir Chandrasekhara Venkata Raman is a Nobel laureate for his discovery of Raman scattering. His work showed that when light interacts with molecular vibrations, it causes a change in the wavelength of the light [20]. In his article, he stated his discovery as "*A new radiation*" [21, 22].

In his work in 1928, he used sunlight as a light source and just his eyes as a detector. As demonstrated in Figure 1.2, he illuminated a liquid sample with sunlight through a microscope objective and placed a violet filter before the sample. He placed a green filter after the sample and saw a green light. He explained the difference between this radiation and fluorescence radiation by drawing attention to the intensity and polarization of this light. He elucidates that the intensity of this "new radiation" is in a different order, and it is polarised. Usually, the fluorescent radiation is unpolarized,

so this observed light scattering was recorded as a new type of radiation, later as *Raman scattering*.

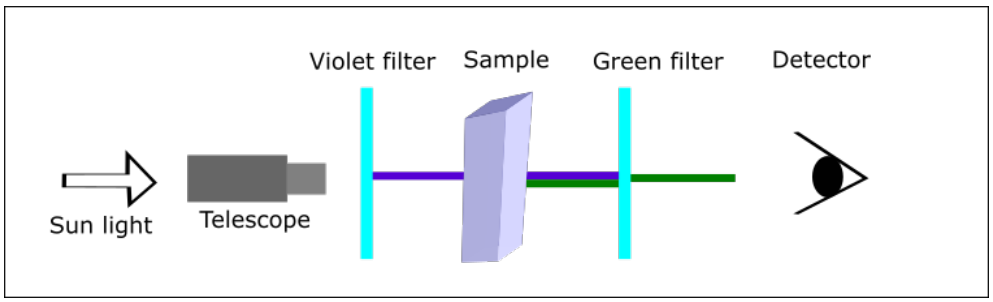

Figure 1.2. Demonstration of the experimental setup, which shows the discovery of Raman scattering.

1.1.1. Jablonski Diagram

The Jablonski diagram, given in Figure 1.3, is a visual representation of the possible transitions that may occur when a molecule has been excited by light. In this figure, energy levels of a molecule are symbolized by solid black lines, and the virtual states are symbolized with dashed black lines. The energy of the states increases from bottom to top on the diagram. The lowest vibrational the energy levels of the electronic states are shown by bold lines, whereas the higher levels are represented by thinner lines. From bottom to top, more closely spaced energy levels show the trend going towards the continuum energy levels. With respect to the total spin angular momentum of the states, the electronic states are called *singlet (S)* or *triplet (T)* states. The singlet state corresponds to the case when the total spin angular momentum is zero. The triplet state corresponds to the case when total spin angular momentum is one.The transitions shown in the diagram correspond to different processes. For example, Rayleigh scattering is form of an elastic scattering of light or any other electromagnetic radiation from a particle having size less than $\sim 1/10$ the wavelength of the radiation. The interacted particles can be atoms or molecules. Raman scattering happens when light or any other electromagnetic radiation inelastically scatters from the particle, which may be atoms, electrons, and molecules. Absorption is a radiative

transition of a molecule from lower to higher electronic states. In this case, the absorbed energy of photons by a molecule is turned into the internal energy of the molecule. Fluorescence and phosphorescence are both radiative transitions. Fluorescence occurs between two electronic states with the same spin multiplicity whereas Phosphorescence happens between two electronic states which have different spin multiplicities.

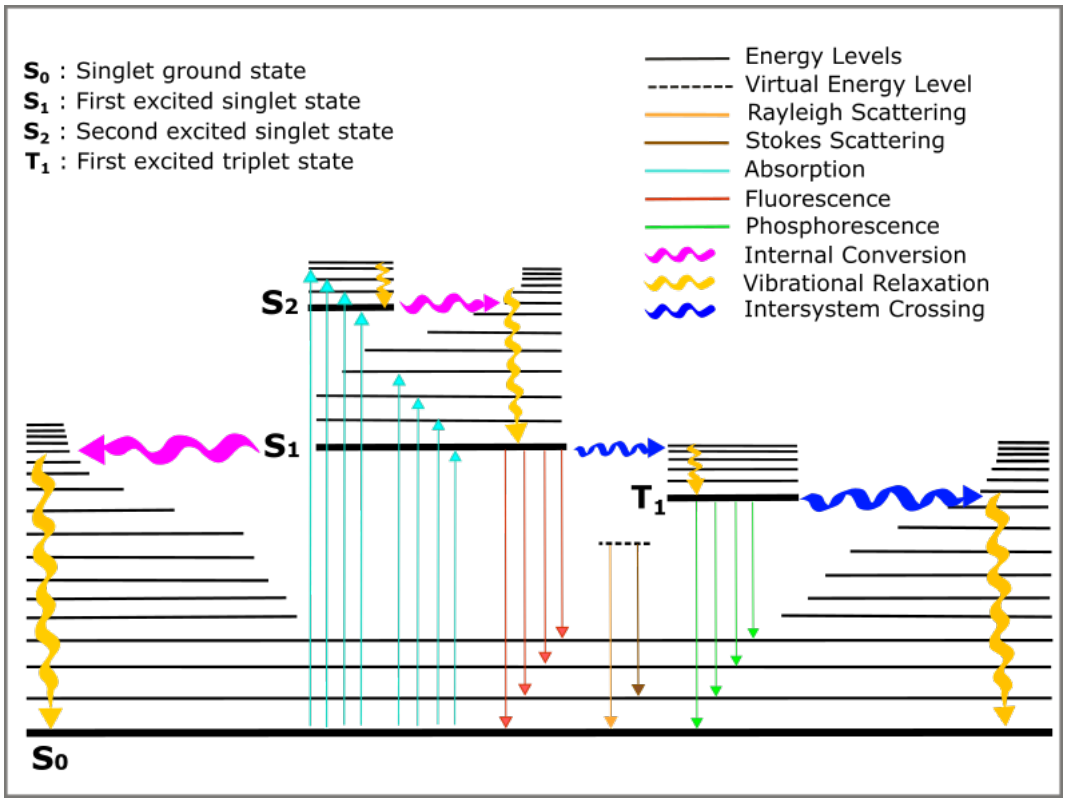

Figure 1.3. Jablonski diagram shows the possible energy transitions between the energy levels of a molecule excited by light corresponding the specific events.

Raman scattering is a radiative process that is seen between a virtual state and a ground electronic state. Internal conversion is a type of non-radiative transition that is seen between two electronic states having the same spin multiplicities. Vibrational relaxation is a non-radiative transition towards a lower vibrational energy level within the same electronic state. The intersystem crossing is a non-radiative transition between two isoenergetic vibrational levels of the same electronic states with different spin multiplicities.

1.1.2. Classical theory of Raman Scattering

From the point of classical theory, Raman scattering can be understood in the following. Let there be a laser light with the electric field, E, oscillating in time, t:

$$E = E_0 \cos 2\pi v_0 t, \tag{1.1}$$

where E_0 is the amplitude and ν_0 is the frequency of the laser. When a diatomic molecule exposed to such a laser light, a dipole moment, P, is induced:

$$P = \alpha E = \alpha E_0 \cos 2\pi v_0 t, \tag{1.2}$$

where α is the electric dipole polarizability. In the case of the molecule is vibrating with a frequency ν_m, the displacement from the equilibrium position, x, can be written as follows:

$$x = x_0 \cos 2\pi v_m t, \tag{1.3}$$

where x_0 is the amplitude of the displacement. If the amplitude of the vibration is small α can be taken as a linear function of x, using Maclaurin expansion, as in the following:

$$\alpha = \alpha_0 + \left(\frac{\partial \alpha}{\partial x}\right)_0 x_0 + \ldots, \tag{1.4}$$

where α_0 is the polarizability of the molecule at the equilibrium. If we combine Equation (1.2), Equation (1.3) and Equation (1.4), the dipole moment, P, can be written as

$$\begin{aligned} P &= \alpha E_0 \cos 2\pi v_0 t, \\ &= \alpha_0 E_0 \cos 2\pi v_0 t + \left(\frac{\partial \alpha}{\partial x}\right)_0 x E_0 \cos 2\pi v_0 t, \\ &= \alpha_0 E_0 \cos 2\pi v_0 t + \left(\frac{\partial \alpha}{\partial x}\right)_0 x_0 E_0 \cos 2\pi v_0 t \cos 2\pi v_m t, \\ &= \underbrace{\alpha_0 E_0 \cos 2\pi v_0 t}_{\text{Rayleigh scattering}} + \underbrace{\frac{1}{2}\left(\frac{\partial \alpha}{\partial x}\right)_0 x_0 E_0 \left[\cos\left\{2\pi\left(v_0 + v_m\right)t\right\} + \cos\left\{2\pi\left(v_0 - v_m\right)t\right\}\right]}_{\text{Raman scattering}}. \end{aligned} \tag{1.5}$$

In classical theory, the first term in Equation (1.5) indicates Rayleigh scattering, which is due to the oscillating dipole, and the second term shows Raman scattering at the frequencies of $\nu_0 + \nu_m$ (anti-Stokes) and $\nu_0 - \nu_m$ (Stokes). Therefore, in Raman

spectroscopy, we measure the vibrational frequency, ν_m, of a molecule as a shift from the incident beam frequency ν_0. In terms of wavelength, Anti-Stokes scattering wavelength, λ_{AS}, is smaller than Rayleigh scattering wavelength, and Stokes scattering wavelength, λ_S, is greater than the Rayleigh scattering wavelength. Regarding how much the wavelength differs from the incident light's wavelength, Raman shift is calculated, as shown in Figure 1.4.

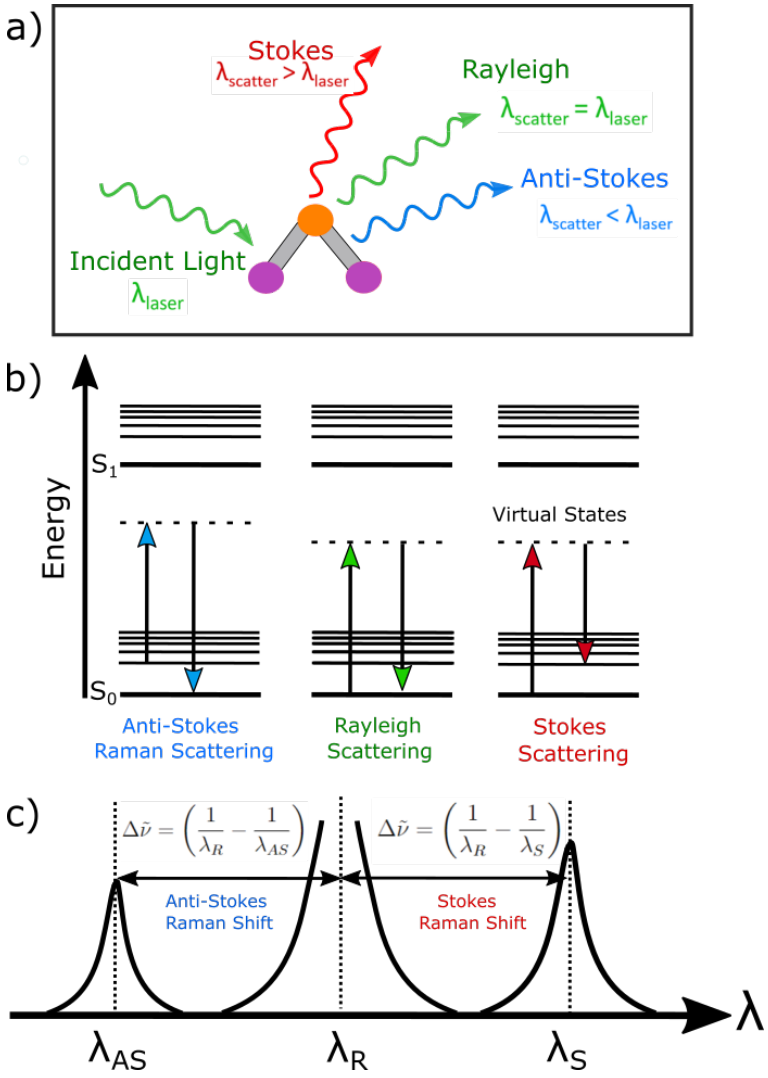

Figure 1.4. Stokes, anti-Stokes, and the Rayleigh scattering mechanisms. The wavelength of anti-Stokes scattering λ_{AS}, is less than the wavelength Rayleigh scattering λ_R, whereas the wavelength of Stokes scattering, λ_S, is greater than the wavelength Rayleigh scattering.

1.1.3. Calculation of Raman Shifts

When a molecule interacts with an electromagnetic field, energy transfer from the electromagnetic field to the molecule occurs according to the Bohr's frequency condition which is

$$\Delta E = E_2 - E_1 = h\nu, \tag{1.6}$$

where E_1 and E_2 are the energies of the ground and the excited states, respectively, h is Planck's constant, and ν is the frequency of the electromagnetic wave. We can write ν in terms of the speed of light, c, and the wavelength of the electromagnetic wave, λ, as follows:

$$\nu = \frac{c}{\lambda}. \tag{1.7}$$

If we rewrite the Equation (1.6) we have:

$$\begin{aligned} h\nu &= h\nu_1 - h\nu_2, \\ &= \frac{hc}{\lambda_2} - \frac{hc}{\lambda_1}. \end{aligned} \tag{1.8}$$

We can define a parameter called *spectroscopic wavenumber*, $\tilde{\nu}$ as follows:

$$\tilde{\nu} = \frac{\nu}{c} = \frac{1}{\lambda}, \tag{1.9}$$

so that the Equation (1.8) becomes:

$$\Delta\tilde{\nu} = \frac{1}{\lambda_2} - \frac{1}{\lambda_1}. \tag{1.10}$$

Hence, the Raman shifts, $\Delta\tilde{\nu}$, correspond to the vibrational frequencies of the molecules irradiated by a laser and can be calculated in terms of the laser (λ_{laser}) and the scattered (λ_{scat}) lights' wavelengths as

$$\Delta\tilde{\nu} = \frac{1}{\lambda_{laser}} - \frac{1}{\lambda_{scat}}. \tag{1.11}$$

1.1.4. Raman Scattering in Polyatomic Molecules

In the case of polyatomic molecules, overall vibrations of a molecule can be expressed in terms of a superposition of normal vibrations. For example, an N-atom molecule has 3N degrees of freedom of motion because each atom can move in three directions (x,y,z). Among these 3N degrees, 3 degrees are from translational motions

and 3 degrees are from the rotational motions of the entire molecule about the three major axes of rotation, which pass through the center of gravity. As a result, the net number of normal vibrational degrees of freedom becomes 3N-6. If the molecule has a linear geometry then there is no rotation about the molecular axis, so the total degrees of freedom becomes 3N-5.

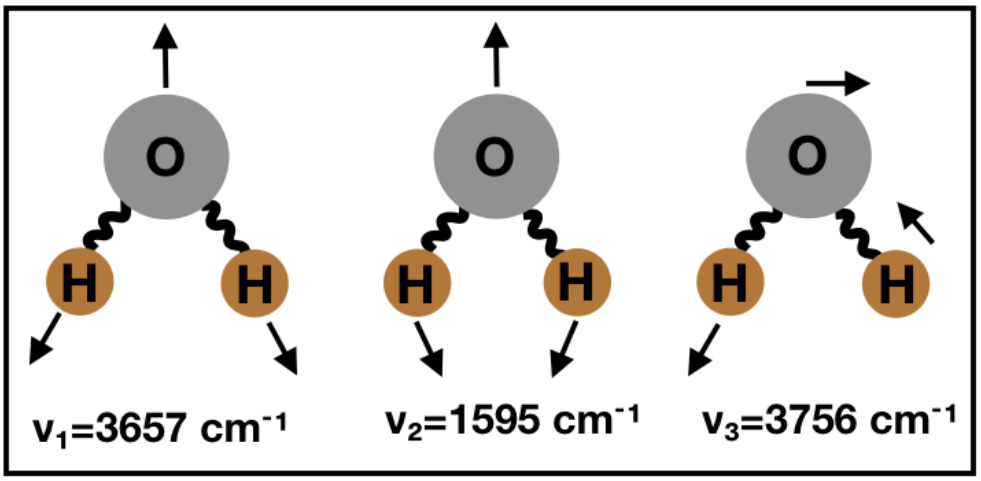

Figure 1.5. Normal vibrational modes of H_2O. Arrows show the directions of the vibrations.

1.1.5. Intensity of Stokes and anti-Stokes Scattering

Since Raman scattering is about molecular vibration, the intensity ratio of Stokes and anti-Stokes light depends on temperature. Accordingly, it is related to the number of molecules in the ground and the excited state. As shown in Figure 1.4b, the intensity of anti-Stokes scattering is proportional to the number of molecules in the ground state, whereas the intensity of Stokes scattered light is proportional to the number of molecules in the excited state. Since the number of molecules is greater in the ground state than in the excited state, the intensity of Stokes-scattered light is higher than the anti-Stokes-scattered light, as indicated in Figure 1.4c. In general, the intensity of Stokes and anti-Stokes scattered light is the 10^{-6} of the Rayleigh scattered light, which is very weak [23].

1.2. Optical Tweezers

Arthur Ashkin was the founder of the optical trapping technique in 1970 and was awarded the Nobel Prize in Physics in 2018 for his discovery [24]. He realized that using the radiation pressure of light, micron-sized neutral particles in liquids and gas can be trapped in stable optical potential wells created by lasers [24].

With the conventional optical tweezers, atoms, molecules, submicron particles and dielectric particles at a micrometer level in size can be optically trapped, and forces at the piconewton level can be measured [25, 26]. The mechanism underlying this technique is one of the fundamental laws of physics, the law of conservation of momentum. [27]. When light passes through a different medium, its path refracts, which causes a change in the momentum of the light. By the conservation of the momentum law, the difference in the light's momentum is picked up by the medium. If this medium is a dielectric object, then the particle can be moved or manipulated.

There are two kinds of forces on the bead due to the light interaction; scattering, and the gradient force. Scattering force occurs due to the radiation pressure of light on the particle. Gradient force results from the Lorenz force acting on the particle, which behaves like a dipole induced by the electromagnetic field [28]. This force pulls the particle towards the high-intensity region of the light [29].To find trap stiffness, the optical trap can be modeled as a spring, as demonstrated in Figure 1.6, where k is the trap stiffness, and x is the displacement from the beam center. According to the particle size, the physics of optical tweezers can be explained in two regimes, namely Rayleigh and ray optics regimes. These two regimes will be explained in the following sections.

1.2.1. Optical Tweezers in Rayleigh Regime

Rayleigh regime describes the forces on the spherical particle by radiation. In this regime, the size of the particle with radius a is very small compared to the wavelength of light, λ, which is $a < 1/10\lambda$ (see Figure 1.7).

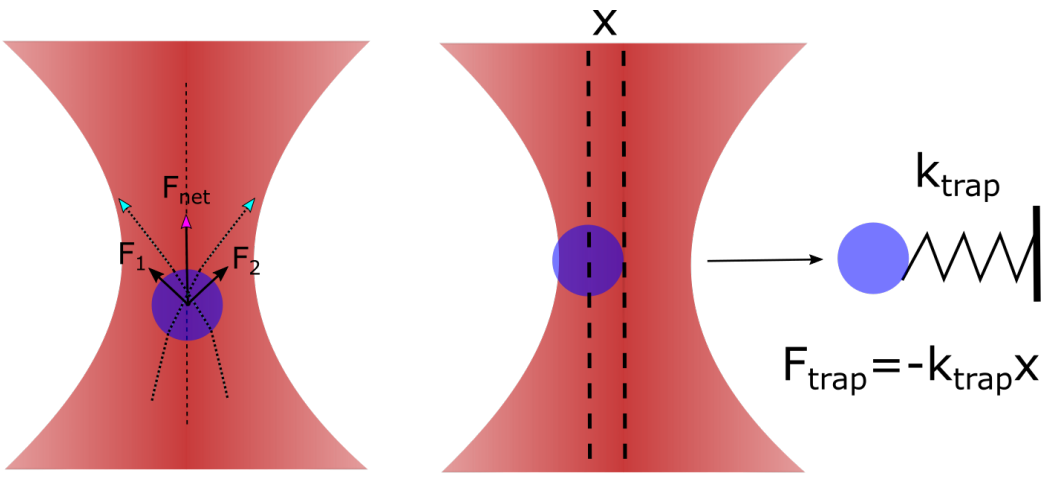

Figure 1.6. Forces on the optically trapped particle. The turquoise arrows show the refraction path of the light rays, F_1 and F_2 show the forces on the particle due to the refraction, and the pink arrow shows the net force which is pulling the particle towards the beam waist.

When a spherical particle, with the radius a, instantaneously is exposed to the electric field, $\boldsymbol{E}(\mathbf{r},t)$, it acts like a dipole with the dipole moment, $\boldsymbol{p}(\boldsymbol{r},t)$, as follows [30, 31]:

$$\boldsymbol{p}(\boldsymbol{r},t) = 4\pi\varepsilon_2 a^3 \left(\frac{\varepsilon_1 - \varepsilon_2}{\varepsilon_1 + 2\varepsilon_2}\right) \boldsymbol{E}(\boldsymbol{r},t), \tag{1.12}$$

where ε_1 and ε_2 are the dielectric constants of the particle, and the the medium, respectively. The scattering cross section of the particle is given as

$$\sigma_{\text{scat}} = \frac{8}{3}\pi(ka)^4 a^2 \left(\frac{m^2-1}{m^2+2}\right)^2, \tag{1.13}$$

where m is the ratio of the refractive indices of the particle to the medium, k is a dimensionless size parameter, which is $k = 2\pi a/\lambda$. As a result of a change in the laser light's momentum, the particle feels a scattering force due to the conservation of the total momentum. This force is called the scattering force, $\boldsymbol{F}_{\text{scat}}(\boldsymbol{r})$, and is given as

$$\boldsymbol{F}_{\text{scat}}(\boldsymbol{r}) = \frac{\sigma_{\text{scat}}\langle \boldsymbol{S}(\boldsymbol{r}t)\rangle_{\text{T}}}{c/n_2} = \hat{\boldsymbol{z}}\left(\frac{n_2}{c}\right)\sigma_{\text{scat}} I(r), \tag{1.14}$$

where $\boldsymbol{S}$ is the Poynting vector and can be written as $\langle \boldsymbol{S}(\boldsymbol{r},t)\rangle_{\text{T}} = \hat{\boldsymbol{z}} I(r)$. The gradient force that the particle feels is expressed as

$$\begin{aligned} \boldsymbol{F}_{\text{grad}}\,(\boldsymbol{r}t) &= [\boldsymbol{p}(\boldsymbol{r},t)\cdot\nabla]\boldsymbol{E}(\boldsymbol{r},t), \\ &= 4\pi n_2^2 \varepsilon_0 a^3 \left(\frac{m^2-1}{m^2+2}\right)\frac{1}{2}\nabla \boldsymbol{E}^2(\boldsymbol{r},t). \end{aligned} \tag{1.15}$$

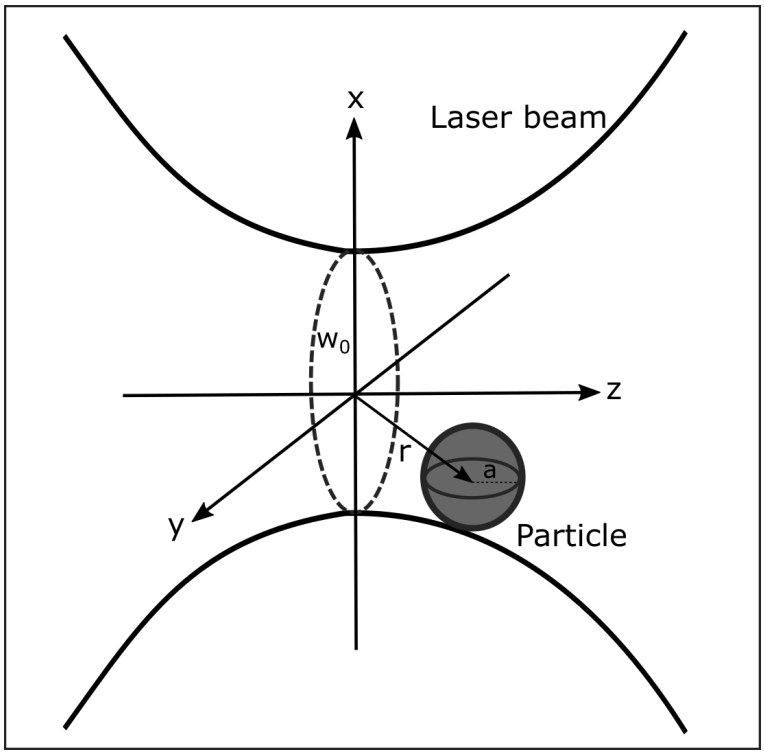

Figure 1.7. A particle with the radius a in an optical trap in Rayleigh regime.

To find the force at the particle's steady state we can take average of $\boldsymbol{F}_{\text{grad}}(\boldsymbol{r},t)$ over time as follows:

$$\begin{aligned}
&\boldsymbol{F}_{\text{grad}}(\boldsymbol{r}) = \langle \boldsymbol{F}_{\text{grad}}(\boldsymbol{r},t)\rangle_{\text{T}}\,,\\
&= 4\pi n_2^2 \varepsilon_0 a^3 \left(\frac{m^2-1}{m^2+2}\right)\frac{1}{2}\nabla\left\langle \boldsymbol{E}^2(\boldsymbol{r},t)\right\rangle_{\text{T}}\,,\\
&= \pi n_2^2 \varepsilon_0 a^3 \left(\frac{m^2-1}{m^2+2}\right)\nabla|E(\boldsymbol{r})|^2,\\
&= \frac{2\pi n_2 a^3}{c}\left(\frac{m^2-1}{m^2+2}\right)\nabla I(r).
\end{aligned} \tag{1.16}$$

1.2.2. Optical Tweezers in Ray Optics Regime

In ray optics regime, where the particle size, a, is bigger than the wavelength of the light ray, λ, that is $a > \lambda$, the scattering (F_{sc}), and the gradient (F_{gr}) forces exerted by a light ray on a dielectric sphere can be found using the formulae [32]:

$$F_{sc} = \frac{nP}{c} = 1 + R\cos 2\theta_{in} - \frac{T^2[\cos(2\theta_{in}-2\theta_{sc}) + R\cos 2\theta_{in}]}{1+R^2+2R\cos 2\theta_{in}}, \tag{1.17}$$

$$F_{gr} = \frac{nP}{c} = R\sin 2\theta_{in} - \frac{T^2[\sin(2\theta_{in} - 2\theta_{sc}) + R\sin 2\theta_{in}]}{1 + R^2 + 2R\cos 2\theta_{sc}}, \tag{1.18}$$

where θ_{sc} and θ_{in} are the refraction and the incidence angles, P is the power of the light ray, n is the refractive index of the medium, c is the speed of light, R and T are the Fresnel reflection and transmission coefficients of the object's surface at the angle θ.

1.2.3. Optical Tweezers in Different Configurations

Manipulation of biological materials, such as cells and tissues, by optical tweezers, can be built up in different configurations, such as dual-beam or single-beam optical tweezers and optical stretchers using face-to-face fiber lasers. Also, it is optional to trap cells with or without using microbeads. Trapping cells with the microbeads attached to the cells is one way of manipulating the biological sample. In this configuration, the beads are attached to the cells, and lasers are focused on the beads to prevent the cells from heat damage due to the laser (Figure 1.8a). Hence cells do not feel the laser so that heat-related photo-damage is minimized, and force calculation and trap calibration can easily be done for the spherical bead geometry. However, experimental preparation for bead attachment to cells is somewhat challenging. If the sample can adhere to the microscope slide, one beam can be used to stretch the biological material using the adhesion force on the one end of the sample (Figure 1.8 b). With dual-beam tweezers, it is possible to stretch cells without attaching the beads (Figure 1.8 c). In this way, experimental procedures become simplified, but cells are exposed to a laser which may cause photo-damage depending on the laser power.

In addition to this, since trapping is not done on the beads, it is difficult to calculate force and trap stiffness on different geometries other than the sphere. In the optical stretcher configuration, the sample is positioned between face-to-face fiber lasers having Gaussian profiles. The lasers are not focused on the cell between the two fibers (Figure 1.8 d), which decreases photo-damage. The stretching of cells is a result of the momentum transfer of light to the cell.

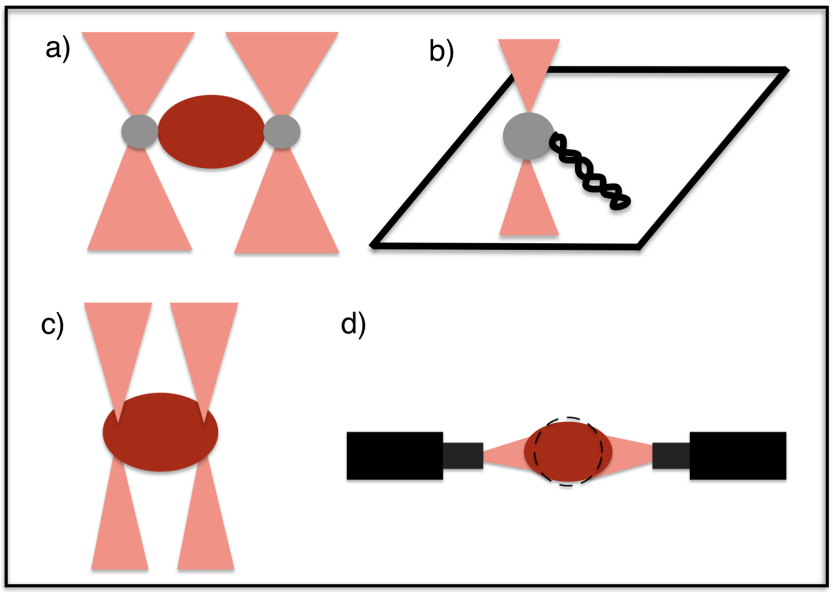

Figure 1.8. Different geometrical configurations in optical tweezers experiments, a) trapping with dual beams and beads, b) trapping of DNA by attaching one end to the slide and the other hand trapped with a bead, c) trapping with dual beams without using beads, c) optical stretcher method which uses two interface fiber lasers and stretches the cell in between by changing the laser power.

Since the refractive index of the cell is greater than the medium, the momentum of the laser beam increases when it enters the cell. By the same mechanism, the momentum of the laser beam decreases when it exits the cell. Hence, the difference in the momentum of the laser causes stretching of the cell [33]. Depending on the laser power, the refractive index, and the size of the cell, the applied force can be tuned by changing the laser power.

1.2.4. Cell Mechanics Studies with Optical Tweezers

The optical tweezers technique was used for the first time in biological applications by its inventor, Arthur Ashkin, in 1987 [34, 35]. He demonstrated that with the optical trapping technique, living organisms could be trapped and manipulated without affecting their vitality and functionality. He successfully conducted *in vivo* experiments on bacteria and viruses without damaging their vitality. According to his experiment on *E.coli* bacterium, he reported no damage was seen on the cell motility up to 80 mW

at 1064 nm wavelength by showing the reproduction of these cells within the optical trap [35]. Shortly after, some researchers showed that even intracellular structures like organelles and chromosomes could be optically trapped and manipulated [36].

Until our present day, the optical trapping technique has provided a wealth of knowledge in the field of cell mechanics studies in biophysical research since it can create forces on cells and in this way, it can deform cells in a controlled manner hence giving information about their mechanical features such as deformability, elastic modulus and adhesion force. Investigations in cell motility [37,38], cell stretching [39,40], aggregation [41,42], adhesion force calculations [43,44], cancer researches [45–47], and neuroscience [48,49] can be accounted for some of the application fields of the optical tweezers.

2. RAMAN SPECTROSCOPY AS A NON-INVASIVE DIAGNOSTIC TECHNIQUE FOR ENDOMETRIOSIS DISEASE

Endometriosis is a condition in which the endometrium, the layer of tissue that usually covers the inside of the uterus, grows outside the uterus. One of its severe effects is sub-fertility. The exact reason for endometriosis is still unknown and under investigation. Tracking the symptoms is not sufficient for diagnosing the disease. A successful diagnosis can only be made using laparoscopy. During the disease, the amount of some molecules (i.e., proteins, antigens) changes in the blood. Raman spectroscopy provides information about biochemicals without using dyes or external labels. In this study, Raman spectroscopy is used as a non-invasive diagnostic method for endometriosis. The Raman spectra of 94 serum samples acquired from 49 patients and 45 healthy individuals were compared for this study. Principal Component Analysis (PCA), k-Nearest Neighbors (kNN), and Support Vector Machines (SVM) were used in the analysis. According to the results (using 80 measurements for training and 14 measurements for the test set), it was found that kNN-weighted gave the best classification model with sensitivity and specificity values of 80.5% and 89.7%, respectively. Testing the model with unseen data yielded a sensitivity value of 100% and a specificity value of 100%. To the best of our knowledge, this is the first study in which Raman spectroscopy was used in combination with PCA and classification algorithms as a non-invasive method applied on blood sera for the diagnosis of endometriosis.

2.0.1. Introduction

Endometriosis is defined as the growth of endometrial gland and stroma outside the endometrial cavity, which is caused by an outflow into the peritoneal cavity. Previous reports demonstrated that one in ten women all around the world sought medical support due to endometriosis and endometriosis-related symptoms including pelvic pain (38.7%), dyspareunia (29.5%), and infertility (11.6%) [50]. Given that

the diagnosis of endometriosis depends on histopathologic examination after surgical excision, this approach requires anesthesia induction and hospitalization. Therefore, it significantly affects the quality of life of patients. Thus, researchers focus on new non-invasive methods for the diagnosis of endometriosis, including transvaginal ultrasonography, analysis of blood biomarkers, and genetic predispositions.

Raman spectroscopy provides information about molecular structures and chemical bonds of substances via the detection of inelastically scattered photons [51]. In Raman spectroscopy, the sample is illuminated by a laser beam and inelastically scattered light, which is composed of different frequencies, is observed. The scattered light contains two types of scattering, namely Rayleigh and Raman scattering. The intensity of the light in Rayleigh scattering is strong and the frequencies of the scattered and the incident light are the same, whereas in Raman scattering, the intensity is very weak (about 10^{-6} of the incident beam intensity) and the frequency of the scattered light is different from the frequency of the incident light. The difference between the energies of Rayleigh scattering and the inelastically scattered photons can be expressed as the Raman shift, $\Delta\tilde{\nu}$, and can be calculated using the following equation:

$$\Delta\tilde{\nu} = \frac{1}{\lambda_{laser}} - \frac{1}{\lambda_{scat}}, \tag{2.1}$$

where, λ_{laser} and λ_{scat} are the wavelengths of the laser and the scattered light, respectively.

The vibrational frequencies of each chemical bond within a molecule (e.g., O-H, C-O) are different, hence their fingerprints can be uniquely seen in the spectrum. It was reported in a study that during the disease, the amount of protein biomarkers in the blood varied, and these variations could be identified using multiplex and single immunologic testing technologies [52]. In this context, Raman spectroscopy is a useful tool for detecting the chemical content of a sample. Biologic samples such as tissue, blood, and serum are well-suited measurement samples for Raman spectroscopy because chemical changes accompany progressions of most diseases. Therefore, Raman spectroscopy has significant potential to provide valuable information to physicians in medical diagnostics [53].

Studies have shown that disease diagnostics with Raman spectroscopy is possible for both tissue and blood serum samples. Raman spectra of blood serum samples were used to diagnose many types of diseases, including Alzheimers disease [54], oral cancer [55], nasopharyngeal cancer [56], colorectal cancer [57], dengue infection [58], lung cancer [59], hepatitis B [60], and breast cancer [61]. Endometriosis, however, has thus far only been studied using Raman spectroscopy through tissue. Lieber *et al.*, indicated that Raman spectroscopy could differentiate tissues diagnosed as normal or endometriotic from tissues that were diagnosed as benign-cystic or cancerous [62]. Patel *et al.*, showed that stages of endometrial cancer could be distinguished using Raman imaging [63]. In another study by Notarstefano *et al.*, luteinized granulosa cells were measured using Raman micro-spectroscopy to separate ovarian endometriosis from control samples [64].

2.0.2. Principal Component Analysis (PCA)

By identifying the main components that maximize the variation between observations, principal components analysis seeks to capture the majority of the information in a dataset. The covariance matrix is a symmetric matrix with the same number of rows and columns as the number of data dimensions. Calculating the covariance between the pairwise means reveals how the characteristics or variables deviate from one another. When a matrix transformation is applied, eigenvectors are linearly independent vectors that do not change direction. The covariance matrix's Eigenvectors point in the direction with the greatest variance. The higher the Eigenvalue, the more variance can be explained. In other words, the Eigenvector with the highest Eigenvalue corresponds to the first principal component, which explains the majority of the variance, and so on. Eliminating information redundancy already aids in dimensionality reduction. However, because each new principle component reduces the proportion of total variance explained, we may further reduce dimensionality by removing the least relevant principal components. At this point, we must determine how many major components are necessary and how much information loss is acceptable. Finally, we must project data from our original feature space to the smaller area covered by our primary components.

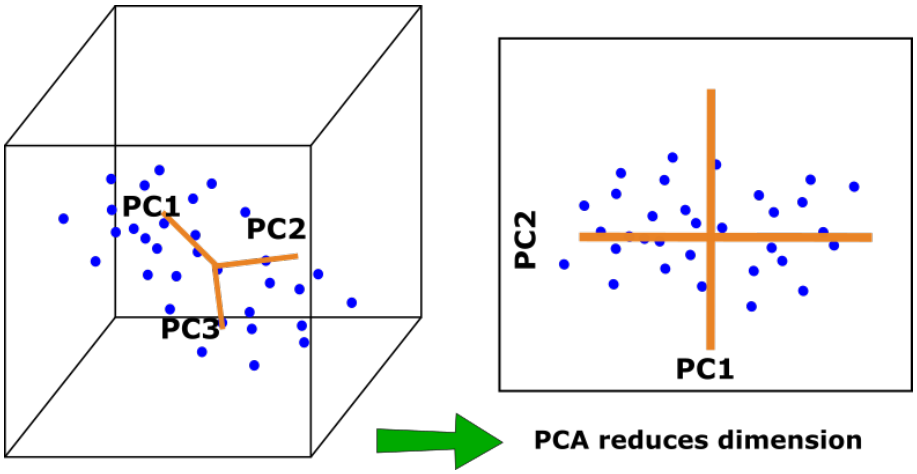

Figure 2.1. PCA analysis recudes dimension. PC means pricipal components.

To show theses statements mathematically, let us take a D-dimensional data set as follows:

$$X = \{x_1, x_2, \ldots, x_N\}. \tag{2.2}$$

Our aim is to find a K-dimensional representation of the data set where K<D. To do that, we have to find a K-dimensional subspace of D and a corresponding projection matrix A so that multiplication of X with A will result in the K-dimensional representation of our data set. For keeping the calculation simple let's take $K = 1$ so that the projection matrix becomes 1-dimensional which means A is a vector, represented as a_1, under this circumstances. Next, we desire to interpret the data matrix X by multiplying the projection vector a_1 and the new representation of X, called Z, is:

$$z_{1n} = a_1^T x_n, \tag{2.3}$$

where Z is:

$$Z = z_1, z_2, \ldots, z_N. \tag{2.4}$$

Here, z is the coordinate in X projected onto a 1-dimensional subspace. Using the eigenvectors we maximize the variance of the observations in X since we want to find the maximum variance representation of the coordinates in Z. The variance can be calculated by summing the squares of the observations in Z and dividing by the number of observations (N) in Z as given in the following equation:

$$V_1 = \frac{1}{N} \sum_{n=1}^{N} z_{1n}^2, \tag{2.5}$$

z can be interpreted in terms of a_1^T and x_n as in Equation (2.3), hence we have:

$$V_1 = \frac{1}{N}\sum_{n=1}^{N}\left(a_1^T x_n\right)^2. \tag{2.6}$$

By the symmetry rule we can write:

$$a_1^T x_n = x_n^T a_1. \tag{2.7}$$

Then, we can rewrite Z using the symmetry rule as

$$V_1 = \frac{1}{N}\sum_{n=1}^{N}\left(a_1^T x_n x_n^T a_1\right) = a_1^T\left(\frac{1}{N}\sum_{n=1}^{N}\left(x_n x_n^T\right)\right)a_1. \tag{2.8}$$

Let us define the parenthesis on the right side of the Equation (2.8) as C:

$$C = \frac{1}{N}\sum_{i=1}^{N} x_n x_n^T, \tag{2.9}$$

and rewrite the Equation (2.8):

$$V_1 = a_1^T C a_1. \tag{2.10}$$

We call the matrix C as the *covariance matrix*. Our aim was finding a vector a which maximizes the variance. To do that, we can differentiate V_1 with respect to a_1 and setting the expression equal to zero. Now, our aim to maximize the variance under the constraint that is:

$$a_1^T a = 1. \tag{2.11}$$

For this maximization problem, we can use Lagrange multiplier method as follows:

$$f\left(a_1, \lambda\right) = a_1^T C a_1 - \lambda_1\left(a_1^T a_1 - 1\right), \tag{2.12}$$

where, a_1 is the Eigenvector and λ is the Eigenvalue. Remember that the Eigenvector associated with the largest Eigenvalue equals the principal component that explains most of the variance. If we take a derivative of $f\left(a_1, \lambda\right)$ with respect to λ and equate to zero, we have:

$$\frac{\partial f}{\partial \lambda_1} = a_1^T a_1 - 1 = 0, \tag{2.13}$$

and

$$a_1^T a_1 = 1. \tag{2.14}$$

If we take derivative of $f\left(a_1, \lambda\right)$ with respect to a_1, we get:

$$\frac{\partial\left(a_1^T C a_1\right)}{\partial a_1} = a_1^T\left(C + C^T\right) - 2\lambda_1 a_1^T. \tag{2.15}$$

Since, the covariance matrix, C is symmetric we can write $C^T = C$, then the equation becomes:

$$\frac{\partial f}{\partial a_1} = 2a_1^T C - 2\lambda_1 a_1^T = 0, \tag{2.16}$$

hence we have:

$$a_1 C = \lambda_1 a_1^T. \tag{2.17}$$

With these findings we can rewrite the variance, V_1 as

$$V_1 = a_1^T C a_1 = \lambda_1 a_1^T a_1 = \lambda_1. \tag{2.18}$$

The final result imply that the variance, V_1, is equivalent to the Eigenvalue, λ_1, associated with the Eigenvector that spans the 1-dimensional subspace and therefore corresponds to the principal component. For the higher dimensions the Equation (2.18) becomes:

$$V_k = a_k^T C a_k = \lambda_k a_k^T a_k = \lambda_k. \tag{2.19}$$

where the total variance represented by k principal components can be found by summing λ_k over k.

2.0.3. k-Nearest Neighbor (kNN) and Support Vector Machines (SVM) Algorithms

k-Nearest Neighbor and Support Vector Machines combined with Principal Component Analysis (PCA) have frequently been used together with spectroscopy in disease diagnostics. kNN is a classification method based on the commonality within groups; every single spectrum can be treated as a point in a multidimensional space. This method calculates the Euclidean distance between each pair of spectra points. Then, by regarding the majority vote of its nearest neighbors, the class assignment of a sample is performed [65]. Support Vector Machine algorithm is a powerful, supervised learning algorithms, which were introduced by Vapnik [66]. It is used as a classification method in which every data element is viewed as a point in n-dimensional space (n is the number of features) with the value of each feature being the value of an individual coordinate.

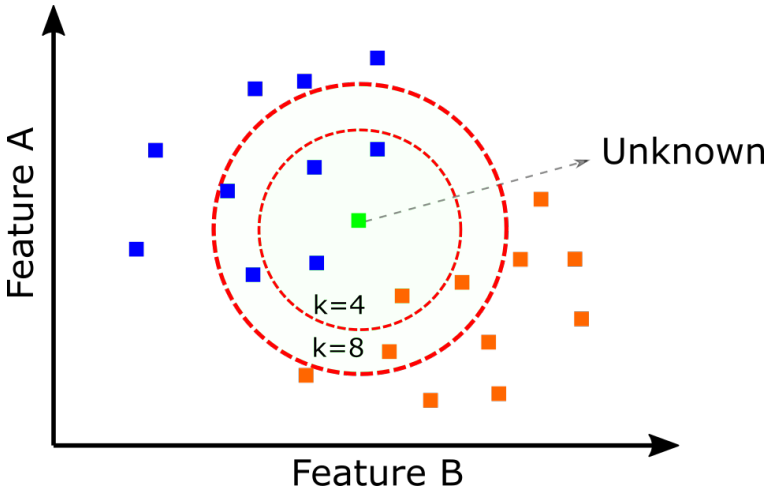

Figure 2.2. Algorithm of kNN.

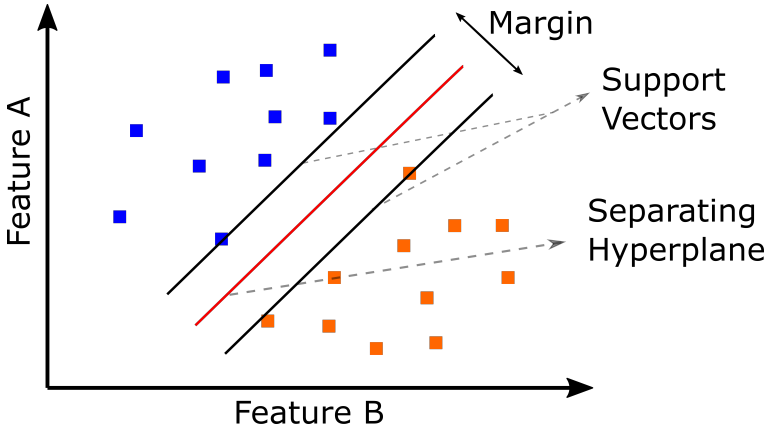

Figure 2.3. Algorithm of SVM.

Classification of the data is achieved by determination of the hyperplane that maximizes the margin between the groups. It is an elegant approach for the classification of spectral data [67–70].In some recent studies, classification methods and Raman spectroscopy were used together for disease diagnostics.

Dingari *et al.* reported that Raman spectroscopy and multivariate classification could discriminate lesions in stereotactic breast biopsies, irrespective of microcalcification status [71]. Li *et al.* developed a method for the non-invasive detection of colon cancer using Raman spectroscopy together with PCA and kNN [72].

In this article, we report the first Raman spectroscopy-based classification model

that can be used as a non-invasive diagnostic technique for endometriosis. This new approach requires only blood serum from a patient with endometriosis for the diagnosis of the disease. Therefore, the diagnosis of endometriosis could be achievable without laparoscopy.

Γpop2.0.3.1. Patient Selection. Forty-nine patients who had a surgical diagnoses of endometriosis and 45 healthy women with no history of pelvic pain or infertility were enrolled in this study after ethical approval was granted by the Ethics Committee of the Faculty of Medicine, Acibadem University. Each participant gave written informed consent. All experiments were performed in accordance with relevant guidelines and regulations. Student's t-test was applied on the data of volunteers who joined the study.

Table 2.1. Demographic data for the patient and control groups. (n): number of patients with myomas/adenomyosis. BMI: body mass index. Confidence level: 0.95.

	Control group	**Patient group**	***p*-value**
# of Volunteers	45	49	
Adenomyosis (n)	0	2 (4.08%)	0.290
Uterine myoma (n)	3 (6.60%)	5 (10.20%)	0.561
BMI	25.5±3.3	24.6±3.6	0.179
Mean Age (years)	27.1±7.8	29.4±5.4	0.315

There were no statistically significant differences between the patient and control groups in terms of age, BMI (body mass index), presence of uterine myomas, and adenomyosis, as given in Table 2.1. The patients were not divided into subgroups for the investigation because there is no known account to determine whether the main presenting symptom has a different underlying pathophysiology. Four patients had uterine myomas in the patient group, and three women had uterine myomas in the control group; all were asymptomatic. In the patient group, two patients had adenomyosis. Women with comorbidities, drug users, and patients with pelvic pain that was not proven to be endometriosis and who were not on their secretory phase (16-28th day) of the menstrual cycle were excluded.

Γpop2.0.3.2. Sample Preparation. Blood samples were taken in 10-mL gel tubes and centrifuged at 1500 g for 10 minutes to isolate the serum. All the serum samples were stored at $4°C$ and measured a maximum of two days after the collection. For the measurement, approximately 0.5 mL of the serum sample was prepared in a quartz cuvette.

2.0.4. Experimental Setup

The experimental arrangement (see Figure 2.4) was built around a home-built microscope that included a water immersion microscope objective (60X, NA, Olympus). A single mode diode laser (CrystaLaser) with wavelength 785 nm and power 100 mW

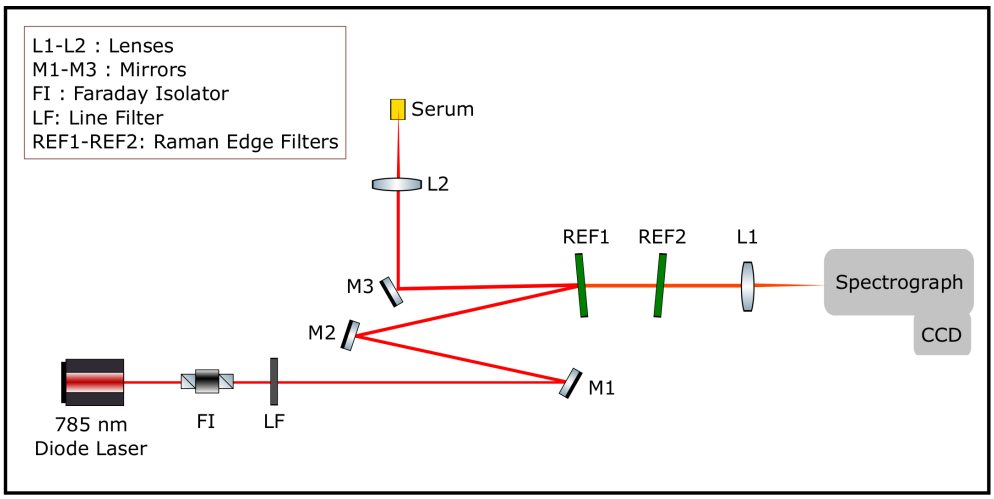

Figure 2.4. The experimental arrangement for Raman spectroscopy.

was used for Raman excitation. The unwanted back-reflected beams were filtered using a Faraday isolator (FI, EOTech), which was placed in front of the diode laser. A laser line filter (LF) was employed to obtain a clean laser profile around 785 nm (Semrock, LL01-780-12.5). The sample was illuminated through a focusing lens and the back-scattered light at 180°C geometry was collected using the same lens. The laser power on the sample was detected around 70 mW. The Rayleigh scattered photons were filtered using two sequentially located Raman edge filters (REF). The Raman scattered beam was focused on a 100 μm slit of a spectrometer (f = 303 mm, f/4, Andor) using an achromatic lens with a focal length 50 mm. The spectrometer was equipped with a

600 lines/mm grating and with a thermoelectric-cooled CCD camera (at -90°C, Andor iDus DU420A-OE).

2.0.5. Experiment and Analysis

The measurement and spectral analysis scheme is given in Figure 2.5. According to this scheme, first, the toluene spectrum was measured using an exposure time of 0.2 s for wavenumber calibration. Secondly, the distilled water spectrum was acquired using an exposure time of 30 s with 14 successive scans.

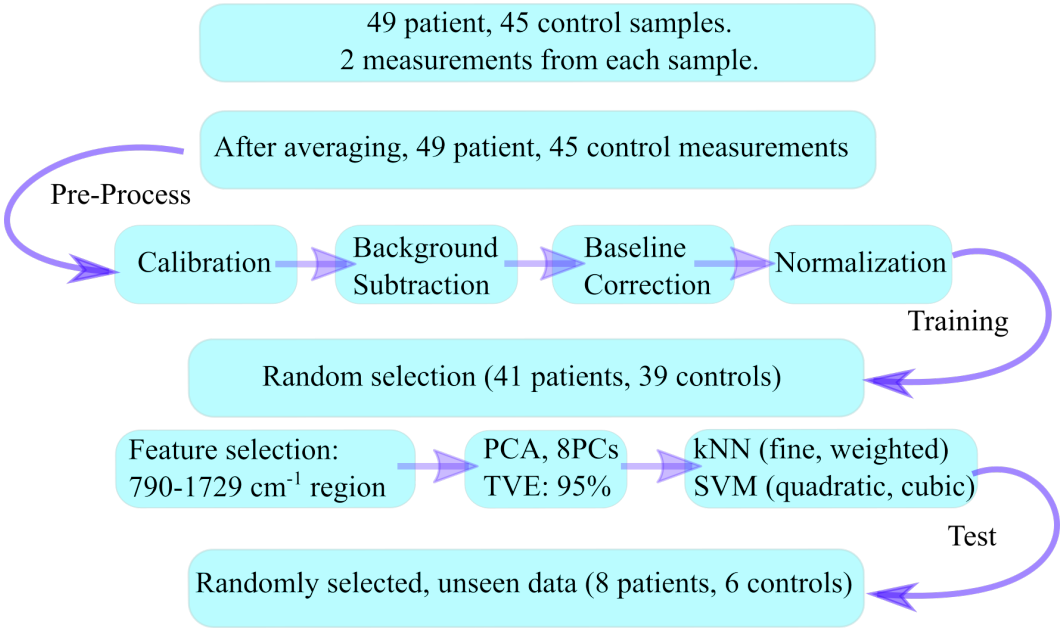

Figure 2.5. Infographic for the pre-processing and the data analysis.

The average of the water spectra was used for the background subtraction. Next, the Raman spectra of the serum samples were measured using the same integration parameters as with the water measurements. Each serum sample was measured twice sequentially. After cosmic-ray removal from the spectral data, 14 scans were decreased to 10 scans by excluding those with higher variance, and then these ten scans were averaged for each measurement. The spectra, which belonged to the same volunteer, were then averaged. Thereby, the data underwent pre-processing through a graphical user interface (GUI) that we wrote on the MATLAB platform (Figure 2.6). The GUI

performs the pre-processing steps, namely calibration (Figure 2.7), background (BG) (Figure 2.8), and baseline correction (BC) (Figure 2.10), as demonstrated in Figure 2.11a.

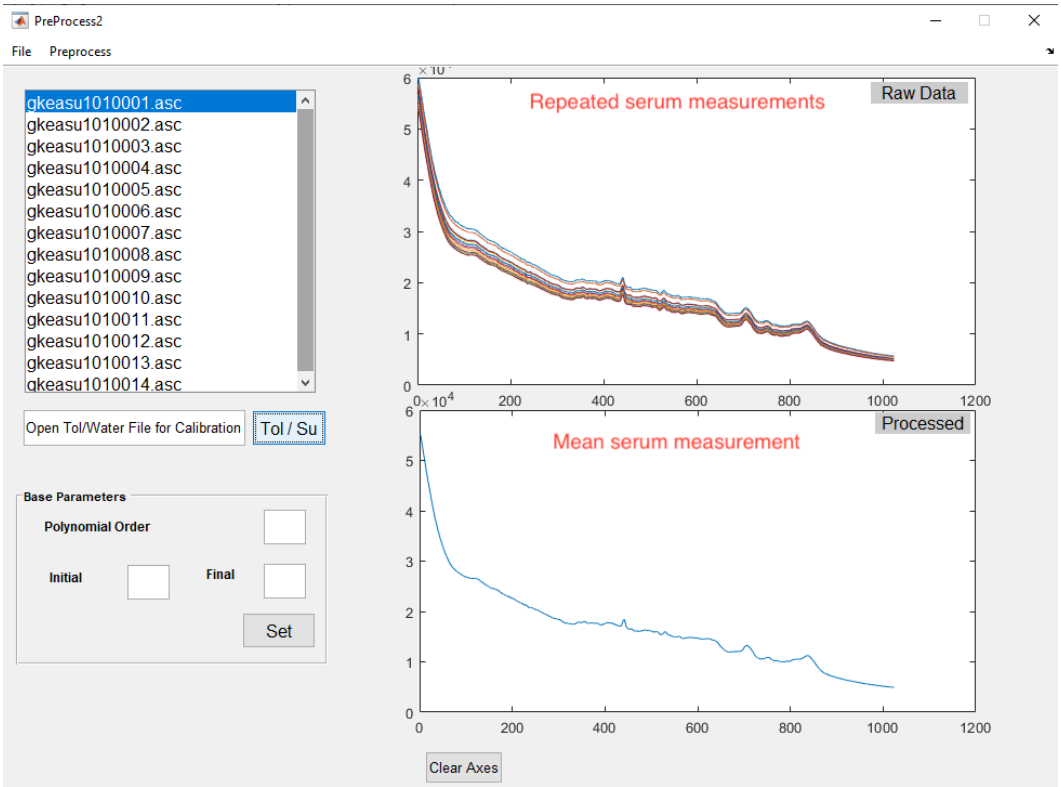

Figure 2.6. Average Raman spectrum calculation on GUI.

The developed wavenumber calibration method, which uses the Raman spectrum of toluene, was applied [73]. The reference bands of the toluene spectrum were used to calibrate the distilled water and serum spectra [51]. The distilled water spectra were subtracted from the corresponding serum spectra to exclude signals coming from the water and cuvette. This step makes the spectrum background-corrected (BG).

After the BG correction, there still remain auto-florescence signals coming from the serum sample. To further exclude these unwanted signals, baseline correction was applied for each spectrum by fitting a cubic spline curve on the selected 12 wavenumber points on the spectrum. To perform baseline subtraction, the selected wavenumbers (corresponding to the data points) were identical for each spline curve to ensure objectivity for each sample.

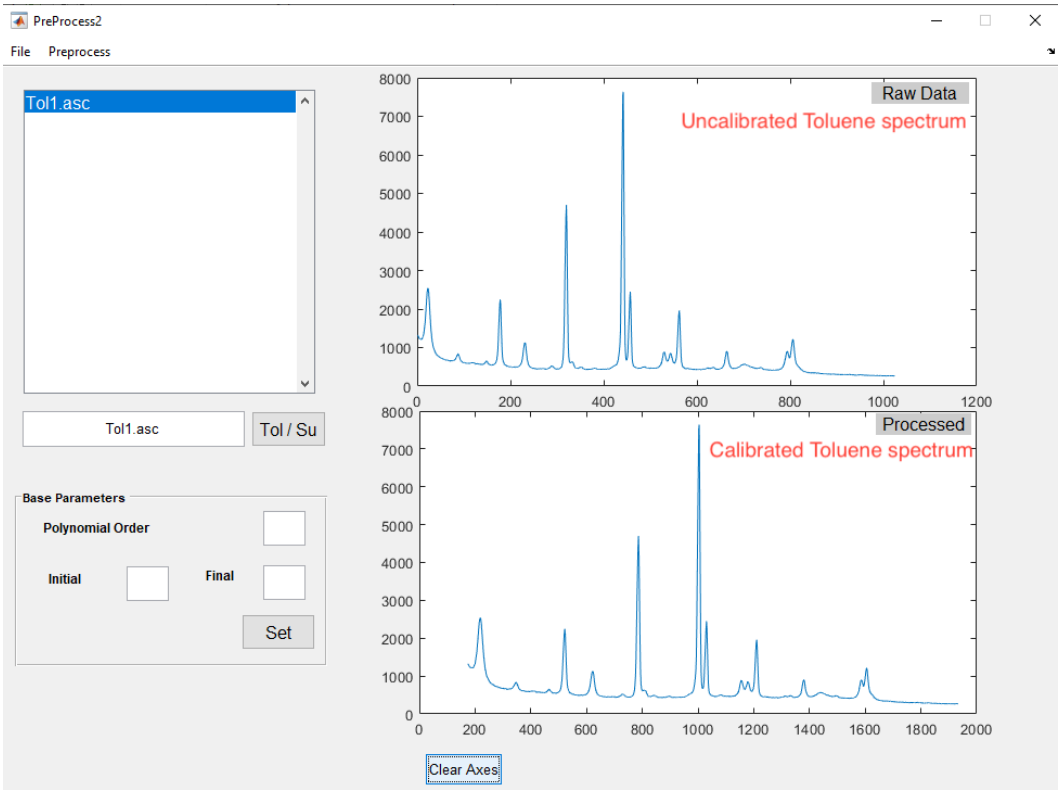

Figure 2.7. Calibration process on GUI using toluene.

Afterwards, the spline curve was subtracted from the BG spectrum to obtain the baseline-corrected (BC) spectrum (Figure 2.11a). Then, vector normalization was applied for each BC spectrum. The mean spectra of the normalized BC data of the two groups. The overall results of these steps can be viewed in Figure 2.11b. For further examination, PCA was applied to the vector-normalized background corrected data. This is a method for data description and compression, which is useful for reducing the dimension of large data sets while preserving most of the information. Its discriminating power for grouping data into clusters makes PCA noteworthy for diagnostic studies. After PCA analysis, built-in MATLAB functions were used to apply kNN (fine and weighted) and SVM (cubic and quadratic) classification methods to construct classification models. The feature selection was performed by re-constructing all the models 10 times for the selected regions because the 5-fold cross-validation algorithm of MATLAB's classification software is a random process. The standard deviation and the mean accuracy values for each model determined. Then, the interval of the spectrum with the highest classification accuracy values, was chosen.

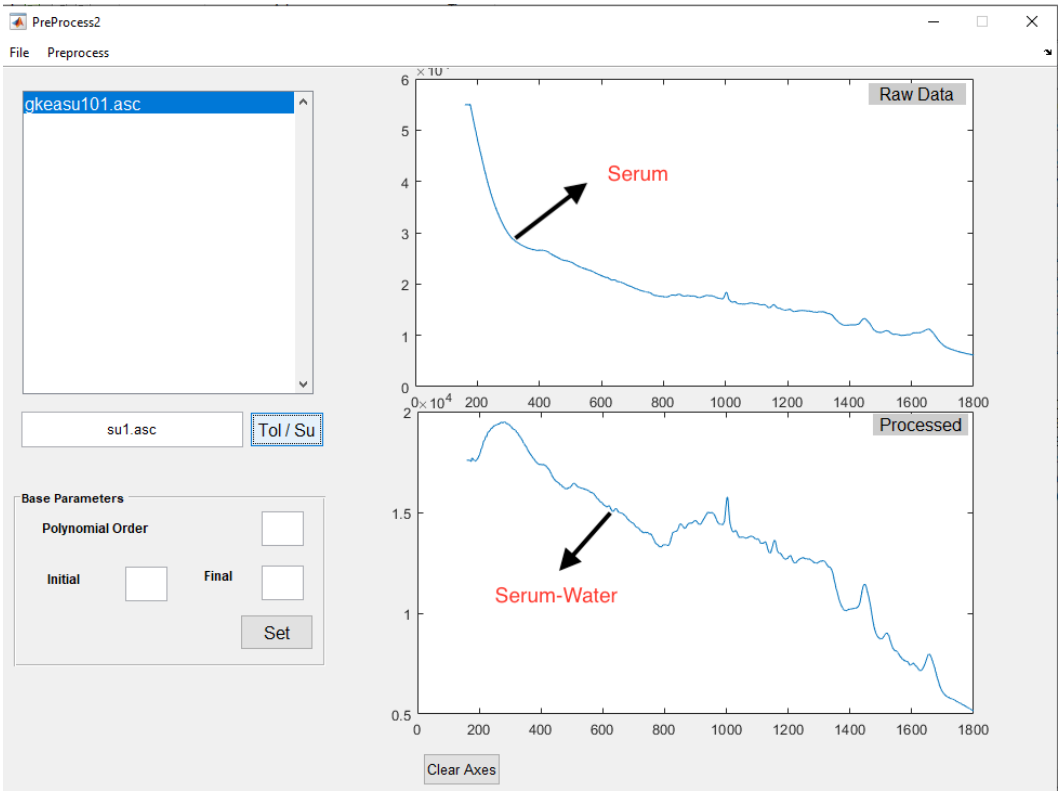

Figure 2.8. Background subtraction from the serum spectrum on GUI.

After feature selection, 85% of the total spectral data was selected as a training group, which included 41 patient and 39 control measurements. Then, the remaining 15% was set as test data, which contained 8 patient and 6 control measurements. By concerning the training and test results, the specificity, sensitivity, PPV, NPV, and the accuracy of the classification models were calculated according to the equations given in Figure 2.9.

	Actual Positive (P)	**Actual Negative (N)**	
Predicted Positive	True Positive (TP)	False Positive (FP)	PPV TP/(TP+FP)
Predicted Negative	False Negative (FN)	True Negative (TN)	NPV TN/(TN+FN)
	Sensitivity TP/(TP+FN)	Specificity TN/(TN+FP)	
	Accuracy (TP+TN)/(P+N)		

Figure 2.9. The definitions of sensitivity, specificity, positive predictive value (PPV), negative predictive value (NPV), and accuracy.

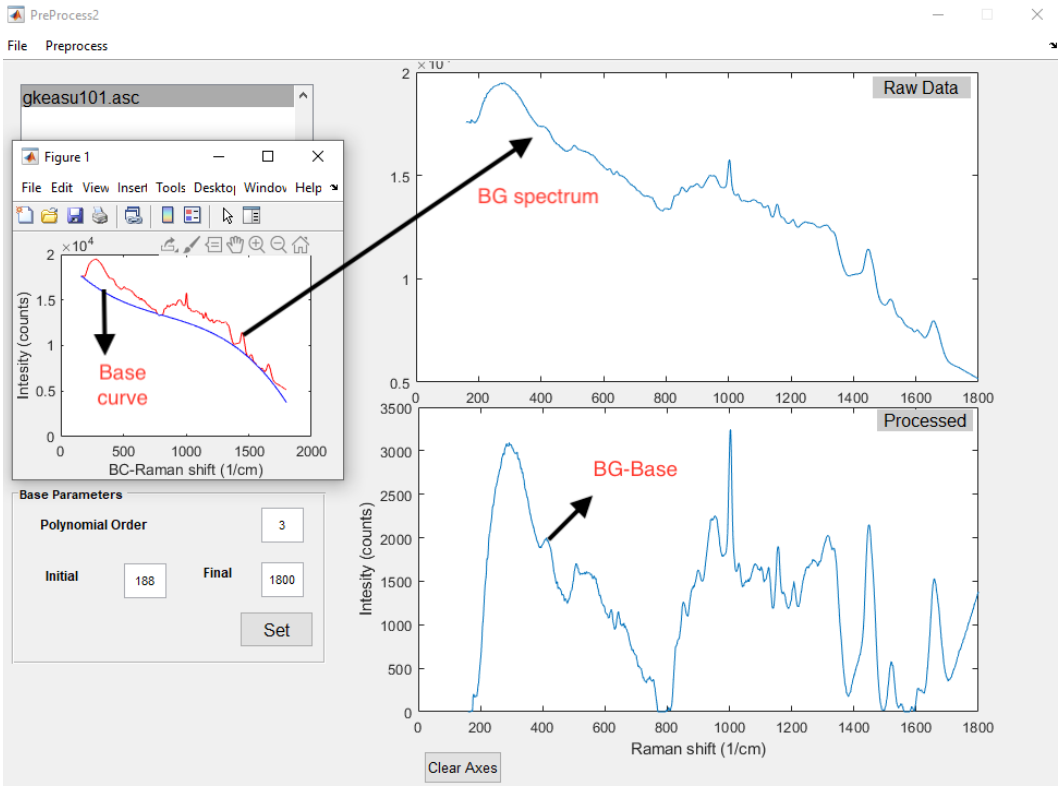

Figure 2.10. Baseline correction to BG serum spectrum on GUI.

2.0.6. Results and Discussion

The mean Raman spectra of the two groups are demonstrated in Figure 2.11b. Although the intensity difference between the groups in the spectral range of 500-750 cm^{-1} is apparent, this spectral interval was not used in the classification processes because the signal variance is high in that region. The appropriate region was chosen for the classification using the variable selection procedure, which is described in the *methods* section. For this procedure, the mean accuracy values of the classification models with the standard deviations (given in parentheses) were calculated and are given in Table 2.11. The final feature selection was decided by considering the region with the highest mean accuracy value, which was found as 790-1729 cm^{-1} spectral interval. Then, PCA was applied on the normalized and baseline corrected Raman spectral data to extract the relevant features for the selected region (790-1729 cm^{-1}). The number of PCs was set in the 95% of the total variance explained (TVE). The TVE values were found as 48.3, 17.2, 13.6, 5.2, 4.3, 2.9, 2.1, and 1.6, respectively.

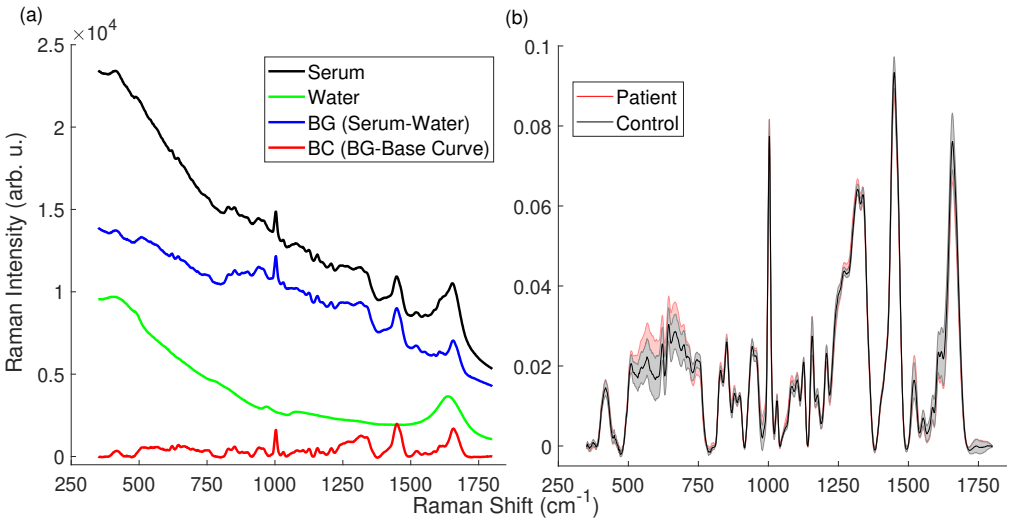

Figure 2.11. (a) Background (BG) and baseline-corrected (BC) Raman spectra of a serum sample. (b) Normalized BC mean Raman spectra of the control and patient groups. Standard deviations of each group were plotted and overlaid as shaded curves.

This condition requires 8 PCs for this model. All 8 PCs were included in the model. Figure 2.12a shows the PCA scores of the first against the third PC to visualize the discrimination of the two groups on the orthogonal feature plane.

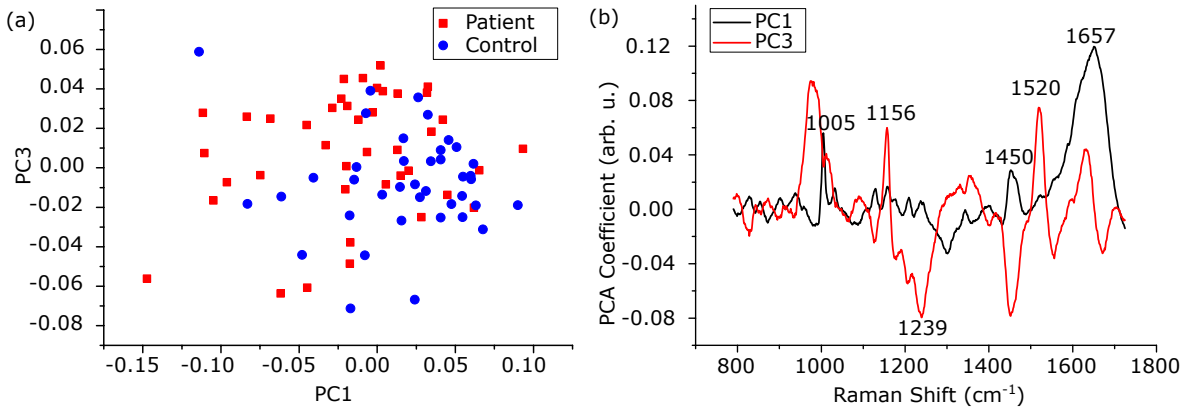

Figure 2.12. PCA performance on the training data set, which includes normalized BC data from 41 patients and 39 healthy individuals. (a) PCA score plot (PC1 vs. PC3) (b) Loading 1 and Loading 3 spectra.

Some of the peaks labeled on the loading graph, given in Fig 2.12b, demonstrate shifts and variations, which can be interpreted as changes in structure and the amount of some chemicals in serum during the disease.

Among these bands, 1005 cm^{-1} was tentatively assigned to phenyl ring angular vibrations due to phenylalanine content or C=CH bending vibration due to the ground state beta carotene content [74]. The presence of beta carotene also contributed to the 1156 and 1520 cm^{-1} bands, which are C-C and C=C stretching bond vibrations, respectively [75]. The peak at 1450 cm^{-1} was assigned to CH_2 bending vibration, which exists in lipids, phospholipids, and some amino acids [73]. Besides these, the peaks around 1239 and 1650 cm^{-1} were assigned to amide III (parallel beta sheet) and amide I, respectively. They are related to the secondary structure of proteins such as alpha helix (1657 cm^{-1}), parallel β-sheet (1630 cm^{-1}), and turn (1670 cm^{-1}) [61]. The importance of these bands in the diagnosis of endometriosis is not yet clear, and it is to be investigated in the future. On the other hand, the alteration of the bands at 1156 and 1520 cm^{-1} may refer to a change in the amount of beta carotene in the patient group. One explanation for this change could be that the alteration of retinoic acid metabolism in patients with endometriosis [76]. Taylor *et al.* reported a decrease in carotenoids in endometriotic tissues, which may be provide hope for medical therapies as adjuvants or alternatives to the surgical excision [77]. Therefore, beta carotene, which is an important member of the carotenoid family, may have a protective role against endometriosis.

After PCA, the study was carried a step further to examine the performance of the machine learning algorithms on the classification of the Raman spectral data. For this purpose kNN (fine and weighted) and SVM (cubic and quadratic) were used. The data set included measurements from 49 patients and 45 healthy individuals. The training and the cross-validation (5-fold) data sets were separated by selecting 85% of the total data (containing 41 patient and 39 control measurements) randomly. The remaining 15% (including 8 patient and 6 control measurements) of the data was used as unseen data to assess the predictive power of the classification models. The mean accuracy results of the selected algorithms are shown in Table 2.2. The performance of the applied classification methods in terms of their sensitivity, specificity, positive predictive value (PPV), and negative predictive value (NPV) is presented in Figure 2.2.

Table 2.2. Comparison of the mean accuracy results of kNN and SVM classification models for the four selected regions after 10 repetitions of calculations.

Feature Selection	**Mean Accuracy (%)**			
Region (cm^{-1})	**kNN-f**	**kNN-w**	**SVM-c**	**SVM-q**
450-1729	76.2 (2.9)	78.0 (3.6)	73.8 (4.1)	76.9 (4.3)
790-1729	79.4 (3.8)	82.1 (2.5)	80.0 (2.3)	82.5 (2.9)
1140-1729	72.8 (5.1)	77.3 (2.2)	77.5 (3.4)	78.5 (2.2)
1368-1729	63.3 (1.9)	65.8 (4.2)	68.5 (5.8)	64.5 (1.8)

Table 2.3. Comparison of the predictive ability of kNN and SVM classification models. All results are given in percentages. Information given in parentheses represents the ratio of number of correct predictions to the number of true class measurements. The superscripts means:$^{(a)}$fine, $^{(b)}$weighted, $^{(c)}$cubic, $^{(d)}$quadratic.

Training	**kNN-f** $^{(a)}$	**kNN-w** $^{(b)}$	**SVM-c** $^{(c)}$	**SVM-q** $^{(d)}$
Specificity	84.6 (33/39)	89.7 (35/39)	84.6 (33/39)	87.1 (34/39)
Sensitivity	78.0 (32/41)	80.5 (33/41)	75.6 (31/41)	75.6 (31/41)
PPV	84.2 (32/38)	89.2 (33/37)	75.6 (31/35)	83.8 (31/37)
NPV	78.6 (33/42)	81.4 (35/43)	83.8 (34/45)	76.7 (33/43)
Test	**kNN-f** $^{(a)}$	**kNN-w** $^{(b)}$	**SVM-c** $^{(c)}$	**SVM-q** $^{(d)}$
Specificity	100 (6/6)	100(6/6)	100(6/6)	100(6/6)
Sensitivity	87.5 (7/8)	100 (8/8)	87.5 (7/8)	87.5 (7/8)

Sensitivity and specificity are measures of classification success in predicting diseased and control specimens, respectively. Detailed explanations of these terms are given in Figure 2.9. The results indicated that application of the kNN-weighted algorithm on the spectral data exhibited the highest classification model accuracy among the others. Using this algorithm in the training procedure, 33 of 41 patients and 35 of 39 control samples were correctly classified. During the testing phase, the model was allowed to guess the correct label ("patient" or "control") of the unseen datum one by one. The results indicated that the model correctly classified 8 of the 8 patients

and 6 of the 6 control samples. In short, this result indicates a promising potential for the use of Raman spectroscopy together with the kNN-w classification algorithm for non-invasive diagnostics of endometriosis.

2.0.7. Conclusion

Developing a non-invasive method for endometriosis is challenging and currently under investigation. There are new strategies for improving transvaginal ultrasonography skills to diagnose mostly deep infiltrating endometriosis. Biomarker or genetic predisposition studies are being published in a growing manner. Laparoscopy is the most secure way to diagnose endometriosis, but it is an invasive method requiring such that patients should undergo a kind of surgery. Instead, a non-invasive method would be more economical and patient-friendly for the diagnosis of endometriosis. In this respect, as it was demonstrated for the first time in this article, Raman spectroscopy technique together with PCA and the classification algorithms could be a good candidate as a non-invasive diagnostic method for endometriosis.

To further improve this study, one might classify particular spectral bands of the serum spectrum that correspond to the suspected biomarkers of endometriosis. However, because there are insufficient literature data for reference Raman signals of all biomarkers of endometriosis (i.e., annexin V, VEGF, CA-125, slCAM-1 [52]), the Raman spectrum of each suspected biomarker should be measured as the reference spectrum to make more reliable inferences about the disease.

3. MEASURING THE EFFECT OF REPETITIVE STRETCHING ON THE DEFORMABILITY OF HUMAN RED BLOOD CELLS USING OPTICAL TWEEZERS

Cell mechanics plays an important role in many biological processes such that crawling, proliferation, spreading, stretching, contracting, division, and programmed cell death. The loss of cell viscoelasticity underlines various types of diseases such as sickle cell, malaria, cancer, and diabetes mellitus. To get a better understanding of the loss of viscoelasticity, mechanical responses of various types of cells to stress or strain are under investigation. Especially red blood cells are one of the simple structured cells that the effects of stress or strain could be easily assessed on. Thanks to their viscoelastic nature, they can deform by preserving the cell integrity when passing through the blood vessels that are smaller than their size. In this study, the individual RBCs were exposed 20 times to a transient biaxial stretch-relaxation cycle of 5 s by optical tweezers to find the mechanical response in terms of deformability index. According to the findings, we observed that RBCs lost their deformable structures with each cycle of stretching more and more and became almost undeformable after being repetitively stretched.

3.1. Introduction

Erythrocytes, or red blood cells (RBCs), are one of the most important circulatory cells responsible for carrying oxygen through the whole body [78]. With an average diameter of about 8 μm, an RBC has approximately 120 days of a lifetime during which it circulates nearly half a million times in the body [79]. While circulating, RBCs can deform without losing their functionality through the small capillaries with an inner diameter $< 3\mu$m. Their ability stems from the viscoelastic nature of RBCs, especially the cytoskeleton mechanics. However, towards the end of their life cycles, they start to degrade since they are repetitively deformed while going through the capillaries. This process grows RBCs fatigue, and their deformability breaks down.

The effect of stretching-related fatigue on the degradation of human RBCs is largely unveiled [80]. The membrane of the erythrocytes contains about 20 major proteins and at least 850 minor ones which interact with each other, but generally speaking, it is a three-dimensional protein scaffold mainly formed by spectrin, actin, and its associated proteins (tropomyosin, tropomodulin, adducin, and dematin), intact protein 4.1R, and ankyrin [81, 82]. Having such a crowded protein-based structure, the cell membrane is mainly viewed as two parts: lipid bilayer on the outer side and a 2D actin-spectrin protein meshwork, called *cytoskeleton* (CSK), on the cytoplasmic side of the membrane [83]. This two-dimensional protein meshwork embedded in the cell membrane is called *spectrin meshwork*, as can be viewed in Figure 3.1.

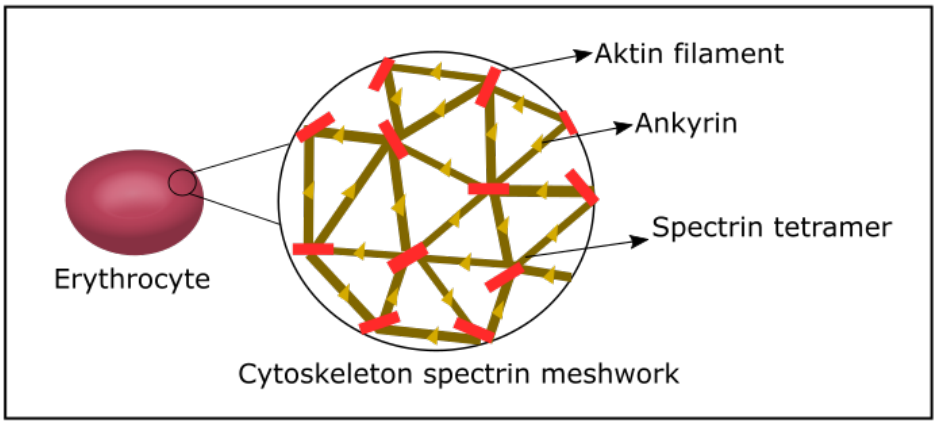

Figure 3.1. Some of the proteins that build up the cytoskeleton meshwork.

These spectrin polymers are crosslinked with each other at "junctions", which are complex structures formed by several proteins (i.e., F-actin) [84]. Usually, six spectrin polymers are seen as radiated from a junction which is called *sixfold connectivity*. In addition, fourfold connectivities are also observed [81, 85]. Although the exact mechanism that undergoes all the interactions of the myriad proteins in such a complex scaffold, with its dynamic protein meshwork structure, the cytoskeleton is crucial for RBCs in terms of their flexibility and longevity to survive in the circulatory system within their lifecycles [81]. The protein network structure creates a pre-existed tensile stress which is called *prestress* [14,86,87]. This allows cells to deform while maintaining cell integrity. The prestress that exists inside the cell is balanced by the microtubule struts that can be regarded as compression elements. The equilibrium between the

tensional and the compressional elements inside the cells is called *tensegrity* (tensional integrity) [88–90].

3.1.1. Universal Laws of Cytoskeleton Mechanics

Cells are active matter that can interact with the environment and create forces dynamically in many biological activities such as signaling, crawling, cell division, and cell contraction. They have two major parts: cytoplasm and cell membrane or cytoskeleton. The cytoplasm is a fluid in which all the organelles reside. In contrast, the cytoskeleton is a protein-based complex meshwork that makes cells deformable and conserves their shapes under mechanical stress. As a result, cells are neither viscous nor elastic organisms. Since the cytoskeleton and the cytoplasm can not be apart, cells are stated as viscoelastic. The cytoskeleton is composed of hundreds of different proteins. Understanding each protein's activity in the cell's mechanical behaviors is challenging in such a crowded and complex structure. There are many attempts that aim to describe cell mechanics from bottom to top, such as proteins and polymers and, from top to bottom such as tensegrity, power law, and soft glassy model. Yet, there is no unifying cell mechanics that could explain the universal cell behaviors.

Some researchers showed that cells tend to behave in certain behaviors under specific interventions independently from the cell types and the measurement techniques. These behaviors are observed in many experiments and stated as the universal laws of cytoskeleton mechanics, which are empirical laws [14, 16, 91–93]. These universal cell behaviors were observed in different cell types independent of the measurement techniques. The most frequently used modalities for these experiments are AFM and MTC (Figure 3.2). The universal behaviors of cells are stated as follows: (i) cell rheology is scale-free, (ii) cells are prestressed, (iii) diffusion is anomalous inside the cells, and (iv) stretching alters cell stiffness.

According to some studies with different modalities such as Magnetic twisting cytometry (MTC), internal laser tracking microrheology (ILTM), external laser tracking microrheology (ELTM), and two-point microrheology (TPM), it was observed dy-

namical modulus changes with the applied frequency [14, 17, 94]. Such a frequency dependency implies that there is no characteristic time for cells and cell rheology is scale-free.

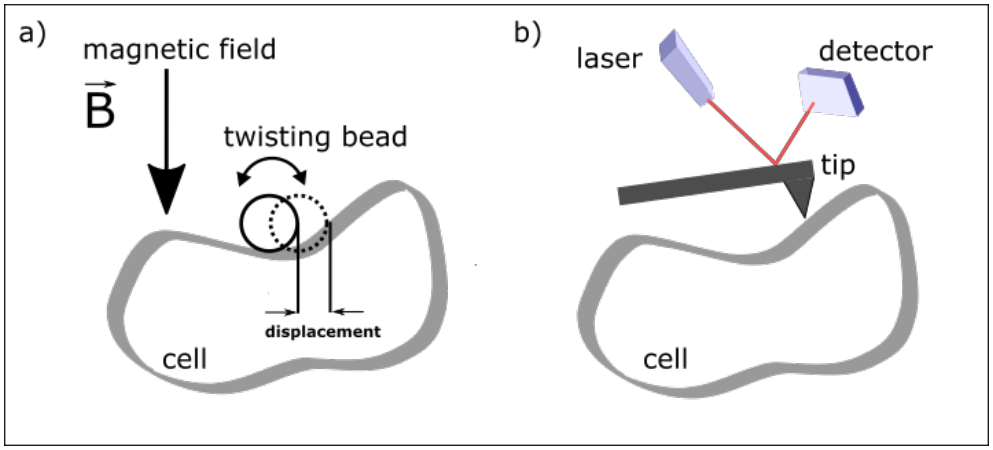

Figure 3.2. Cell rheology probed by a) MTC and b) AFM.

The prestressed nature of cells has been shown by laser cutting the actin fiber of the cells using a nano-scissor. The researchers observed that after some amount of time, the severed ends of the fibers splayed apart due to the inherited prestress of the cell [87]. Diffusion anomaly has been observed by examining the distribution of the mean-squared distance of the microbeads attached to the inside of the cells [16, 95]. Finally, the fourth law was observed in cell stretching experiments such that stretched cells may tend to act in both ways; solid-like or liquid-like [91]. In this study, we worked on two of them: stretching-related cell stiffening and being scale-free of cell rheology.

3.1.2. Strethcing-Related Cell Stiffening

According to one of the universal cytoskeleton mechanics laws, it is known that stretching alters cell stiffness [14, 91]. Such an alteration may result in two cases; cell stiffening [96–99] and softening [16, 100]. This controversial situation was cleared by some studies by stating that these two behaviors occur at the same time [91, 101]. That means cell fluidization during the stretching is masked by the concurrent stiffening behavior [99]. Stretching-related cell stiffening may be thought of as cells' and tissues'

self-protective mechanism, *mechanoprotection*, for holding their integrity [96, 97, 102]. Although the mechanical behaviors of the cells are controlled by a myriad of proteins, it is unlikely to separate each protein's contribution to the cells' mechanical behaviors [99]. Instead, stretching cells to understand the mechanical behaviors is more doable than assessing the cell mechanics in terms of their proteins [103].

Cell stretching can be achieved using different modalities such as MTC (magnetic twisting cytometry), micropipettes, MEMS (Micro-Electro-Mechanical Systems), microfluidics, and optical tweezers (OT) [40, 80, 104, 105]. Optical Tweezers can create direct mechanical stress on living cells, making it possible to deform them in a controlled manner. Especially, dual-beam OT enables cell stretching without any need for micron-sized beads as handles [39, 106, 107]. It is widely used in cell mechanics studies [26, 45, 108–114].

Magnetic twisting cytometry (MTC) is another widely used modality to probe cell mechanics. By applying torque to magnetic beads which are attached to the cells, it is capable of measuring mechanical properties at the single-cell level, but it has its limitation. With MTCs, only a small portion of the cells could be deformed by the attached beads, which limits measurement as a whole level at once. In addition to this, the contact area of the bead with the cell, as well as its location of the attachment to the cell, may not be precisely controlled in every measurement, and therefore the measurement may vary from cell to cell [115]. On the other hand, dual-beam optical tweezers are capable of assessing the mechanical properties of a single cell without any need to attach beads. In some of the studies on cell mechanics, by changing the twisting frequency of MTC, cell stiffness has been probed such that cells were observed stiffer as the frequency increased [92, 93, 103]. One of the other laws of universal cytoskeletal mechanics says that cell rheology is scale-free, that is, the dynamic modulus of cells changes with frequency as a power law and has no characteristic relaxation times [14, 17, 91–93, 103, 116].

In this study, we wanted to assess, at single and whole-cell levels, the two mentioned universal laws of cytoskeleton mechanics: stretching alters cell stiffness, and cell

rheology is scale-free. To do that, we repetitively stretched and relaxed the RBCs using OTs. Repetitive stretching was thought of as twisting a bead at a specific frequency (as in the case of MTC), and the deformability index (or strain) that we defined in this paper was associated with the inverse of stiffness. The effects of cyclic and static deformation on RBCs were assessed in a study using amplitude-modulated electrodeformation on a microchip [80]. However, this study used transverse lengths instead of axial lengths for technical reasons to calculate the cell extension. Since the response of the cell may vary in axial and transverse directions, the researchers have clearly stated that some differences may occur in the results due to the transverse definition of the extension ratio. Anyhow, their findings were conclusive and revealed increasing cell fatigue with the increasing number of cell stretching cycles.

In our work, we repetitively stretched 34 individual human RBCs with dual-beam optical tweezers to understand how the deformability changes after each stretching-relaxation cycle. The findings presented here gave an insight into the cell's mechanical behavior at a single and whole-cell level. Our results indicated that the stiffening behavior of the RBCs with repetitive stretching is consistent with the weak power law in the literature.

3.1.3. Cell Rheology is Scale-Free

According to some cell rheology experiments using MTC and AFM, it was observed that cell behaviors are frequency dependent [14, 92, 117]. That means there are no characteristic relaxation times for cells. Rahter, the relaxation times distributes as a power law depending on the frequency.

3.2. Materials and Methods

3.2.1. Collection of Blood Samples

Three healthy women and five healthy men volunteered for this study with the ethical permission (2021/04) of Boğaziçi University Science and Engineering Fields

Human Research Ethics Committee (FMINAREK). Blood samples were taken using a lancet needle from the participants' fingertips.

3.2.2. Sample Preparation

In an Eppendorf tube, 0.1 μL of whole blood was mixed with 1 mL PBS (Phosphate-buffered saline) and 100 μL BSA (Bovine Serum Albumin). 70 μL of the prepared sample was placed on the microscope slide, which was then covered with a BSA-dried cover glass. Nail polish was used to seal the edges of the cover glass, see Figure 3.3. The BSA-dried cover glass was made by pouring 15 μL BSA into a cover glass and drying it for 10 minutes at 70°C in an incubator. This procedure was carried out to prevent RBCs from adhering to the cover glass. All the experiments were carried out at room temperature.

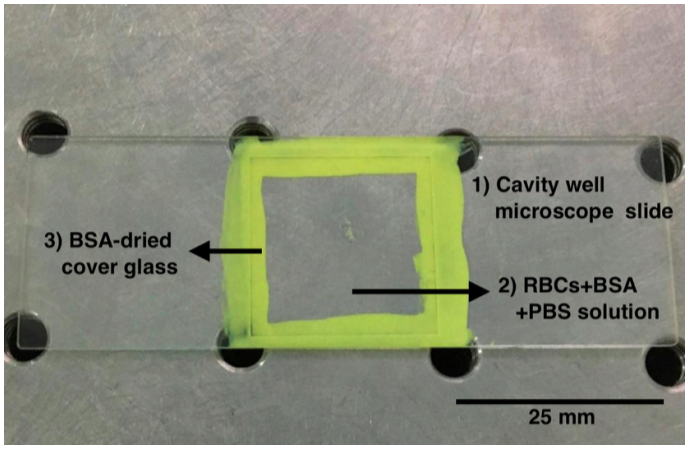

Figure 3.3. Sample on the cavity well microscope slide, covered with BSA-dried cover glass and sealed with nail polish.

3.2.3. Experiment and Analysis

All the experiments were conducted with commercial optical tweezers, namely Zeiss PALM micro tweezers with the laser wavelength of 1064 nm and the set laser power of 60 mW (the two traps share this power equally, 30 mW for each). The system has Axiocam 503 mono camera with the specifications 1936 (H) x 1460 (V) =

2.8 Mega Pixels, Max. file size per image: app. 5.6 MB at 1936 x 1460 pixels at 14 bit/pixel. It has an oil immersion 100x objective with the numerical aperture 1.3 and FWD = 0.20 mm (Zeiss Objective EC Plan-Neofluar).

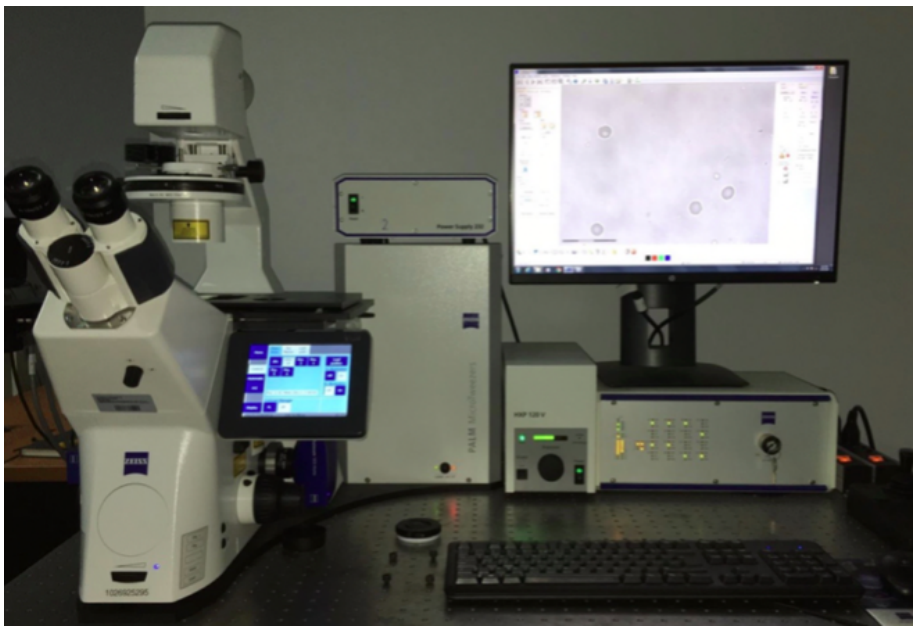

Figure 3.4. A view of the Zeiss PALM micro tweezers.

The experiment was created by setting the determined parameters (velocity, direction of trap movement, the power of the traps, and experiment duration) on the user interface of the tweezers, see Figure 3.5. With this setting, the stretching experiment was performed by the tweezers automatically. Before starting the experiment and while the laser was off, the traps were positioned on the two ends of the RBC with 5μm apart (Figure 3.6).

After the trap positioning, the laser was turned on, and the experiment started. The experiment was set such that while one of the traps was moving with the defined velocity, 10 μm/s, for 5 s, the other one was kept fixed in position. With the movement of the trap, the RBC was first stretched, and then after reaching the maximum stretched length, it escaped from the moving trap and began to relax (Figure 3.7). The experiment was conducted 20 times on an individual RBC, repetitively. During

the experiment, the total laser power that an RBC was exposed to is low [118], and the usage of 1064 nm laser wavelength further decreased the risk of damaging RBCs in terms of hemoglobin and water absorption [119].

Figure 3.5. Setting the experimental parameters on the interface of the Zeiss PALM micro tweezers.

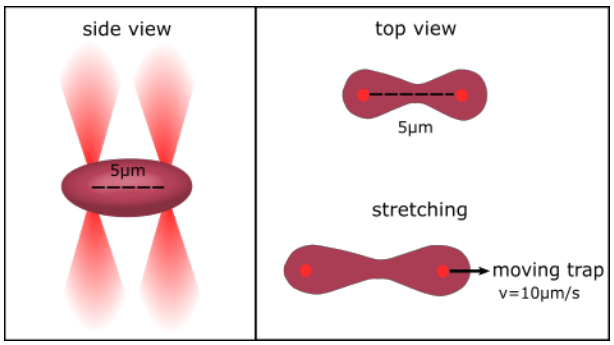

Figure 3.6. Cell stretching using the Dual-beam optical tweezers.

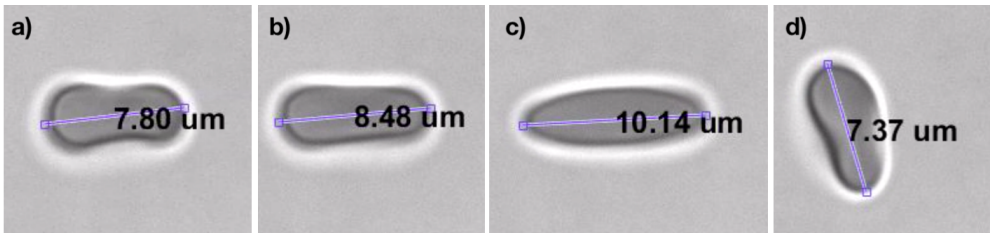

Figure 3.7. a) The trapped RBC before the stretching starts, b) the stretched RBC after the experiment is started, c) the maximum stretched RBC before escaping from the trap, d) the relaxed RBC after escaping from the trap.

3.2.4. Edge Detection Analysis

In the analysis, the axial diameter of the cell during the stretching was calculated with a MATLAB code I wrote. The algorithm of the code for analyzing a single cell can be stated in seven steps: 1) Original image (Figure 3.8a) was reversed in colors (unit8(255)-image); hence the reversed image was created (Figure 3.8b). This step is needed for making the inside of the image brighter than the environment to perform edge detection, 2) Using "greytresh" function, the image in Figure 3.8b was binarized. A binary image (Figure 3.8c) was created, 3) Using "imfill" function, the black areas inside the image became white. Binary image whose environment totally black and inside is totally white (Figure 3.8d) was created, 4) Using "bwboundries" function, edge (red curve) of the image in Figure 3.8d was calculated. The edge is demonstrated on the binary image and original image below:

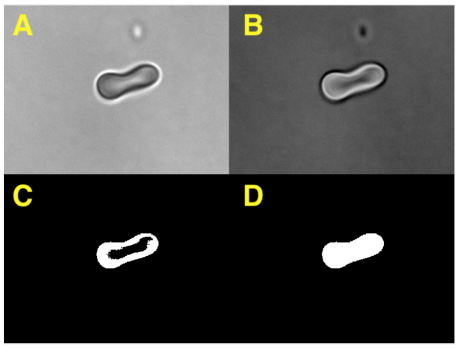

Figure 3.8. Edge detection preparation of a cell image. a) The original image, b) Reversed-color image, c) Binary image, d) Totally white-filled image.

5) "Max Feret Diameter" function was applied to find the long axial diameter of the edge in terms of pixel value, 6) Pixel to μm conversion is done using tweezers' scale bar (Figure 3.9c) and "measuretool.m" function. We calculated: 30 μm = 429.8 pixel.

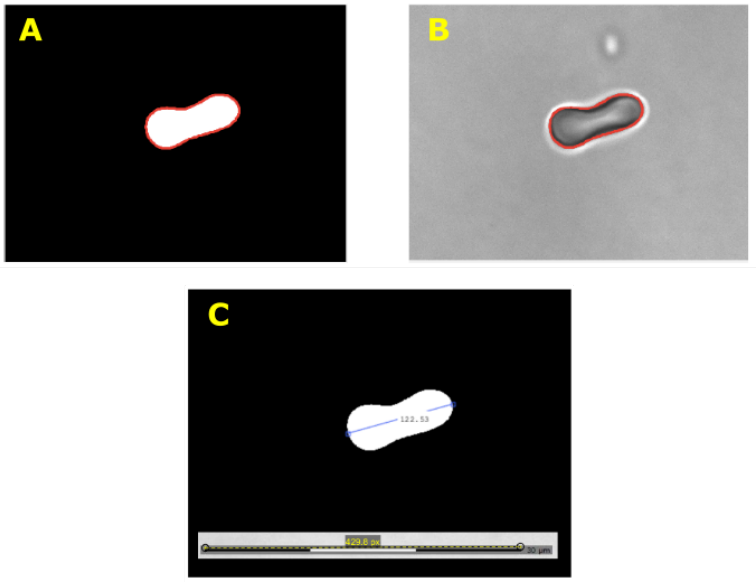

Figure 3.9. Edge detection and the length calibration of a cell image. a) Detection of the edge of the cell, b) the detected edge is shown on the original image, c) measurement of maximum Feret diameter.

So that, 1 pixel = 0.0698 μm, 7) Feret diameter (FD) in terms of pixel was multiplied by calibration factor (0.0698) to get FD in μm. After that, deformability index (DI) and stiffness (G'_n) were defined as [4, 91]:

$$DI = \frac{L_{max} - L_i}{L_i}, \qquad G'_n = \frac{1}{DI}, \tag{3.1}$$

where L_i is the initial (unstretched) length, L_{max} is the maximum stretched length of the RBC. We defined *permanent deformation* or *hysteresivity*, h, as the fraction of final length to the initial length of RBCs in analogy with the case in MTC as [120, 121]

$$h = \frac{L_f}{L_i}, \tag{3.2}$$

where L_i is the initial length of the cell and L_f is the minimum of axial lengths recorded after the cell escaped from the trap. The escape speed, u_{esc}, of an RBC from one of the traps was also investigated. The defined instantaneous escape speed is given in the following formula:

$$u_{esc} = \frac{L_{(max)} - L_{(max-1)}}{\delta t}, \tag{3.3}$$

where $L_{(max)}$ (point *p2* in Figure 3.10) is the axial diameter of the maximum stretched RBC, $L_{(max-1)}$ (point *p1* in Figure 3.10) is the axial length of the RBC framed just before $L_{(max)}$ and, δt is the time interval between these two.

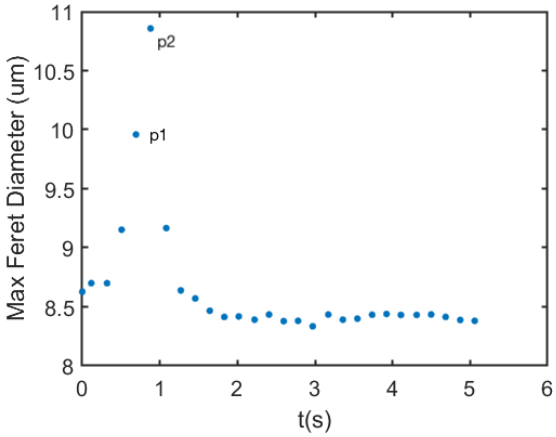

Figure 3.10. Change of maximum Feret diameter of an RBC during a stretching-relaxation process.

3.3. Results and Discussion

We observed that RBCs became stiffer with the increasing number of stretching-relaxation cycles. As given in Figure 3.11a the mean initial ($\bar{L}_i$) and the mean maximum stretched cell lengths ($\bar{L}_{max}$) converged almost to the same point with the increasing number of stretching. This finding evidenced that RBCs' loss of their deformable structures after undergoing a certain number of stretching-relaxation cycles. The calculated mean deformability index ($\bar{DI}$) of the cells, using $\bar{L}_i$ and $\bar{L}_{max}$, showed linear dependency on the stretching number in an inverse manner (Figure 3.11b).

Using MTC, the frequency-dependent exponential behavior of the cells was examined mostly in terms of storage and loss modulus or as a combination of these two, that is, the complex modulus or the defined fractional stiffness. [91–93, 103, 115, 120] In our case, we assessed the stiffness, G'_n, with the increasing stretching cycle. The exponential fit to G'_n data revealed the exponent 0.07 (Figure 3.11c), it is a compatible result of Deng *et al.,* which is 0.05 in the *slow regime* that they defined [93].

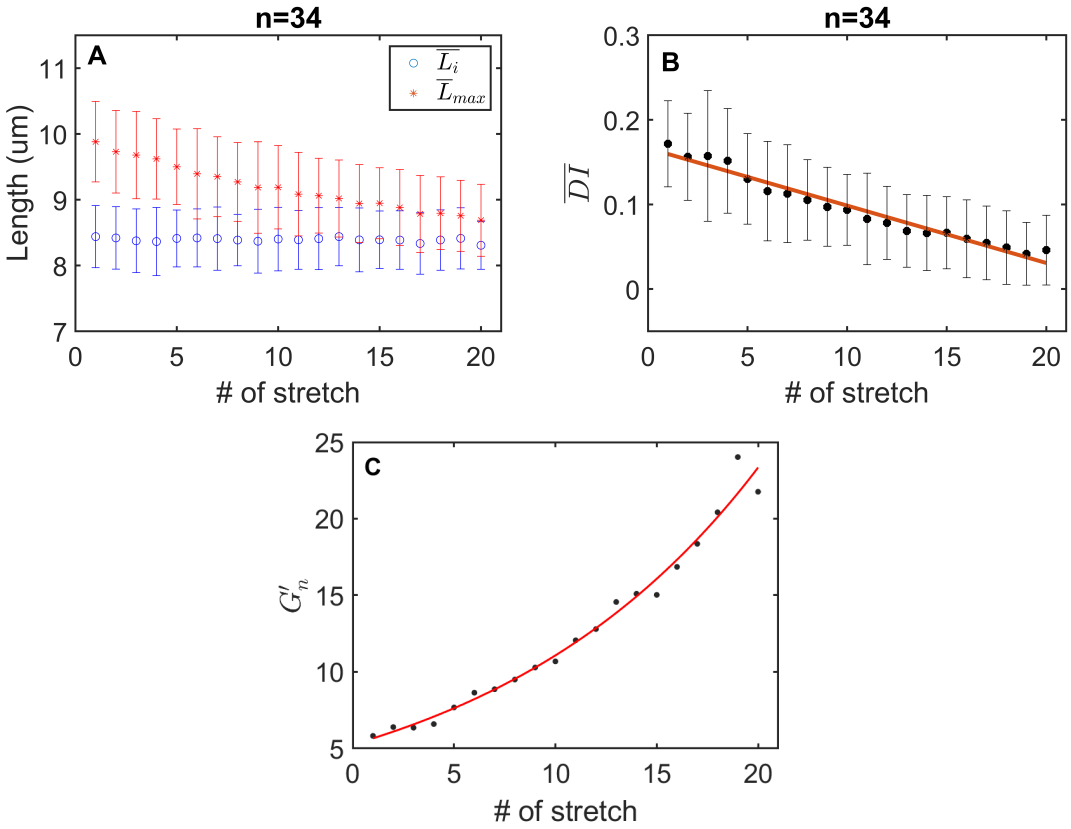

Figure 3.11. a) Change of $\bar{L}_i$ and $\bar{L}_{max}$ with the number of stretching, b) Change of $\bar{DI}$ with the number of stretching, the adjusted R-squared value is 0.96. n indicates the number of cells, c) Each data point indicates the mean of 34 cells. The exponent of the exponential fit revealed 0.074 with the R-square value of 0.98.

In Figure 3.12a the data of time-dependent stretching and the recovery processes were demonstrated for all the cells. In the figure, each ribbon line represents the mean time-dependent MFD of the 34 cells corresponding to the stretching number. Clearly, with each stretching-relaxation cycle, from 1^{st} to 20^{th}, maximum cell lengths (the peak value in the graph) decreased which indicates cell stiffening. In Figure 3.12b, the mean relaxation data of the 1^{st}, 10^{th}, and 20^{th} stretching were shown. The exponential fit to the relaxation data revealed the decay time, τ. The decay time or the relaxation time of the first stretching cycle given in Figure 3.12b revealed 228 ms. This is quite a similar result with one of the works of Henon *et al.,* that is 206 ms [119] in which optical tweezers were used. Having similar results using the same modality is affirmative. On the other hand, the cells were not repetitively stretched. Therefore, we cannot

compare the rest of the data (after the first stretching) with this work. However, when we compare the decay times of the 1^{st}, 10^{th}, and 20^{th} stretching in our experiment, there is a slight decrease from 1^{st} (228 ms) to 10^{th} (217 ms) and a dramatic increase from 10^{th} to 20^{th} (550 ms) stretching.

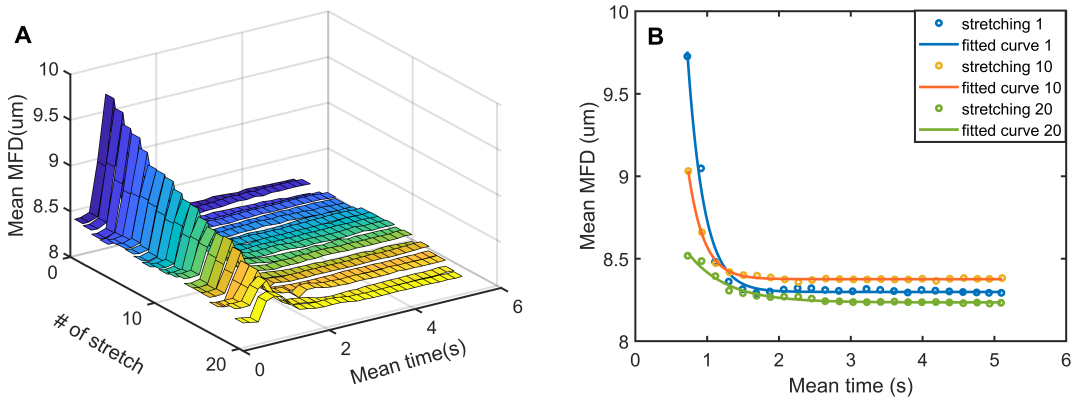

Figure 3.12. a) Change of Feret diameter during the stretching and the recovery processes with time. Each ribbon line represents the mean MFD of the 34 cells for the corresponding stretching #, b) The exponential fit result of the relaxation data of the cells. Open circles represent the experimental data, and the solid curves are the exponential fit to the data. The data shows the relaxation process of the 1^{st}, 10^{th} and 20^{th} stretching of the cells (of 34). Decay times of the fit curves are 228 ms (stretching 1), 217 ms (stretching 10), 550 ms (stretching 20), with the corresponding R-square values; 0.98, 0.99 and, 0.97.

Solid-like and liquid-like behaviors of the cells have been assessed by the defined hysteresivity, h. As given in Figure 3.13a, the mean h ($\bar{h}$) falls below 1. The cell behavior is considered liquid-like when $h > 1$, which enables the cell to alter its shape, crawling, spreading, division, and contracting [120]. On the other hand, when $h < 1$, the mechanical behavior of the cells is considered solid-like which is closely related to the ability of rapid shape recovery in response to deformation [120]. According to our results, $\bar{h}$ values for each stretching fall below $h = 1$ line (Figure 3.13a), which may be concerned that RBCs display solid-like behavior. The escape speed of the cells from the trap was investigated to further indicate the change in the biological

material. The mean instantaneous escape speed ($\bar{u}_{esc}$) was found to be decreasing with the increasing number of the stretching cycle. As shown in Figure 3.13b, it has a non-linear pattern which indicates that membrane displacement in a unit time interval decreases with a decreasing rate. This may be thought of as *a lag* to respond to the force. RBC cytoskeleton is principally composed of spectrin, actin, and the associated proteins [81]. Actin, one of the constituents of the cytoskeleton, has a major role in cell mechanics, force generation, and motility [122–124]. One of the reasons behind the stretching-related stiffening of the cell may be attributable to the force-induced actin accumulation in CSK [97]. Another explanation may come from stretched-induced chemical reactions in the cells. It is reported that stretching triggers the activation of several biochemical pathways in the cells and, such a disturbance causes cell stiffening [97, 109, 125]. However, this study has no experimental evidence of stiffening due to such a chemical change.

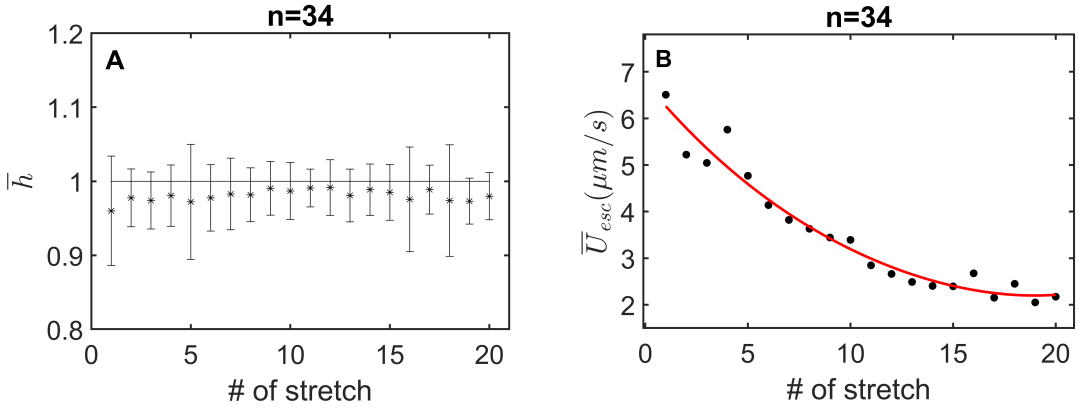

Figure 3.13. a) Mean permanent deformation, $\bar{h}$, of the 34 RBCs are shown for each stretching number. All the data points were below the $\bar{h} < 1$ line. This indication was interpreted as a solid-like behavior of the RBCs, b) Exponential fit (red line) to $\bar{u}_{esc}$ revealed $y = 6.743e^{(-0.08x)} + 0.0321e^{(0.16x)}$ with the R-square value of 0.95, n indicates number of the cells.

The effect of repetitive stretching on the cell morphology was demonstrated in Figure 3.14. It was seen that the membranes of the unstretched cells were smooth, whereas the membranes of the stretched ones have darker areas which may be a sign

of protein damage or actin/spectrin accumulation. [126] The difference between the morphology of the stretched and the unstretched cells could be seen better in a different colorbar (colorcube MATLAB). When the colorful images were compared, the unstretched cells had concentric circular structures while that structure was distorted on the stretched cells. Besides, the centers of the stretched cells were brighter than the unstretched ones. This situation may be because of a decrease in the biological material in this area which made us again think of protein accumulation (darker areas) towards the edges.

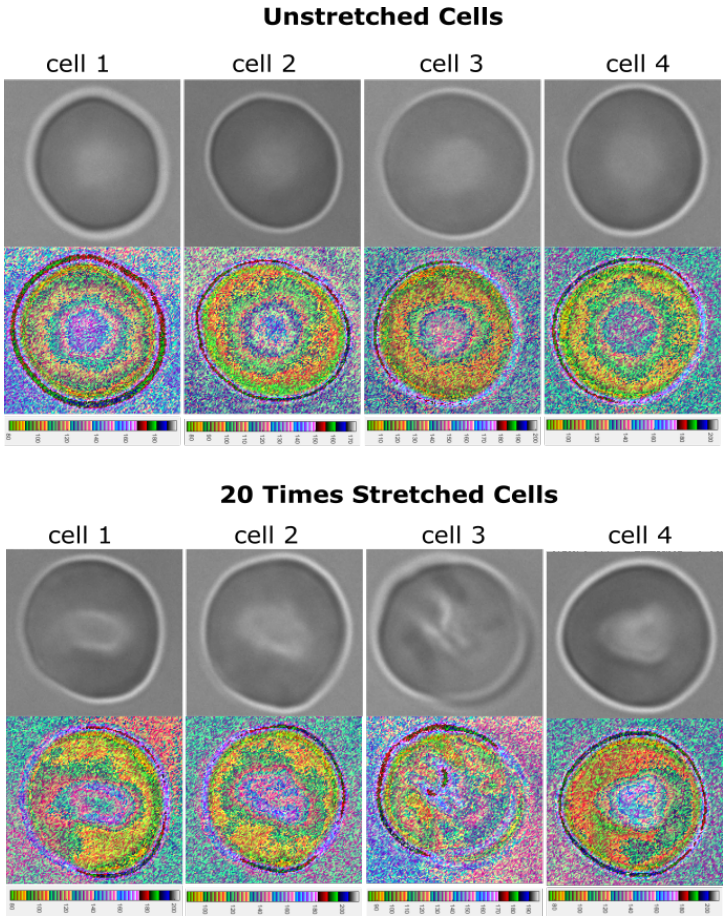

Figure 3.14. Effect of repetitive stretching on the membrane morphology of the selected four RBCs. The images were demonstrated in terms of both the grayscale images and the colorcube colorbar (of MATLAB). The first two rows show the cells before stretching, while the last two rows show the cells after being stretched 20 times. Concentric circles are seen on the unstretched cells while this structure is distorted on the 20-times stretched cells.

3.4. Conclusion

The universal laws of cytoskeleton mechanics state that stretching alters cell stiffness and cell rheology is scale-free. These laws have been verified mostly by using MTCs and AFM on different cell types. Depending on the frequency, an exponential trend was seen with those modalities in the cell stiffness and the relaxation time constant. By the nature of these modalities, cells could not be deformed as a whole. Instead, small parts of cells could be deformed to understand the mechanical response. In our work, we stretched RBCs using optical tweezers without using beads to test those laws at the whole-cell level. Therefore, our experiment has no twisting beads at a specific frequency. In this work, twisting an attached bead to a cell is physically considered repetitively stretching a cell by OTs. So, each stretching number or cycle, in our case, corresponds to each twisting of the bead in MTC. With this analogy, we have analyzed how cell stiffness changed with repetitive stretching. It is arguable how twisting a bead at $f = 10s^{-1}$ is equivalent to stretching a cell 10 times repetitively. To answer this question, one may stretch the cells at different trap velocities since increasing twisting frequency physically means deforming the cells faster in a unit time interval. Overall, exponential behavior of the stretching-dependent cell stiffness has been observed on RBCs using optical tweezers, and our findings agree with the previous works to some extent.

4. COMPARISON OF THE HUMAN'S AND CAMEL'S ERYTHROCYTES DEFORMABILITY USING OPTICAL TWEEZERS AND RAMAN SPECTROSCOPY

The evolution of red blood cells (RBCs) or erythrocytes has led to variation in morphological and mechanical properties of these cells among many species today. Camelids have the most different RBC characteristics among the vertebrates. As a result of adaptation to the desert environment, camelid RBCs can expand twice as much of their total volume in the case of rapid hydration yet are almost undeformable under mechanical stress. The difference between cell features of the human and the camelid species was explored both mechanically and chemically with optical tweezers and Raman spectroscopy, respectively. We measured the deformability of camel RBCs relative to the human RBCs at the single-cell level using optical tweezers. We found that the deformability index (DI) of the camel and the human RBCs were 0.03±0.05 and 0.22±0.08, respectively. Raman spectral analysis of the whole blood indicated that some of the Raman peaks observed on the camel's blood spectrum were absent on the human blood's spectrum, which further points to the difference in chemical contents of the two species.

4.1. Introduction

All the vertebrates, except Antarctic icefish, have circulating hemoglobin fluid packed in red blood cells. These cells are responsible for oxygen transport for all the modern vertebrates [127]. RBCs vary in shape and size among the vertebrates, ranging from over 50 μm to below 10 μm [128]. The possible outcomes of such variations to RBCs' mechanical functions are still under investigation [129]. Regarding such variations in RBCs' shape, size, and deformability, there is no unique description of optimized RBC characteristics. Human RBCs are biconcave-shaped viscoelastic cells.

Having an average diameter of about 8μm, they can deform through the small capillaries (with an inner diameter less than $3\mu m$) without losing cell functions. Thereby, deformability is a crucial property for them to circulate through the vascular system effectively.

On the other hand, camelid RBCs are rigid and almost undeformable under mechanical stress [130, 131]. Rather, their ellipsoidal shape aligns them with the stress field. They can transverse through the circulatory system, owing to their shape. [130] Yet, they can expand twice as much of their initial cell volume, [132–135] which advantage camelids survive in the desert environment in the case of a large amount of hydration [136–138]. Such expandability and, at the same time, undeformability of these cells is related to the cell membrane phospholipid composition, which makes the membrane more fluid and the cells resistant to osmotic variations [136, 139, 140]. It is reported that in the case of dehydration (water loss up to 27%), the fluidity of the camel blood is not affected since the camel erythrocytes make up a small amount of the blood content [141].

The molecular mechanism for the difference between the camelid and human RBCs, in terms of osmotic stability, was explained by the protein-lipid ratio and protein organization of the cell membrane [142–144]. A study reported that the protein-lipid ratio for human RBC ghosts (which are dead cells without cytoplasmic structures) was found as 1.25, while this value for camel RBCs was 3.0 [142]. Another study showed that the protein-lipid ratio was 1.2 and 3.7 for human and camel erythrocyte membranes, respectively [143]. The same study also indicated that the amount of membrane integral proteins was almost five times greater in camel cells [143]. High resistance to osmotic lysis of the camel erythrocytes was formerly explained by this high protein-lipid ratio, especially integral proteins, without referencing a specific protein [145].

Camel RBCs were investigated with varying techniques and modalities, such as Klett photometer [146], microcinematography [134], flame photometer [147], sonic irradiation [142], gel electrophoresis [131, 143, 145], viscometric techniques [130], scanning electron microscope [131], scanning and transmission electron microscopy [144],

chromatography [148], blood count, [137] proteomics [140], and rheometry [149]. These studies focused on osmotic behaviors, susceptibility to direct hemolysin of cobra venom, protein composition, and organization of the membrane, the relationship between cell shape and membrane structure, homeostasis, and viscosity. Optical trapping is a handy tool for life sciences, especially cell mechanics investigations. It enables fixation-free immobilization of biological particles, making it possible to manipulate them in the desired way. The physical principles behind this tool rely on the generation of optical forces resulting from the change in optical momentum that is transferred to the particle of interest [24, 34, 150, 151]. When a correct wavelength is used, it has become possible to investigate a cell in its living medium with no or very little photodamage. By adding a second beam or splitting the original beam into two, a dual-beam optical tweezers system can be created where the cell mechanics is interrogated by stretching cells [39, 152–154]. Double-beam optical tweezers studies have two types of geometry: i) the beams counter-propagate [4, 154, 155] ii) both beams are in the axial direction and catch the cell from two ends [40, 156–159]. Among these studies, deformation of red blood cells was investigated for healthy cells [155, 156], type 2 diabetes mellitus and diabetic retinopathy [4], and radiation therapy applied cells [40].

As the mechanical properties of the cell change, the chemical structure changes, as well. An efficient way to monitor this change is Raman spectroscopy. This technique examines the vibrational transition energies due to laser-molecule interaction. The frequencies of the photons scattered from the sample are different from the illumination frequency as much as the frequency of molecular vibration [21]. Raman spectroscopy was utilized to understand the mechanical and chemical structure of the red blood cells previously for some of the species but has never been applied to camel blood yet [160–164].

In this study, we aimed to approach the camel RBCs from the perspective of cell mechanics by measuring cell deformability. We used optical tweezers to apply direct mechanical stress on an isolated RBC for the deformability measurements. Mechanical stress was created by trapping the erythrocytes from the two ends and moving one of the traps with a certain speed, and cell stretching was achieved. In addition, for

chemical analysis, we utilized Raman spectroscopy to have Raman spectra of whole blood from both species.

4.2. Methods

4.2.1. Blood Collection

With the ethical permission (2022-05) of Bogazici University Science and Engineering Fields Human Research Ethics Committee (FMINAREK), one healthy woman and two healthy men volunteered for this study. Experiments with two healthy male single-humped dromedaries were conducted with the permission (2021-017) of Bogazici University Institutional Animal Experiments Local Ethics Committee (BUHADYEK). Blood samples were drawn using a lancet needle from the participants' fingertips. A veterinarian has drawn blood samples for the camelid RBC experiments, and the samples were transported inside EDTA tubes at 4°C. All the measurements were completed on the same day of blood collection.

4.2.2. Sample Preparation

Whole blood of 0.1 μL was mixed with 1 mL PBS (Phosphate-buffered saline) and 100 μL BSA (Bovine serum albumin) solution in a tube. 70 μL of the prepared blood sample was placed onto the microscope slide, and BSA-dried cover glass was placed on top. The edges of the cover glass were sealed using nail polish. The BSA-dried cover glass was used to prevent RBCs from adhering to the cover glass. The BSA-dried cover glass was prepared by placing 15 μL BSA on a cover glass and kept in an incubator at 45°C for 10 minutes. The experiments were performed at room temperature.

4.2.3. Experiment and Analysis

The experiments were performed using dual-beam Zeiss PALM Micro Tweezers, with a wavelength of 1064 nm and a laser power of 60 mW (30 mW for each trap). The determined stretching parameters (velocity, direction of movement, the power of

the traps, and experiment duration) were set on the user interface of the tweezers. Before starting the experiment, the optical traps (while off) were configured on the cells. For human RBCs, the traps were positioned on the two ends of the cell with a trap separation of 5μm. Whereas, for camel RBCs, the traps were positioned at the center of the cells on top of each other. After the positioning procedure, the traps were activated, and the experiment started. During the stretching, one of the traps was moving with the defined velocity of 1 μm/s for 10 s, while the other one was kept fixed in position. When the trap starts to move, the RBC first stretches, and then after reaching the maximum stretched length, it escapes from the moving trap and begins to relax (see Figure 4.1).

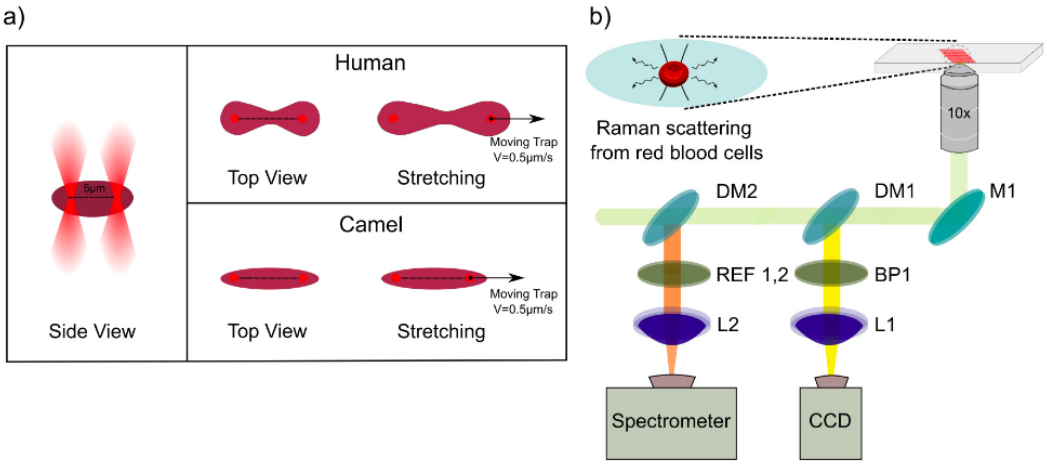

Figure 4.1. a) Side view of a trapped RBC and top view of stretched Human and Camel RBCs b) Raman spectroscopy setup.

The maximum Feret diameter function of MATLAB was used to calculate the axial diameter of the cells. Deformability index (DI) [4] was calculated using the following equation:

$$DI = \frac{L_{max} - L_i}{L_i}, \tag{4.1}$$

where L_i is the initial (unstretched) length, L_{max} is the maximum stretched length of the RBC.

4.3. Results and Discussion

To study cell stretching characteristics, we measured the cell lengths of 206 human and 159 camel RBCs when they were optically trapped in our experimental setup. We show, in Figure 4.2, the time-lapse images of the camel and the human red blood cells.

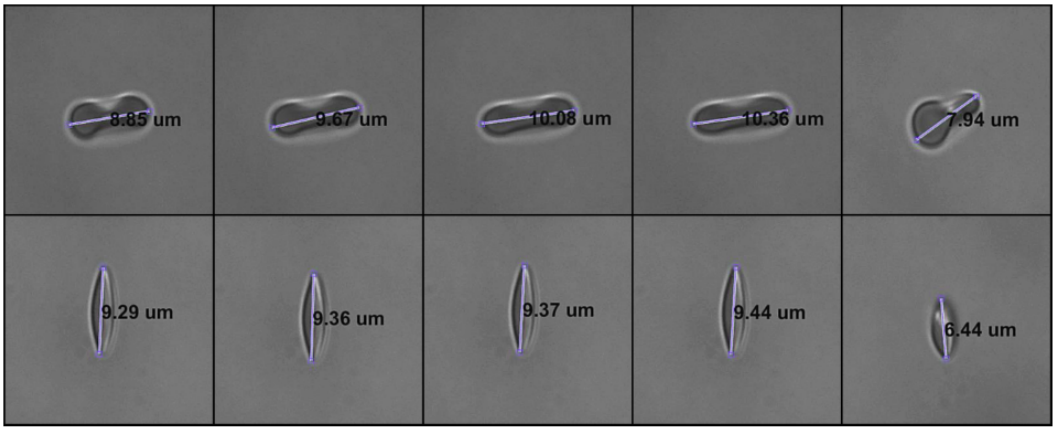

Figure 4.2. Top view of stretching and relaxation processes of a human (top row) and a camel (bottom row) RBCs. Calculated maximum Feret diameters were labeled on the RBCs in each frame.

During the image processing, we calculated the maximum Feret diameter of the RBCs for each frame dynamically and created movies for each RBC we experimented with. As a result, we found their time-dependent length during the stretching and the relaxation states. In the figure, we annotated the selected bright field time-lapse images with the calculated Feret diameters. Using the same technique, we calculated the mean initial long axial lengths for the camel and the human erythrocytes as 8.51±0.86 μm and 8.66±0.57 μm.

To investigate cell deformation under mechanical stress, we measured their axial lengths in each frame to compare their initial, and the maximum stretched lengths. Their distributions with the bandwidths are given in Figure 4.3. The analysis indicated that camel RBCs were less deformable than the human RBCs. In Figure 4.3c, we demonstrate the boxplot of the deformability index data that we calculated using the

initial and the maximum stretched lengths of the RBCs.

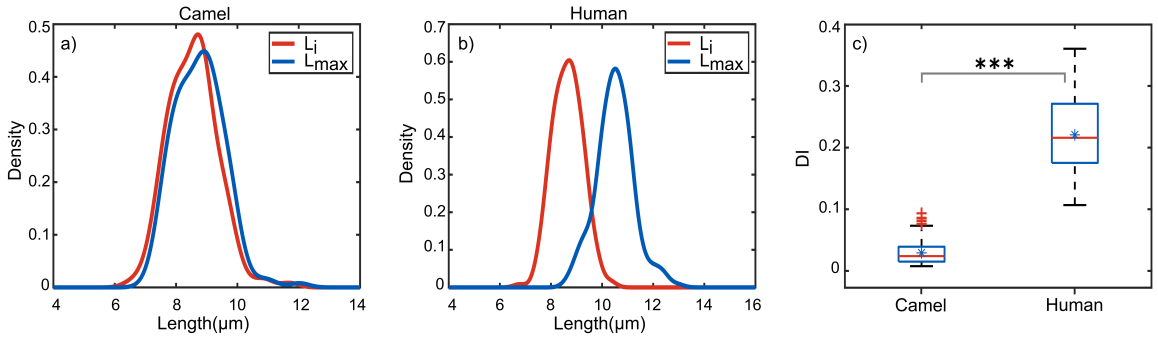

Figure 4.3. Normal kernel distribution of initial and maximum stretched lengths with the corresponding bandwidths: a) for the camel 0.2964 and 0.3130 and, b) for the human 0.2304 and 0.2496 c) Box plot of the DI. The means and the standard deviations of DI for camel and human groups are 0.024±0.0188 and 0.215±0.061, respectively. The result of the t-test: $p<0.001$.

The graph revealed the mean DI of the camel and human groups with the standard deviations as 0.024±0.0188 and 0.215±0.061, respectively. This result showed that camel RBCs are one order of magnitude less deformable than human RBCs. The Student's t-test was applied to the DI data, and the difference was found as statistically significant ($p<0.005$).

To obtain chemical information from the two species' RBC, we acquired Raman spectra of the whole blood taken from all samples we analyzed with optical tweezers. We repeated the measurements ten times for each sample to apply statistical analysis. In Figure 4.4, we demonstrated the difference between the average Raman spectra of both species.

The average Raman spectra are different in several Raman shift positions. To quantify the difference and to reveal the sub-components of the important peaks, we applied a Gaussian curve-fitting on the spectra. The main differences between the two species are located in the Raman shift values stated in Table 4.1.

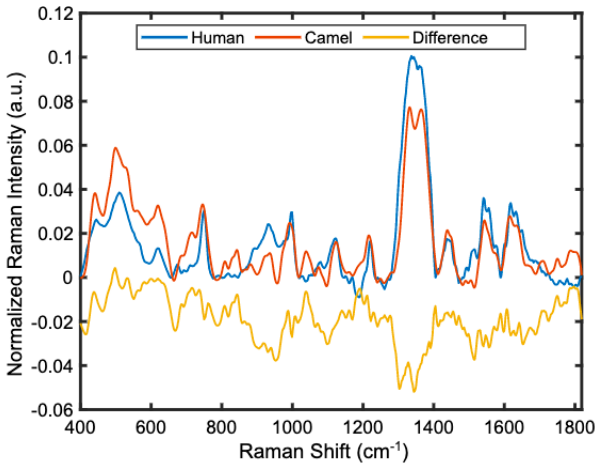

Figure 4.4. Raman spectrum of the two groups indicates dramatic differences in some bands' intensities: 540 cm^{-1}, 714 cm^{-1}, 1080 cm^{-1}. The bands, 838 cm^{-1}, and 945 cm^{-1}, are absent on the human spectrum, while these bands are Raman-active on the camel spectrum.

Raman spectra of whole blood of the camel and human groups (Figure 4.4) show the difference in peak intensities at 540 cm^{-1} band, which is assigned to S-S signal. This band is reported as the sign of integral proteins of the cell membrane [23, 165]. The amount of the integral proteins was reported 5 times greater in camel erythrocytes compared to human erythrocytes [143].

We observed that the spectral intensity of the 540 cm^{-1} band of the camels is twice as much of humans. The Raman signal from 714 cm^{-1} was assigned to phospholipid membranes. The current literature shows that RBC membrane structures are different in humans and camels. Our data indicate that Raman intensity at 714 cm^{-1} is higher in camels than in humans (see Figure 4.5).

Such a difference may point out the structural difference between these two cell types. The two wavenumbers in the spectrum, that is 838 cm^{-1} and 945 cm^{-1}, are absent for humans, while these wavenumbers are Raman-active for camels. The band, 838 cm^{-1} was assigned to tyrosine [166,167] and deformative vibrations of amine groups. The Raman signal of the camel blood at these peak remains inconclusive.

Table 4.1. The band assignments of human and camel RBCs' Raman spectra.

RS(cm^{-1})	**Normalized Raman Intensity (a.u.)**		**Assignment**
	Human	**Camel**	
540	0.0022± 0.0078	0.0042 ± 0.0009	S-S
714	0.0052 ± 0.0007	0.0277 ± 0.0031	C-N
838	absent	0.0303 ± 0.0017	tyrosine
945	absent	0.0144 ± 0.0034	polysaccharides, amylose
998	0.0264 ± 0.0026	0.0396 ± 0.0028	$\nu(C_\beta C_1)_{asym}$
1080	0.0074 ± 0.0026	0.0190 ± 0.0043	$\nu(C_\beta C_1)_{asym}$, phospholipids
1123	0.0047 ± 0.0025	0.0300 ± 0.0031	ν(pyr half-ring)$_{asym}$
1220	0.0254 ± 0.0061	0.0388 ± 0.0027	$\delta(C_mH)$, amide III
1305	0.0493 ± 0.0009	0.0338 ± 0.0049	$\delta(C_mH)$
1368	0.0920 ± 0.0008	0.0854 ± 0.0119	heme, ν(pyr half-ring)$_{sym}$
1439	0.0161 ± 0.0006	0.0273 ± 0.0078	$\delta(CH_2/CH_3)$
1557	0.0326 ± 0.0058	0.0343 ± 0.0023	$\nu(C_\beta C_\beta)_{sym}$
1650	0.0214 ± 0.0020	0.0094 ± 0.0020	(C=C) Amide I

The band, 945 cm^{-1}, was assigned to polysaccharides and amylose. It was reported that camels have high blood glucose levels [168]. In addition, the same study compared the amylase levels in camels as monogastric animals and humans as ruminant animals and found that intestinal amylase level is much higher in camels.

Therefore, the main difference observed in 945 cm^{-1} for the two groups may stem from being monogastric or ruminant animals [168]. Intensities of the peaks at 1368 cm^{-1} [169], which shows blood hemoglobin concentration level, are very close to each other for the two groups.

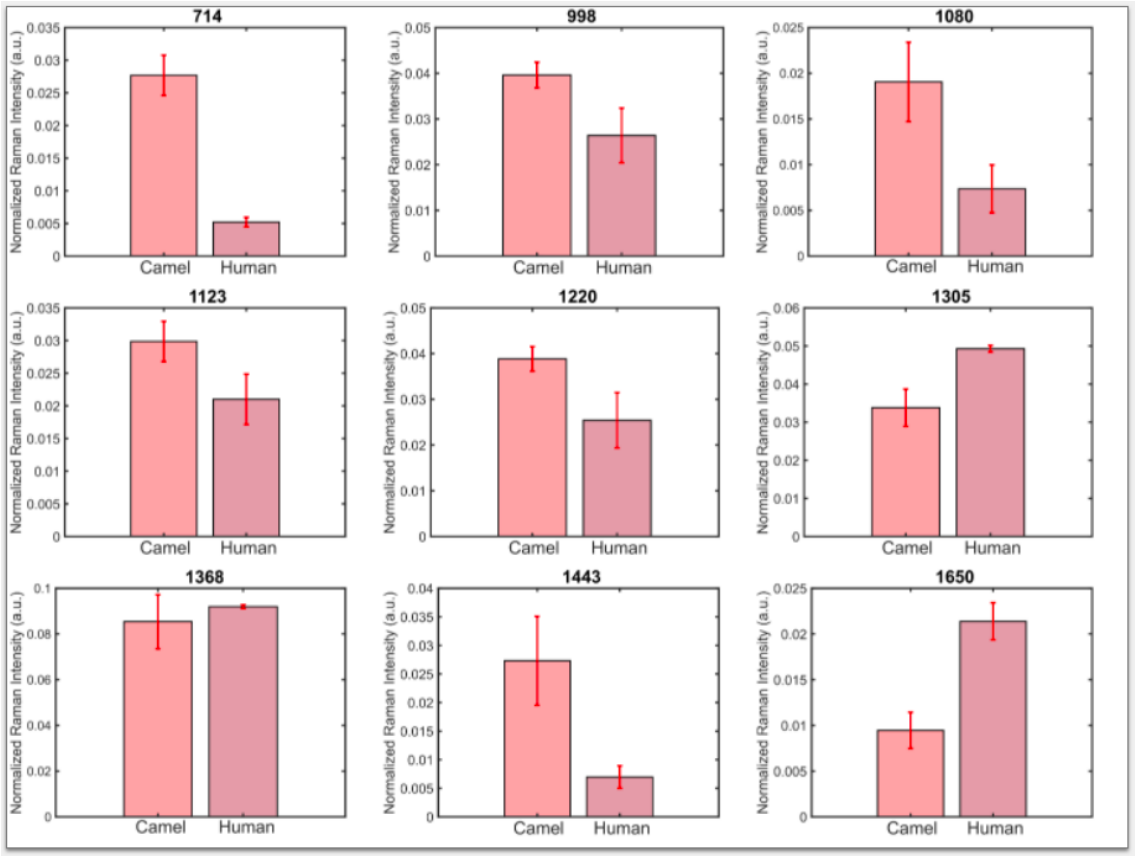

Figure 4.5. The bar graph shows the selected peak Raman intensities after band component analysis. These peak intensities are correlated to the amount of lipid and protein compositions; 714 cm^{-1} and 1080 cm^{-1} phospholipids, 1220 cm^{-1} amide III, 1305 cm^{-1} and 1439 cm^{-1} lipids, and 1650 cm^{-1} amide I.

4.4. Conclusion

Cells are complex systems such that mechanical and chemical stimuli drive each other. With such complex and crowded lipid/protein compositions, it is challenging to attribute cells' mechanical behaviors to specific lipid/protein types. Instead, deforming cells and observing their mechanical behaviors is another way of grasping cell mechanics. In this work, we aimed to investigate the most different cell types among the vertebrates, which is camel erythrocytes compared to human erythrocytes. Examining the deformation characteristics of the cells using optical tweezers gave some results such that their deformabilities are one order of magnitude apart from each other. In addition, the whole blood analysis of the two species using Raman spectroscopy shed some

light on the chemical content of these two types of cells, which are closely related to the mechanical features to some extent. However, we were unable to do single-cell Raman spectral measurement due to our technical limitations; instead, we measured the whole blood. To further improve our findings, one can do single-cell Raman measurements as a complement to cell deformation experiments to get more precise results.

5. SUMMARY

In this thesis, two powerful measurement techniques, namely, Raman spectroscopy and optical tweezers, were applied to biological problems on disease diagnostic techniques and cell mechanics.

In the first study, we aimed to develop a non-invasive diagnostic technique for endometriosis disease. Our motivation in this study was that until now, the definitive diagnosis of this disease was only possible with laparoscopy, which is an invasive method, so a non-invasive diagnostic method would be cheaper and more patient-friendly. The biomarkers of this disease are some types of proteins and changes in the blood. We aim to trace these changes in the blood serum. Since Raman spectroscopy can detect these kinds of changes in blood, it was utilized for this work. In addition to that, some machine learning algorithms were applied to our data to build up a model for diagnostics of the disease using the Raman spectra. We showed that Raman spectroscopy, together with machine learning algorithms, has the potential to develop a non-invasive diagnostic tool for endometriosis. Our published article of this work can be reviewed for further considerations [170].

Our second project concentrated on studying the universal mechanical behaviors of cells. Cells are complex dynamic organisms in which chemical and mechanical stimuli drive each other to regulate the cell's metabolic activities. Understanding the cell mechanics of such complex organisms is challenging with our current technology. However, certain behaviors have been observed even though the exact reasons for these behaviors are still unknown. We investigated two of these characteristic behaviors on red blood cells which are strain-stiffening and power-law behaviors. Until now, studies about the universal cell behaviors have been carried out using MTC and AFM modalities. With these modalities it is possible to examine cells from a small portion. It is not possible to create physical stimuli at the whole-cell-level. However, optical tweezers are quite well to intervene a cell as a whole, such that, one can hold on the cell from the two ends and stretch it as a whole body.

In the final study, we compare the camel and the human erythrocytes in terms of their mechanical and chemical features using Raman spectroscopy and optical tweezers. The focus of this project was doing a comparative analysis of the most distinctive erythrocytes, which belong to camels, relative to human erythrocytes. The deformability of the cells is quantified using optical tweezers, and it found that human erythrocytes are almost ten times more deformable than camel erythrocytes. The chemical features of these two species' blood samples were analyzed using Raman spectroscopy. According to the spectral data, we indicated that the lipid and protein content of the two groups differ from each other. However, we were unable to do single-cell Raman spectroscopy. Our data shows the Raman spectrum of the whole blood instead. This work can be improved by ding single-cell Raman spectroscopy for directly In order to correlate the information obtained with Raman measurements directly with the mechanical properties.

The studies in this thesis focused on developing non-invasive diagnostic methods and understanding cells' mechanical behaviors by utilizing Raman spectroscopy and optical tweezers [40, 170].

REFERENCES

1. Tao, J., Y. Li, D. K. Vig and S. X. Sun, "Cell Mechanics: A Dialogue", *Reports on Progress in Physics*, Vol. 80, No. 3, p. 036601, 2017.

2. Barabino, G. A., M. O. Platt and D. K. Kaul, "Sickle Cell Biomechanics", *Annual Review of Biomedical Engineering*, Vol. 12, pp. 345–367, 2010.

3. Maciaszek, J. L. and G. Lykotrafitis, "Sickle Cell Trait Human Erythrocytes are Significantly Stiffer Than Normal", *Journal of Biomechanics*, Vol. 44, No. 4, pp. 657–661, 2011.

4. Agrawal, R., T. Smart, J. Nobre-Cardoso, C. Richards, R. Bhatnagar, A. Tufail, D. Shima, P. H. Jones and C. Pavesio, "Assessment of Red Blood Cell Deformability in Type 2 Diabetes Mellitus and Diabetic Retinopathy by Dual Optical Tweezers Stretching Technique", *Scientific Reports*, Vol. 6, p. 15873, 2016.

5. LIM, C. T., "Single Cell Mechanics Study of the Human Disease Malaria", *Journal of Biomechanical Science and Engineering*, Vol. 1, No. 1, pp. 82–92, 2006.

6. Alenghat, F. J., B. Fabry, K. Y. Tsai, W. H. Goldmann and D. E. Ingber, "Analysis of Cell Mechanics in Single Vinculin-deficient Cells Using a Magnetic Tweezer", *Biochemical and Biophysical Research Communications*, Vol. 277, No. 1, pp. 93–99, 2000.

7. Rianna, C. and M. Radmacher, "Cell Mechanics as a Marker for Diseases: Biomedical Applications of AFM", *AIP Conference Proceedings*, Vol. 1760, p. 020057, AIP Publishing LLC, 2016.

8. Lekka, M., "Discrimination Between Normal and Cancerous Cells Using AFM", *Bionanoscience*, Vol. 6, No. 1, pp. 65–80, 2016.

9. Miura, K. and S. Yamamoto, "A Scanning Acoustic Microscope Discriminates Cancer Cells in Fluid", *Scientific Reports*, Vol. 5, No. 1, pp. 1–11, 2015.

10. Caponi, S., S. Mattana, M. Mattarelli, M. A. Cardinali, L. Urbanelli, K. Sagini, C. Emiliani and D. Fioretto, "Correlative Brillouin and Raman Spectroscopy Data Acquired on Single Cells", *Data in Brief*, Vol. 29, p. 105223, 2020.

11. Majzner, K., S. Tott, L. Roussille, V. Deckert, S. Chlopicki and M. Baranska, "Uptake of Fatty Acids by a Single Endothelial Cell Investigated by Raman Spectroscopy Supported by AFM", *Analyst*, Vol. 143, No. 4, pp. 970–980, 2018.

12. Sorkin, R., G. Bergamaschi, D. Kamsma, G. Brand, E. Dekel, Y. Ofir-Birin, A. Rudik, M. Gironella, F. Ritort, N. Regev-Rudzki *et al.*, "Probing Cellular Mechanics with Acoustic Force Spectroscopy", *Molecular Biology of the Cell*, Vol. 29, No. 16, pp. 2005–2011, 2018.

13. Silvani, G., V. Romanov, C. D. Cox and B. Martinac, "Biomechanical Characterization of Endothelial Cells Exposed to Shear Stress Using Acoustic Force Spectroscopy", *Frontiers in Bioengineering and Biotechnology*, Vol. 9, p. 21, 2021.

14. Trepat, X., G. Lenormand and J. J. Fredberg, "Universality in Cell Mechanics", *Soft Matter*, Vol. 4, No. 9, pp. 1750–1759, 2008.

15. Balland, M., N. Desprat, D. Icard, S. Féréol, A. Asnacios, J. Browaeys, S. Hénon and F. Gallet, "Power Laws in Microrheology Experiments on Living Cells: Comparative Analysis and Modeling", *Physical Review E*, Vol. 74, No. 2, p. 021911, 2006.

16. Bursac, P., G. Lenormand, B. Fabry, M. Oliver, D. A. Weitz, V. Viasnoff, J. P. Butler and J. J. Fredberg, "Cytoskeletal Remodelling and Slow Dynamics in the Living Cell", *Nature Materials*, Vol. 4, No. 7, pp. 557–561, 2005.

17. Moeendarbary, E. and A. R. Harris, "Cell Mechanics: Principles, Practices,

and Prospects", *Wiley Interdisciplinary Reviews: Systems Biology and Medicine*, Vol. 6, No. 5, pp. 371–388, 2014.

18. Bu, Y., L. Li, C. Yang, R. Li and J. Wang, "Measuring Viscoelastic Properties of Living Cells", *Acta Mechanica Solida Sinica*, Vol. 32, No. 5, pp. 599–610, 2019.

19. Moreno-Flores, S., R. Benitez, M. dM Vivanco and J. L. Toca-Herrera, "Stress Relaxation Microscopy: Imaging Local Stress in Cells", *Journal of Biomechanics*, Vol. 43, No. 2, pp. 349–354, 2010.

20. Nasdala, L., D. C. Smith, R. Kaindl, M. A. Ziemann *et al.*, "Raman Spectroscopy: Analytical Perspectives in Mineralogical Research", *Spectroscopic Methods in Mineralogy*, Vol. 6, pp. 281–343, 2004.

21. Raman, C. V., "A New Radiation", *Indian Journal of Physics*, Vol. 2, pp. 387–398, 1928.

22. Raman, C. V. and K. S. Krishnan, "A New Type of Secondary Radiation", *Nature*, Vol. 121, No. 3048, pp. 501–502, 1928.

23. Nakamoto, K., *Infrared and Raman Spectra of Inorganic and Coordination Compounds, Part B: Applications in Coordination, Organometallic, and Bioinorganic Chemistry*, John Wiley & Sons, 2009.

24. Ashkin, A., "Acceleration and Trapping of Particles by Radiation Pressure", *Physical Review Letters*, Vol. 24, No. 4, p. 156, 1970.

25. Ashkin, A., "History of Optical Trapping and Manipulation of Small-neutral Particle, Atoms, and Molecules", *IEEE Journal of Selected Topics in Quantum Electronics*, Vol. 6, No. 6, pp. 841–856, 2000.

26. Zhu, R., T. Avsievich, A. Popov and I. Meglinski, "Optical Tweezers in Studies of Red Blood Cells", *Cells*, Vol. 9, No. 3, p. 545, 2020.

27. Ashkin, A., "Optical Trapping and Manipulation of Neutral Particles Using Lasers", *Proceedings of the National Academy of Sciences*, Vol. 94, No. 10, pp. 4853–4860, 1997.

28. Boyde, L., A. Ekpenyong, G. Whyte and J. Guck, "Comparison of Stresses on Homogeneous Spheroids in the Optical Stretcher Computed with Geometrical Optics and Generalized Lorenz–Mie Theory", *Applied Optics*, Vol. 51, No. 33, pp. 7934–7944, 2012.

29. Kalume, A., C. Wang and Y.-L. Pan, "Optical-trapping Laser Techniques for Characterizing Airborne Aerosol Particles and Its Application in Chemical Aerosol Study", *Micromachines*, Vol. 12, No. 4, p. 466, 2021.

30. Kerker, M., *The Scattering of Light and Other Electromagnetic Radiation: Physical Chemistry: a Series of Monographs*, Vol. 16, Academic Press, 2013.

31. Harada, Y. and T. Asakura, "Radiation Forces on a Dielectric Sphere in the Rayleigh Scattering Regime", *Optics Communications*, Vol. 124, No. 5-6, pp. 529–541, 1996.

32. Ashkin, A., "Forces of a Single-beam Gradient Laser Trap on a Dielectric Sphere in the Ray Optics Regime", *Biophysical Journal*, Vol. 61, No. 2, pp. 569–582, 1992.

33. Guck, J., R. Ananthakrishnan, T. J. Moon, C. Cunningham and J. Käs, "Optical Deformability of Soft Biological Dielectrics", *Physical Review Letters*, Vol. 84, No. 23, p. 5451, 2000.

34. Ashkin, A., J. M. Dziedzic and T. Yamane, "Optical Trapping and Manipulation of Single Cells Using Infrared Laser Beams", *Nature*, Vol. 330, No. 6150, pp. 769–771, 1987.

35. Ashkin, A., J. M. Dziedzic and T. Yamane, "Optical Trapping and Manipulation

of Single Cells Using Infrared Laser Beams", *Nature*, Vol. 330, No. 6150, pp. 769–771, 1987.

36. Berns, M. W., W. H. Wright, B. J. Tromberg, G. A. Profeta, J. J. Andrews and R. J. Walter, "Use of a Laser-induced Optical Force Trap to Study Chromosome Movement on the Mitotic Spindle", *Proceedings of the National Academy of Sciences*, Vol. 86, No. 12, pp. 4539–4543, 1989.

37. Nascimento, J., E. L. Botvinick, L. Z. Shi, B. Durrant and M. W. Berns, "Analysis of Sperm Motility Using Optical Tweezers", *Journal of Biomedical Optics*, Vol. 11, No. 4, p. 044001, 2006.

38. Hyun, N., C. Chandsawangbhuwana, C. Yang-Wong, M. W. Berns, Q. Zhu and L. Z. Shi, "Effects of Viscosity on Sperm Motility Studied with Optical Tweezers", *Journal of Biomedical Optics*, Vol. 17, No. 2, p. 025005, 2012.

39. Mills, J., L. Qie, M. Dao, C. Lim and S. Suresh, "Nonlinear Elastic and Viscoelastic Deformation of the Human Red Blood Cell with Optical Tweezers", *Molecular*

&

Cellular Biomechanics, Vol. 1, No. 3, p. 169, 2004.

40. Inanc, M. T., I. Demirkan, C. Ceylan, A. Ozkan, O. Gundogdu, U. Goreke, U. A. Gurkan and M. B. Unlu, "Quantifying the Influences of Radiation Therapy on Deformability of Human Red Blood Cells by Dual-beam Optical Tweezers", *Rsc Advances*, Vol. 11, No. 26, pp. 15519–15527, 2021.

41. Lee, K., A. V. Danilina, M. Kinnunen, A. V. Priezzhev and I. Meglinski, "Probing the Red Blood Cells Aggregating Force with Optical Tweezers", *IEEE Journal of Selected Topics in Quantum Electronics*, Vol. 22, No. 3, pp. 365–370, 2015.

42. Lee, K., M. Kinnunen, M. D. Khokhlova, E. V. Lyubin, A. V. Priezzhev, I. Meglin-

ski and A. A. Fedyanin, "Optical Tweezers Study of Red Blood Cell Aggregation and Disaggregation in Plasma and Protein Solutions", *Journal of Biomedical Optics*, Vol. 21, No. 3, p. 035001, 2016.

43. Gou, X., H. C. Han, S. Hu, A. Y. Leung and D. Sun, "Applying Combined Optical Tweezers and Fluorescence Microscopy Technologies to Manipulate Cell Adhesions for Cell-to-cell Interaction Study", *IEEE Transactions on Biomedical Engineering*, Vol. 60, No. 8, pp. 2308–2315, 2013.

44. Schwingel, M. and M. Bastmeyer, "Force Mapping During the Formation and Maturation of Cell Adhesion Sites with Multiple Optical Tweezers", *Plos One*, Vol. 8, No. 1, p. e54850, 2013.

45. Yousafzai, M. S., G. Coceano, S. Bonin, J. Niemela, G. Scoles and D. Cojoc, "Investigating the Effect of Cell Substrate on Cancer Cell Stiffness by Optical Tweezers", *Journal of Biomechanics*, Vol. 60, pp. 266–269, 2017.

46. Hong-Lian, G., L. Chun-Xiang, D. Jian-Fa, J. Yu-Qiang, H. Xue-Hai, L. Zhao-Lin, C. Bing-Ying and Z. Dao-Zhong, "Mechanical Properties of Breast Cancer Cell Membrane Studied with Optical Tweezers", *Chinese Physics Letters*, Vol. 21, No. 12, p. 2543, 2004.

47. Tavano, F., S. Bonin, G. Pinato, G. Stanta and D. Cojoc, "Custom-built Optical Tweezers for Locally Probing the Viscoelastic Properties of Cancer Cells", *International Journal of Optomechatronics*, Vol. 5, No. 3, pp. 234–248, 2011.

48. Lenton, I. C., E. K. Scott, H. Rubinsztein-Dunlop and I. A. Favre-Bulle, "Optical Tweezers Exploring Neuroscience", *Frontiers in Bioengineering and Biotechnology*, p. 1360, 2020.

49. Mohanty, S. K., M. Sharma, M. M. Panicker and P. K. Gupta, "Controlled Induction, Enhancement, and Guidance of Neuronal Growth Cones by Use of Line Optical Tweezers", *Optics Letters*, Vol. 30, No. 19, pp. 2596–2598, 2005.

50. Fuldeore, M. J. and A. M. Soliman, "Prevalence and Symptomatic Burden of Diagnosed Endometriosis in the United States: National Estimates From a Cross-sectional Survey of 59,411 Women", *Gynecologic and Obstetric Investigation*, Vol. 82, No. 5, pp. 453–461, 2017.

51. Ferraro, J. R., *Introductory Raman Spectroscopy*, Elsevier, 2003.

52. Vodolazkaia, A., Y. El-Aalamat, D. Popovic, A. Mihalyi, X. Bossuyt, C. Kyama, A. Fassbender, A. Bokor, D. Schols, D. Huskens *et al.*, "Evaluation of a Panel of 28 Biomarkers for the Non-invasive Diagnosis of Endometriosis", *Human Reproduction*, Vol. 27, No. 9, pp. 2698–2711, 2012.

53. Choo-Smith, L.-P., H. Edwards, H. P. Endtz, J. Kros, F. Heule, H. Barr, J. S. Robinson Jr, H. Bruining and G. Puppels, "Medical Applications of Raman Spectroscopy: From Proof of Principle to Clinical Implementation", *Biopolymers: Original Research on Biomolecules*, Vol. 67, No. 1, pp. 1–9, 2002.

54. Ryzhikova, E., O. Kazakov, L. Halamkova, D. Celmins, P. Malone, E. Molho, E. A. Zimmerman and I. K. Lednev, "Raman Spectroscopy of Blood Serum for Alzheimer's Disease Diagnostics: Specificity Relative to Other Types of Dementia", *Journal of Biophotonics*, Vol. 8, No. 7, pp. 584–596, 2015.

55. Sahu, A., S. Sawant, H. Mamgain and C. M. Krishna, "Raman Spectroscopy of Serum: An Exploratory Study for Detection of Oral Cancers", *Analyst*, Vol. 138, No. 14, pp. 4161–4174, 2013.

56. Feng, S., R. Chen, J. Lin, J. Pan, G. Chen, Y. Li, M. Cheng, Z. Huang, J. Chen and H. Zeng, "Nasopharyngeal Cancer Detection Based on Blood Plasma Surface-enhanced Raman Spectroscopy and Multivariate Analysis", *Biosensors and Bioelectronics*, Vol. 25, No. 11, pp. 2414–2419, 2010.

57. Lin, D., S. Feng, J. Pan, Y. Chen, J. Lin, G. Chen, S. Xie, H. Zeng and R. Chen, "Colorectal Cancer Detection by Gold Nanoparticle Based Surface-enhanced Ra-

man Spectroscopy of Blood Serum and Statistical Analysis", *Optics Express*, Vol. 19, No. 14, pp. 13565–13577, 2011.

58. Mahmood, T., H. Nawaz, A. Ditta, M. Majeed, M. Hanif, N. Rashid, H. Bhatti, H. Nargis, M. Saleem, F. Bonnier *et al.*, "Raman Spectral Analysis for Rapid Screening of Dengue Infection", *Spectrochimica Acta Part A: Molecular and Biomolecular Spectroscopy*, Vol. 200, pp. 136–142, 2018.

59. Huang, Z., A. McWilliams, H. Lui, D. I. McLean, S. Lam and H. Zeng, "Near-infrared Raman Spectroscopy for Optical Diagnosis of Lung Cancer", *International Journal of Cancer*, Vol. 107, No. 6, pp. 1047–1052, 2003.

60. Kamińska, A., E. Witkowska, K. Winkler, I. Dziecielewski, J. L. Weyher and J. Waluk, "Detection of Hepatitis B Virus Antigen From Human Blood: SERS Immunoassay in a Microfluidic System", *Biosensors and Bioelectronics*, Vol. 66, pp. 461–467, 2015.

61. Pichardo-Molina, J., C. Frausto-Reyes, O. Barbosa-García, R. Huerta-Franco, J. González-Trujillo, C. Ramírez-Alvarado, G. Gutiérrez-Juárez and C. Medina-Gutiérrez, "Raman Spectroscopy and Multivariate Analysis of Serum Samples From Breast Cancer Patients", *Lasers in Medical Science*, Vol. 22, No. 4, pp. 229–236, 2007.

62. Lieber, C. A., K. Molpus, K. Brader and A. Mahadevan-Jansen, "Diagnostic Tool for Early Detection of Ovarian Cancers Using Raman Spectroscopy", *Biomedical Spectroscopy: Vibrational Spectroscopy and Other Novel Techniques*, Vol. 3918, pp. 129–135, International Society for Optics and Photonics, 2000.

63. Patel, I. I., J. Trevisan, G. Evans, V. Llabjani, P. L. Martin-Hirsch, H. F. Stringfellow and F. L. Martin, "High Contrast Images of Uterine Tissue Derived Using Raman Microspectroscopy with the Empty Modelling Approach of Multivariate Curve Resolution-alternating Least Squares", *Analyst*, Vol. 136, No. 23, pp. 4950–4959, 2011.

64. Notarstefano, V., G. Gioacchini, H. J. Byrne, C. Zacà, E. Sereni, L. Vaccari, A. Borini, O. Carnevali and E. Giorgini, "Vibrational Characterization of Granulosa Cells From Patients Affected by Unilateral Ovarian Endometriosis: New Insights From Infrared and Raman Microspectroscopy", *Spectrochimica Acta Part A: Molecular and Biomolecular Spectroscopy*, Vol. 212, pp. 206–214, 2019.

65. Cover, T. and P. Hart, "Nearest Neighbor Pattern Classification", *IEEE Transactions on Information Theory*, Vol. 13, No. 1, pp. 21–27, 1967.

66. Vapnik, V. N., *The Nature of Statistical Learning Theory*, Springer-Verlag, Berlin, Heidelberg, 1995.

67. Lin, W., X. Yuan, P. W. Yuen, W. I. Wei, J. Sham, P.-C. Shi and J. Y. Qu, "Classification of in Vivo Autofluorescence Spectra Using Support Vector Machines", *Journal of Biomedical Optics*, Vol. 9, No. 1, pp. 180–187, 2004.

68. Palmer, G. M., C. Zhu, T. M. Breslin, F. Xu, K. W. Gilchrist and N. Ramanujam, "Comparison of Multiexcitation Fluorescence and Diffuse Reflectance Spectroscopy for the Diagnosis of Breast Cancer (March 2003)", *IEEE Transactions on Biomedical Engineering*, Vol. 50, No. 11, pp. 1233–1242, 2003.

69. Majumder, S., N. Ghosh and P. K. Gupta, "Support Vector Machine for Optical Diagnosis of Cancer", *Journal of Biomedical Optics*, Vol. 10, No. 2, p. 024034, 2005.

70. Zomer, S., R. G. Brereton, J. F. Carter and C. Eckers, "Support Vector Machines for the Discrimination of Analytical Chemical Data: Application to the Determination of Tablet Production by Pyrolysis-gas Chromatography-mass Spectrometry", *Analyst*, Vol. 129, No. 2, pp. 175–181, 2004.

71. Dingari, N. C., I. Barman, A. Saha, S. McGee, L. H. Galindo, W. Liu, D. Plecha, N. Klein, R. R. Dasari and M. Fitzmaurice, "Development and Comparative Assessment of Raman Spectroscopic Classification Algorithms for Lesion Discrimi-

nation in Stereotactic Breast Biopsies with Microcalcifications", *Journal of Biophotonics*, Vol. 6, No. 4, pp. 371–381, 2013.

72. Li, X., T. Yang, S. Li, D. Wang, Y. Song and S. Zhang, "Raman Spectroscopy Combined with Principal Component Analysis and K Nearest Neighbour Analysis for Non-invasive Detection of Colon Cancer", *Laser Physics*, Vol. 26, No. 3, p. 035702, 2016.

73. Başar, G., U. Parlatan, Ş. Şeninak, T. Günel, A. Benian and İ. Kalelioğlu, "Investigation of Preeclampsia Using Raman Spectroscopy", *Journal of Spectroscopy*, Vol. 27, No. 4, pp. 239–252, 2012.

74. Hernández, B., F. Pflüger, S. G. Kruglik and M. Ghomi, "Characteristic Raman Lines of Phenylalanine Analyzed by a Multiconformational Approach", *Journal of Raman Spectroscopy*, Vol. 44, No. 6, pp. 827–833, 2013.

75. Vítek, P., K. Osterrothová and J. Jehlička, "Beta-carotene-A Possible Biomarker in the Martian Evaporitic Environment: Raman Micro-spectroscopic Study", *Planetary and Space Science*, Vol. 57, No. 4, pp. 454–459, 2009.

76. Yamagata, Y., E. Takaki, M. Shinagawa, M. Okada, K. Jozaki, L. Lee, S. Sato, R. Maekawa, T. Taketani, H. Asada *et al.*, "Retinoic Acid Has the Potential to Suppress Endometriosis Development", *Journal of Ovarian Research*, Vol. 8, No. 1, p. 49, 2015.

77. Taylor, R. N., M. A. Kane and N. Sidell, "Pathogenesis of Endometriosis: Roles of Retinoids and Inflammatory Pathways", *Seminars in Reproductive Medicine*, Vol. 33, pp. 246–256, Thieme Medical Publishers, 2015.

78. Smith, A. S., R. B. Nowak, S. Zhou, M. Giannetto, D. S. Gokhin, J. Papoin, I. C. Ghiran, L. Blanc, J. Wan and V. M. Fowler, "Myosin Iia Interacts with the Spectrin-actin Membrane Skeleton to Control Red Blood Cell Membrane Curvature and Deformability", *Proceedings of the National Academy of Sciences*, Vol.

115, No. 19, pp. E4377–E4385, 2018.

79. Dao, M., C. T. Lim and S. Suresh, "Mechanics of the Human Red Blood Cell Deformed by Optical Tweezers", *Journal of the Mechanics and Physics of Solids*, Vol. 51, No. 11-12, pp. 2259–2280, 2003.

80. Qiang, Y., J. Liu, M. Dao, S. Suresh and E. Du, "Mechanical Fatigue of Human Red Blood Cells", *Proceedings of the National Academy of Sciences*, Vol. 116, No. 40, pp. 19828–19834, 2019.

81. Lux IV, S. E., "Anatomy of the Red Cell Membrane Skeleton: Unanswered Questions", *Blood, the Journal of the American Society of Hematology*, Vol. 127, No. 2, pp. 187–199, 2016.

82. Pesciotta, E. N., S. Sriswasdi, H.-Y. Tang, P. J. Mason, M. Bessler and D. W. Speicher, "A Label-free Proteome Analysis Strategy for Identifying Quantitative Changes in Erythrocyte Membranes Induced by Red Cell Disorders", *Journal of Proteomics*, Vol. 76, pp. 194–202, 2012.

83. Saito, M., T. Watanabe-Nakayama, S. Machida, T. Osada, R. Afrin and A. Ikai, "Spectrin–ankyrin Interaction Mechanics: A Key Force Balance Factor in the Red Blood Cell Membrane Skeleton", *Biophysical Chemistry*, Vol. 200, pp. 1–8, 2015.

84. Jacobs, C. R., H. Huang and R. Y. Kwon, *Introduction to Cell Mechanics and Mechanobiology*, Garland Science, 2012.

85. Byers, T. J. and D. Branton, "Visualization of the Protein Associations in the Erythrocyte Membrane Skeleton", *Proceedings of the National Academy of Sciences*, Vol. 82, No. 18, pp. 6153–6157, 1985.

86. Wang, N., I. M. Tolic-Nørrelykke, J. Chen, S. M. Mijailovich, J. P. Butler, J. J. Fredberg and D. Stamenovic, "Cell Prestress. I. Stiffness and Prestress are Closely Associated in Adherent Contractile Cells", *American Journal of Physiology-cell*

Physiology, Vol. 282, No. 3, pp. C606–C616, 2002.

87. Kumar, S., I. Z. Maxwell, A. Heisterkamp, T. R. Polte, T. P. Lele, M. Salanga, E. Mazur and D. E. Ingber, "Viscoelastic Retraction of Single Living Stress Fibers and Its Impact on Cell Shape, Cytoskeletal Organization, and Extracellular Matrix Mechanics", *Biophysical Journal*, Vol. 90, No. 10, pp. 3762–3773, 2006.

88. Ingber, D. E., "Tensegrity: The Architectural Basis of Cellular Mechanotransduction", *Annual Review of Physiology*, Vol. 59, No. 1, pp. 575–599, 1997.

89. Ingber, D. E., "Tensegrity I. Cell Structure and Hierarchical Systems Biology", *Journal of Cell Science*, Vol. 116, No. 7, pp. 1157–1173, 2003.

90. Ingber, D. E., "Cellular Tensegrity: Defining New Rules of Biological Design That Govern the Cytoskeleton", *Journal of Cell Science*, Vol. 104, No. 3, pp. 613–627, 1993.

91. Trepat, X., L. Deng, S. S. An, D. Navajas, D. J. Tschumperlin, W. T. Gerthoffer, J. P. Butler and J. J. Fredberg, "Universal Physical Responses to Stretch in the Living Cell", *Nature*, Vol. 447, No. 7144, pp. 592–595, 2007.

92. Fabry, B., G. N. Maksym, J. P. Butler, M. Glogauer, D. Navajas and J. J. Fredberg, "Scaling the Microrheology of Living Cells", *Physical Review Letters*, Vol. 87, No. 14, p. 148102, 2001.

93. Deng, L., X. Trepat, J. P. Butler, E. Millet, K. G. Morgan, D. A. Weitz and J. J. Fredberg, "Fast and Slow Dynamics of the Cytoskeleton", *Nature Materials*, Vol. 5, No. 8, pp. 636–640, 2006.

94. Hoffman, B. D. and J. C. Crocker, "Cell Mechanics: Dissecting the Physical Responses of Cells to Force", *Annual Review of Biomedical Engineering*, Vol. 11, pp. 259–288, 2009.

95. Lenormand, G., J. Chopin, P. Bursac, J. J. Fredberg and J. P. Butler, "Directional

Memory and Caged Dynamics in Cytoskeletal Remodelling", *Biochemical and Biophysical Research Communications*, Vol. 360, No. 4, pp. 797–801, 2007.

96. Gardel, M., J. H. Shin, F. MacKintosh, L. Mahadevan, P. Matsudaira and D. Weitz, "Elastic Behavior of Cross-linked and Bundled Actin Networks", *Science*, Vol. 304, No. 5675, pp. 1301–1305, 2004.

97. Glogauer, M., P. Arora, D. Chou, P. A. Janmey, G. P. Downey and C. A. McCulloch, "The Role of Actin-binding Protein 280 in Integrin-dependent Mechanoprotection", *Journal of Biological Chemistry*, Vol. 273, No. 3, pp. 1689–1698, 1998.

98. Gardel, M., F. Nakamura, J. Hartwig, J. C. Crocker, T. Stossel and D. Weitz, "Stress-dependent Elasticity of Composite Actin Networks as a Model for Cell Behavior", *Physical Review Letters*, Vol. 96, No. 8, p. 088102, 2006.

99. Kollmannsberger, P. and B. Fabry, "Linear and Nonlinear Rheology of Living Cells", *Annual Review of Materials Research*, Vol. 41, pp. 75–97, 2011.

100. Yap, B. and R. D. Kamm, "Cytoskeletal Remodeling and Cellular Activation During Deformation of Neutrophils into Narrow Channels", *Journal of Applied Physiology*, Vol. 99, No. 6, pp. 2323–2330, 2005.

101. Kollmannsberger, P., C. T. Mierke and B. Fabry, "Nonlinear Viscoelasticity of Adherent Cells is Controlled by Cytoskeletal Tension", *Soft Matter*, Vol. 7, No. 7, pp. 3127–3132, 2011.

102. Weitz, D. and P. Janmey, "The Soft Framework of the Cellular Machine", *Proceedings of the National Academy of Sciences*, Vol. 105, No. 4, pp. 1105–1106, 2008.

103. An, S. S., B. Fabry, X. Trepat, N. Wang and J. J. Fredberg, "Do Biophysical Properties of the Airway Smooth Muscle in Culture Predict Airway Hyperresponsiveness?", *American Journal of Respiratory Cell and Molecular Biology*, Vol. 35,

No. 1, pp. 55–64, 2006.

104. Kamble, H., M. J. Barton, M. Jun, S. Park and N.-T. Nguyen, "Cell Stretching Devices as Research Tools: Engineering and Biological Considerations", *Lab on a Chip*, Vol. 16, No. 17, pp. 3193–3203, 2016.

105. Caplin, J. D., N. G. Granados, M. R. James, R. Montazami and N. Hashemi, "Microfluidic Organ-on-a-chip Technology for Advancement of Drug Development and Toxicology", *Advanced Healthcare Materials*, Vol. 4, No. 10, pp. 1426–1450, 2015.

106. Bao, G. and S. Suresh, "Cell and Molecular Mechanics of Biological Materials", *Nature Materials*, Vol. 2, No. 11, pp. 715–725, 2003.

107. Zhang, H. and K.-K. Liu, "Optical Tweezers for Single Cells", *Journal of the Royal Society Interface*, Vol. 5, No. 24, pp. 671–690, 2008.

108. Laurent, V. r. M., S. He´ non, E. Planus, R. Fodil, M. Balland, D. Isabey and F. o. Gallet, "Assessment of Mechanical Properties of Adherent Living Cells by Bead Micromanipulation: Comparison of Magnetic Twisting Cytometry Vs Optical Tweezers", *J. Biomech. Eng.*, Vol. 124, No. 4, pp. 408–421, 2002.

109. Choquet, D., D. P. Felsenfeld and M. P. Sheetz, "Extracellular Matrix Rigidity Causes Strengthening of Integrin–cytoskeleton Linkages", *Cell*, Vol. 88, No. 1, pp. 39–48, 1997.

110. Arbore, C., L. Perego, M. Sergides and M. Capitanio, "Probing Force in Living Cells with Optical Tweezers: From Single-molecule Mechanics to Cell Mechanotransduction", *Biophysical Reviews*, Vol. 11, No. 5, pp. 765–782, 2019.

111. Sigüenza, J., S. Mendez and F. Nicoud, "How Should the Optical Tweezers Experiment Be Used to Characterize the Red Blood Cell Membrane Mechanics?", *Biomechanics and Modeling in Mechanobiology*, Vol. 16, No. 5, pp. 1645–1657,

2017.

112. Nussenzveig, H. M., "Cell Membrane Biophysics with Optical Tweezers", *European Biophysics Journal*, Vol. 47, No. 5, pp. 499–514, 2018.

113. Sheikh-Hasani, V., M. Babaei, A. Azadbakht, H. Pazoki-Toroudi, A. Mashaghi, A. A. Moosavi-Movahedi and S. N. S. Reihani, "Atorvastatin Treatment Softens Human Red Blood Cells: An Optical Tweezers Study", *Biomedical Optics Express*, Vol. 9, No. 3, pp. 1256–1261, 2018.

114. Lukose, J., G. Mohan, S. Shastry and S. Chidangil, "Optical Tweezers Combined with Micro-raman Investigation of Alcohol-induced Changes on Single, Live Red Blood Cells in Blood Plasma", *Journal of Raman Spectroscopy*, Vol. 50, No. 10, pp. 1367–1374, 2019.

115. Puig-de Morales-Marinkovic, M., K. T. Turner, J. P. Butler, J. J. Fredberg and S. Suresh, "Viscoelasticity of the Human Red Blood Cell", *American Journal of Physiology-cell Physiology*, Vol. 293, No. 2, pp. C597–C605, 2007.

116. Yoon, Y.-Z., J. Kotar, G. Yoon and P. Cicuta, "The Nonlinear Mechanical Response of the Red Blood Cell", *Physical Biology*, Vol. 5, No. 3, p. 036007, 2008.

117. Alcaraz, J., L. Buscemi, M. Grabulosa, X. Trepat, B. Fabry, R. Farré and D. Navajas, "Microrheology of Human Lung Epithelial Cells Measured by Atomic Force Microscopy", *Biophysical Journal*, Vol. 84, No. 3, pp. 2071–2079, 2003.

118. Zhong, M.-C., X.-B. Wei, J.-H. Zhou, Z.-Q. Wang and Y.-M. Li, "Trapping Red Blood Cells in Living Animals Using Optical Tweezers", *Nature Communications*, Vol. 4, No. 1, pp. 1–7, 2013.

119. Henon, S., G. Lenormand, A. Richert and F. Gallet, "A New Determination of the Shear Modulus of the Human Erythrocyte Membrane Using Optical Tweezers", *Biophysical Journal*, Vol. 76, No. 2, pp. 1145–1151, 1999.

120. Trepat, X., F. Puig, N. Gavara, J. J. Fredberg, R. Farre and D. Navajas, "Effect of Stretch on Structural Integrity and Micromechanics of Human Alveolar Epithelial Cell Monolayers Exposed to Thrombin", *American Journal of Physiology-lung Cellular and Molecular Physiology*, Vol. 290, No. 6, pp. L1104–L1110, 2006.

121. Wang, N. and D. E. Ingber, "Control of Cytoskeletal Mechanics by Extracellular Matrix, Cell Shape, and Mechanical Tension", *Biophysical Journal*, Vol. 66, No. 6, pp. 2181–2189, 1994.

122. Pollard, T. D. and J. A. Cooper, "Actin, a Central Player in Cell Shape and Movement", *Science*, Vol. 326, No. 5957, pp. 1208–1212, 2009.

123. Lemière, J., F. Valentino, C. Campillo and C. Sykes, "How Cellular Membrane Properties are Affected by the Actin Cytoskeleton", *Biochimie*, Vol. 130, pp. 33–40, 2016.

124. Matthews, B. D., D. R. Overby, R. Mannix and D. E. Ingber, "Cellular Adaptation to Mechanical Stress: Role of Integrins, Rho, Cytoskeletal Tension and Mechanosensitive Ion Channels", *Journal of Cell Science*, Vol. 119, No. 3, pp. 508–518, 2006.

125. Jiang, G., G. Giannone, D. R. Critchley, E. Fukumoto and M. P. Sheetz, "Two-piconewton Slip Bond Between Fibronectin and the Cytoskeleton Depends on Talin", *Nature*, Vol. 424, No. 6946, pp. 334–337, 2003.

126. Fai, T. G., A. Leo-Macias, D. L. Stokes and C. S. Peskin, "Image-based Model of the Spectrin Cytoskeleton for Red Blood Cell Simulation", *Plos Computational Biology*, Vol. 13, No. 10, p. e1005790, 2017.

127. Anderson, H. L., I. E. Brodsky and N. S. Mangalmurti, "The Evolving Erythrocyte: Red Blood Cells as Modulators of Innate Immunity", *The Journal of Immunology*, Vol. 201, No. 5, pp. 1343–1351, 2018.

128. Ji, P., M. Murata-Hori and H. F. Lodish, "Formation of Mammalian Erythrocytes: Chromatin Condensation and Enucleation", *Trends in Cell Biology*, Vol. 21, No. 7, pp. 409–415, 2011.

129. Snyder, G. K. and B. A. Sheafor, "Red Blood Cells: Centerpiece in the Evolution of the Vertebrate Circulatory System", *American Zoologist*, Vol. 39, No. 2, pp. 189–198, 1999.

130. Smith, J. E., N. Mohandas and S. B. Shohet, "Variability in Erythrocyte Deformability Among Various Mammals", *American Journal of Physiology-heart and Circulatory Physiology*, Vol. 236, No. 5, pp. H725–H730, 1979.

131. Omorphos, S., C. M. Hawkey and C. Rice-Evans, "The Elliptocyte: A Study of the Relationship Between Cell Shape and Membrane Structure Using the Camelid Erythrocyte as a Model.", *Comparative Biochemistry and Physiology. B, Comparative Biochemistry*, Vol. 94, No. 4, pp. 789–795, 1989.

132. Perk, K., "The Camel's Erythrocyte", *Nature*, Vol. 200, No. 4903, pp. 272–273, 1963.

133. Perk, K., Y. Frei, A. Herz *et al.*, "Osmotic Fragility of Red Blood Cells of Young and Mature Domestic and Laboratory Animals.", *American Journal of Veterinary Research*, Vol. 25, pp. 1241–1248, 1964.

134. Perk, K., "Osmotic Hemolysis of the Camel's Erythrocytes. I. a Microcinematographic Study", *Journal of Experimental Zoology*, Vol. 163, No. 3, pp. 241–246, 1966.

135. Fowler, M., *Medicine and Surgery of Camelids*, John Wiley & Sons, 2011.

136. Hoter, A., S. Rizk and H. Y. Naim, "Cellular and Molecular Adaptation of Arabian Camel to Heat Stress", *Frontiers in Genetics*, Vol. 10, p. 588, 2019.

137. Yagil, R., U. Sod-Moriah and N. Meyerstein, "Dehydration and Camel Blood.

Ii. Shape, Size, and Concentration of Red Blood Cells", *American Journal of Physiology-legacy Content*, Vol. 226, No. 2, pp. 301–304, 1974.

138. Macfarlane, W., R. Morris, B. Howard *et al.*, "Turn-over and Distribution of Water in Desert Camels, Sheep, Cattle and Kangaroos.", *Nature*, Vol. 197, pp. 270–271, 1963.

139. Warda, M., R. Zeisig *et al.*, "Phospholipid-and Fatty Acid-composition in the Erythrocyte Membrane of the One-humped Camel (Camelus Dromedarius) and Its Influence on Vesicle Properties Prepared From These Lipids.", *Deutsche Tieraerztliche Wochenschrift*, Vol. 107, No. 9, pp. 368–373, 2000.

140. Warda, M., A. Prince, H. K. Kim, N. Khafaga, T. Scholkamy, R. J. Linhardt and H. Jin, "Proteomics of Old World Camelid (Camelus Dromedarius): Better Understanding the Interplay Between Homeostasis and Desert Environment", *Journal of Advanced Research*, Vol. 5, No. 2, pp. 219–242, 2014.

141. Long, C. A., "Evolution of Function and Form in Camelid Erythrocytes", *Biophys Bioeng*, 2007.

142. Livne, A. and P. J. Kuiper, "Unique Properties of the Camel Erythrocyte Membrane", *Biochimica Et Biophysica Acta (BBA)-biomembranes*, Vol. 318, No. 1, pp. 41–49, 1973.

143. Eitan, A., B. Aloni and A. Livne, "Unique Properties of the Camel Erythrocyte Membrane: Ii. Organization of Membrane Proteins", *Biochimica Et Biophysica Acta (BBA)-biomembranes*, Vol. 426, No. 4, pp. 647–658, 1976.

144. Khodadad, J. K. and R. S. Weinstein, "The Band 3-rich Membrane of Llama Erythrocytes: Studies on Cell Shape and the Organization of Membrane Proteins", *The Journal of Membrane Biology*, Vol. 72, No. 3, pp. 161–171, 1983.

145. Ralston, G. B., "Proteins of the Camel Erythrocyte Membrane", *Biochimica Et*

Biophysica Acta (BBA)-biomembranes, Vol. 401, No. 1, pp. 83–94, 1975.

146. Condrea, E., Z. Mammon, S. Aloof and A. De Vries, "Susceptibility of Erythrocytes of Various Animal Species to the Hemolytic and Phospholipid Splitting Action of Snake Venom", *Biochimica Et Biophysica Acta (BBA)-specialized Section on Lipids and Related Subjects*, Vol. 84, No. 4, pp. 365–375, 1964.

147. Joshua, H. and J. Ishay, "The Haemolytic Properties of the Oriental Hornet Venom", *Acta Pharmacologica Et Toxicologica*, Vol. 33, No. 1, pp. 42–52, 1973.

148. Turner, J. C., H. M. Anderson and C. P. Gandal, "Comparative Liberation of Bound Phosphatides From Red Cells of Man, Ox, and Camel.", *Proceedings of the Society for Experimental Biology and Medicine*, Vol. 99, No. 3, pp. 547–550, 1958.

149. Windberger, U., R. Auer, M. Seltenhammer, G. Mach and J. A. Skidmore, "Near-newtonian Blood Behavior–is It Good to Be a Camel?", *Frontiers in Physiology*, Vol. 10, p. 906, 2019.

150. Ashkin, A., J. M. Dziedzic, J. E. Bjorkholm and S. Chu, "Observation of a Single-beam Gradient Force Optical Trap for Dielectric Particles", *Optics Letters*, Vol. 11, No. 5, pp. 288–290, 1986.

151. Gieseler, J., J. R. Gomez-Solano, A. Magazzù, I. P. Castillo, L. P. García, M. Gironella-Torrent, X. Viader-Godoy, F. Ritort, G. Pesce, A. V. Arzola *et al.*, "Optical Tweezers-from Calibration to Applications: a Tutorial", *Advances in Optics and Photonics*, Vol. 13, No. 1, pp. 74–241, 2021.

152. McCauley, M. J. and M. C. Williams, "Mechanisms of Dna Binding Determined in Optical Tweezers Experiments", *Biopolymers: Original Research on Biomolecules*, Vol. 85, No. 2, pp. 154–168, 2007.

153. Lincoln, B., F. Wottawah, S. Schinkinger, S. Ebert and J. Guck, "High-

throughput Rheological Measurements with an Optical Stretcher", *Methods in Cell Biology*, Vol. 83, pp. 397–423, 2007.

154. Guck, J., R. Ananthakrishnan, H. Mahmood, T. J. Moon, C. C. Cunningham and J. Käs, "The Optical Stretcher: A Novel Laser Tool to Micromanipulate Cells", *Biophysical Journal*, Vol. 81, No. 2, pp. 767–784, 2001.

155. Rancourt-Grenier, S., M.-T. Wei, J.-J. Bai, A. Chiou, P. P. Bareil, P.-L. Duval and Y. Sheng, "Dynamic Deformation of Red Blood Cell in Dual-trap Optical Tweezers", *Optics Express*, Vol. 18, No. 10, pp. 10462–10472, 2010.

156. Bareil, P. B., Y. Sheng, Y.-Q. Chen and A. Chiou, "Calculation of Spherical Red Blood Cell Deformation in a Dual-beam Optical Stretcher", *Optics Express*, Vol. 15, No. 24, pp. 16029–16034, 2007.

157. Jess, P., V. Garcés-Chávez, D. Smith, M. Mazilu, L. Paterson, A. Riches, C. Herrington, W. Sibbett and K. Dholakia, "Dual Beam Fibre Trap for Raman Microspectroscopy of Single Cells", *Optics Express*, Vol. 14, No. 12, pp. 5779–5791, 2006.

158. Sehgal, H., T. Aggarwal and M. Salapaka, "Characterization of Dual Beam Optical Tweezers System Using a Novel Detection Approach", *2007 American Control Conference*, pp. 4234–4239, IEEE, 2007.

159. Ott, D., S. N. S. Reihani and L. B. Oddershede, "Crosstalk Elimination in the Detection of Dual-beam Optical Tweezers by Spatial Filtering", *Review of Scientific Instruments*, Vol. 85, No. 5, p. 053108, 2014.

160. Rao, S., Š. Bálint, B. Cossins, V. Guallar and D. Petrov, "Raman Study of Mechanically Induced Oxygenation State Transition of Red Blood Cells Using Optical Tweezers", *Biophysical Journal*, Vol. 96, No. 1, pp. 209–216, 2009.

161. Wood, B. R., L. Hammer and D. McNaughton, "Resonance Raman Spectroscopy

Provides Evidence of Heme Ordering Within the Functional Erythrocyte", *Vibrational Spectroscopy*, Vol. 38, No. 1-2, pp. 71–78, 2005.

162. Raj, S., M. Wojdyla, M. M. Sanchez and D. Petrov, "Force and Raman Spectroscopy of Single Red Blood Cell", *Biophotonics: Photonic Solutions for Better Health Care III*, Vol. 8427, p. 842712, International Society for Optics and Photonics, 2012.

163. Liu, R., Z. Mao, D. L. Matthews, C.-S. Li, J. W. Chan and N. Satake, "Novel Single-cell Functional Analysis of Red Blood Cells Using Laser Tweezers Raman Spectroscopy: Application for Sickle Cell Disease", *Experimental Hematology*, Vol. 41, No. 7, pp. 656–661, 2013.

164. Deng, J., Q. Wei, M. Zhang, Y. Wang and Y. Li, "Study of the Effect of Alcohol on Single Human Red Blood Cells Using Near-infrared Laser Tweezers Raman Spectroscopy", *Journal of Raman Spectroscopy: an International Journal for Original Work in All Aspects of Raman Spectroscopy, Including Higher Order Processes, and Also Brillouin and Rayleigh Scattering*, Vol. 36, No. 3, pp. 257–261, 2005.

165. Wesełucha-Birczyńska, A., M. Kozicki, J. Czepiel, M. Łabanowska, P. Nowak, G. Kowalczyk, M. Kurdziel, M. Birczyńska, G. Biesiada, T. Mach *et al.*, "Human Erythrocytes Analyzed by Generalized 2D Raman Correlation Spectroscopy", *Journal of Molecular Structure*, Vol. 1069, pp. 305–312, 2014.

166. Siamwiza, M. N., R. C. Lord, M. C. Chen, T. Takamatsu, I. Harada, H. Matsuura and T. Shimanouchi, "Interpretation of the Doublet at 850 and 830 cm^{-1} in the Raman Spectra of Tyrosyl Residues in Proteins and Certain Model Compounds", *Biochemistry*, Vol. 14, No. 22, pp. 4870–4876, 1975.

167. Naseer, K., A. Amin, M. Saleem and J. Qazi, "Raman Spectroscopy Based Differentiation of Typhoid and Dengue Fever in Infected Human Sera", *Spectrochimica Acta Part A: Molecular and Biomolecular Spectroscopy*, Vol. 206, pp. 197–201, 2019.

168. Osman, A. M. and M. M. S. El Khatim, "Polysaccharidases of the Camel (Camelus Dromedarius) Intestine and Pancreas", *Comparative Biochemistry and Physiology Part A: Physiology*, Vol. 69, No. 3, pp. 429–436, 1981.

169. Virkler, K. and I. K. Lednev, "Raman Spectroscopic Signature of Blood and Its Potential Application to Forensic Body Fluid Identification", *Analytical and Bioanalytical Chemistry*, Vol. 396, No. 1, pp. 525–534, 2010.

170. Parlatan, U., M. T. Inanc, B. Y. Ozgor, E. Oral, E. Bastu, M. B. Unlu and G. Basar, "Raman Spectroscopy as a Non-invasive Diagnostic Technique for Endometriosis", *Scientific Reports*, Vol. 9, 2019.

APPENDIX A: CODE FOR THE GUI

```
function varargout = PreProcess2(varargin)
% Begin initialization code - DO NOT EDIT
gui_Singleton = 1;
gui_State = struct('gui_Name',       mfilename, ...
                   'gui_Singleton',  gui_Singleton, ...
                   'gui_OpeningFcn', @PreProcess2_OpeningFcn,
                      ...
                   'gui_OutputFcn',  @PreProcess2_OutputFcn,
                      ...
                   'gui_LayoutFcn',  [] , ...
                   'gui_Callback',   []);
if nargin && ischar(varargin{1})
    gui_State.gui_Callback = str2func(varargin{1});
end

if nargout
    [varargout{1:nargout}] = gui_mainfcn(gui_State, varargin
       {:});
else
   gui_mainfcn(gui_State, varargin{:});
end
% End initialization code - DO NOT EDIT

% --- Executes just before PreProcess2 is made visible.
function PreProcess2_OpeningFcn(hObject, eventdata, handles,
   varargin)

 global file   root

```

```
26 [handles.calibrated_x, handles.intensity] = calibrate(handles.
      data , 0.03);
27 handles.C =[handles.calibrated_x, handles.intensity];
28
29 axes(handles.CalibratedData);
30 plot(handles.C(:,1),handles.C(:,2));
31 path = sprintf('%s\\cal\\%s', root,file);
32 dlmwrite(path,handles.C)
33 guidata(hObject, handles)
34
35 function Delete_Callback(hObject, eventdata, handles)
36 handles.listbox.String = {'Listbox'};
37 global ChooseListbox
38
39 %getting the values for the selected file names
40 option = get(handles.listbox,'Value');
41
42 %if there is nothing to delete, nothing happens
43 if (isempty(option) == 1 || option(1) == 0 || isempty(
      ChooseListbox))
44     return
45 end
46
47 %erases the contents of highlighted item in data array
48 ChooseListbox(option) = [];
49
50 %updates the gui, erasing the selected item from the listbox
51 set(handles.listbox,'String',ChooseListbox);
52
53 %moves the highlighted item to an appropiate value or else
      will get error
```

```
54 if option(end) > length(ChooseListbox)
55     set(handles.listbox,'Value',length(ChooseListbox));
56 end
57
58 % Update handles structure
59 guidata(hObject, handles);
60
61 % --- Executes on selection change in listbox.
62 function listbox_Callback(hObject, eventdata, handles)
63
64 % --- Executes on slider movement.
65 function slider1_Callback(hObject, eventdata, handles)
66
67 % --- Executes during object creation, after setting all
     properties.
68 function slider1_CreateFcn(hObject, eventdata, handles)
69 global root file
70 if isequal(get(hObject,'BackgroundColor'), get(0,'
     defaultUicontrolBackgroundColor'))
71     set(hObject,'BackgroundColor',[.9 .9 .9]);
72 end
73 guidata(hObject, handles);
74
75 % --- Executes on button press in Tol.
76 function Tol_Callback(hObject, eventdata, handles)
77 global tolfile
78 [filename, pathname] = uigetfile2( ...
79 {  '*.asc','ASCII-files (*.mat)';  ...
80    '*.*',  'All Files (*.*)'}, ...
81    'File Selector', ...
82    'MultiSelect', 'on');
```

```
83
84  tolfile = dlmread(fullfile(pathname, filename));
85  set(handles.OpenTolFile, 'String', filename);
86  guidata(hObject, handles);
87
88  function CalibSpec_Callback(hObject, eventdata, handles)
89  global filename pathname root file tolfile
90  folder = sprintf('%s\\cal',root);
91
92  handles.SepCal = zeros(length(handles.data),2);
93  handles.SepCal(:,2) = handles.data(:,2);
94  handles.SepCal(:,1) = tolfile(:,1);
95
96  [im,newInt] = AxisCorr2(handles.SepCal);
97
98  handles.CalSpec(:,1) = im' ;
99  handles.CalSpec(:,2) = newInt ;
100
101 axes(handles.CalibratedData);
102 plot(handles.CalSpec(:,1), handles.CalSpec(:,2));
103
104 inputFile = fullfile(folder, filename);
105 dlmwrite(inputFile, handles.CalSpec);
106 guidata(hObject, handles);
107
108 % --- Executes on button press in ClearAxes.
109 function ClearAxes_Callback(hObject, eventdata, handles)
110 cla(); %clear axis function
111 guidata(hObject, handles);
112
113 % --- Executes during object creation, after setting all
```

```
    properties.
function listbox_CreateFcn(hObject, eventdata, handles)

if ispc && isequal(get(hObject,'BackgroundColor'), get(0,'
    defaultUicontrolBackgroundColor'))
     set(hObject,'BackgroundColor','white');
end

function Open_Callback(hObject, eventdata, handles)
global n filename pathname root  file

[filename, pathname, filterindex] = uigetfile2( ...
{  '*.asc','ASCII-files (*.mat)';  ...
   '*.*',  'All Files (*.*)'}, ...
   'File Selector', ...
   'MultiSelect', 'on');
root = pathname(1:end-4);
filename2 = cellstr(filename);

n = size(filename2,2);

if(n>1)
    [~,name,ext] = fileparts(filename{1});
    if(strcmp(name(1:3), 'tol') || strcmp(name(1:3), 'Tol'))
        file = sprintf('%s%s',name, ext);
    else
        file = sprintf('%s%s',name(1:end-4), ext);
    end

    for i=1:n
        set(handles.listbox, 'String', filename) ;
```

```
143             handles.data(:,2*i-1:2*i)=dlmread(fullfile(pathname,
                    filename{i}));
144             handles.M(:,i+1) =  handles.data(:,2*i);
145             axes(handles.RawData);
146             plot(handles.data(:,2*i-1), handles.data(:,2*i));
147             hold on;
148         end
149         handles.M(:,1) = handles.data(:,1);
150
151     else
152         [~,name,ext] = fileparts(filename);
153         if(strcmp(name(1:3), 'tol') || strcmp(name(1:3), 'Tol'))
154             file = sprintf('%s%s',name, ext);
155         else
156             file = sprintf('%s%s',name(1:end), ext);
157         end
158
159         set(handles.listbox, 'String', filename) ;
160         handles.data=dlmread(fullfile(pathname,filename));
161         axes(handles.RawData);
162         plot(handles.data(:,1),handles.data(:,2));
163         hold on;
164     end
165        dlmwrite('a.txt', handles.data);
166     guidata(hObject, handles);
167
168     function OpenTolFile_Callback(hObject, eventdata, handles)
169     function OpenTolFile_CreateFcn(hObject, eventdata, handles)
170
171     if ispc && isequal(get(hObject,'BackgroundColor'), get(0,'
            defaultUicontrolBackgroundColor'))
```

```
172         set(hObject,'BackgroundColor','white');
173 end
174
175 function Average_Callback(hObject, eventdata, handles)
176 global filename pathname root file
177
178 folder = sprintf('%s\\ort',root);
179 eliminated = eleme(handles.M);
180 handles.AvgInt = mean(eliminated,2);
181 axes(handles.CalibratedData);
182 plot(handles.M(:,1), handles.AvgInt);
183
184 inputFile = fullfile(folder, file);
185 handles.Avg = horzcat(handles.M(:,1), handles.AvgInt);
186 dlmwrite(inputFile, handles.Avg);
187
188 guidata(hObject, handles);
189
190 function bg_Callback(hObject, eventdata, handles)
191 global  filename pathname root file tolfile
192 folder = sprintf('%s\\bg',root);
193
194 handles.X = tolfile(:,1);
195 handles.Y = handles.data(:,2) - tolfile(:,2);
196 handles.bgdata = [handles.X , handles.Y];
197
198 axes(handles.CalibratedData);
199 plot(handles.X, handles.Y);
200
201 inputFile = fullfile(folder, filename);
202 dlmwrite(inputFile, handles.bgdata);
```

```
203
204 guidata(hObject, handles);
205
206 function bc_Callback(hObject, eventdata, handles)
207 global  filename pathname root file tolfile
208
209 folder = sprintf('%s\\bc',root);
210 folder2 = sprintf('%s\\bcbase',root);
211
212 [sub,bc] = autoBG(handles.data,handles.param);
213
214 axes(handles.CalibratedData);
215 plot(handles.data(:,1),sub);
216 xlabel('Raman shift (1/cm)');
217 ylabel('Intesity (counts)');
218
219 figure();
220 plot(handles.data(:,1),handles.data(:,2),'r',handles.data(:,1)
      , bc,'b' );
221 xlabel('BC-Raman shift (1/cm)');
222 ylabel('Intesity (counts)');
223 size(sub);
224 size(handles.data(:,1));
225
226 inputFile = fullfile(folder, filename);
227 dlmwrite(inputFile, [handles.data(:,1) sub]);
228
229 inputFile2 = fullfile(folder2, filename);
230 dlmwrite(inputFile2, [handles.data(:,1) bc]);
231
232 guidata(hObject, handles);
```

```
233
234 function baseParam_Callback(hObject, eventdata, handles)
235 function baseParam_CreateFcn(hObject, eventdata, handles)
236
237 if ispc && isequal(get(hObject,'BackgroundColor'), get(0,'
    defaultUicontrolBackgroundColor'))
238     set(hObject,'BackgroundColor','white');
239 end
240
241 % --- Executes on button press in setBaseParam.
242 function setBaseParam_Callback(hObject, eventdata, handles)
243 handles.param = str2double(get(handles.baseParam, 'String'));
244 handles.inital = str2double(get(handles.init, 'String'));
245 handles.final = str2double(get(handles.fin, 'String'));
246
247 guidata(hObject, handles);
248
249 function normalize_Callback(hObject, eventdata, handles)
250 global filename root n
251 folder = sprintf('%s\\norm',root);
252
253 axes(handles.CalibratedData);
254 for i = 1:n
255     handles.normVal(:,i) = handles.data(:,2*i)./max(handles.
        data(:,2*i));
256     plot(handles.data(:,1),handles.normVal(:,i));
257     xlabel('Raman shift (1/cm)');
258     ylabel('NormalizedIntesity (counts)');
259     hold on
260     inputFile = fullfile(folder, filename);
261     %inputFile = fullfile(folder, filename{i});
```

```
262     dlmwrite(inputFile, [handles.data(:,1) handles.normVal]);
263 end
264
265 guidata(hObject, handles);
266
267 function fin_Callback(hObject, eventdata, handles)
268 function fin_CreateFcn(hObject, eventdata, handles)
269
270 if ispc && isequal(get(hObject,'BackgroundColor'), get(0,'
    defaultUicontrolBackgroundColor'))
271     set(hObject,'BackgroundColor','white');
272 end
273
274 function init_Callback(hObject, eventdata, handles)
275 function init_CreateFcn(hObject, eventdata, handles)
276
277 if ispc && isequal(get(hObject,'BackgroundColor'), get(0,'
    defaultUicontrolBackgroundColor'))
278     set(hObject,'BackgroundColor','white');
279 end
280
281 function bcCorr_Callback(hObject, eventdata, handles)
282
283 global  filename pathname root file tolfile
284
285 folder = sprintf('%s\\bcm',root);
286 folder2 = sprintf('%s\\bcmbase',root);
287
288 handles.bcData=dlmread('base1.txt'); % defined base points are
      used
289 in = find(handles.data(:,1) == handles.inital);
```

```
290 out = find(handles.data(:,1) == handles.final);
291
292 handles.data1 = handles.data(in:out,:); %data1= data-one
293 [correctedData,yy,xData] = bcCorrect(handles.data1,handles.
      bcData);
294
295 axes(handles.CalibratedData);
296 plot(correctedData(:,1),correctedData(:,2));
297 inputFile = fullfile(folder, filename);
298 dlmwrite(inputFile, [correctedData(:,1) correctedData(:,2)]);
299
300 inputFile2 = fullfile(folder2, filename);
301 dlmwrite(inputFile2,[xData yy]);
302
303 guidata(hObject, handles);
```

APPENDIX B: CODE FOR THE EDGE DETECTION

```
% To run this code:
% Put 'AnalysisCode.m', '.log'(from the tweezers) , '
    uigetfile2.m' and 'importfile.m' into the 'images' folder
%pixel calibration
%1 pixel = 0.0698 um
calib = 0.0698;
time_ref = 0;
%choosing the reference photo for rhe calculation of initial
    length
[filename_ref, pathname_ref] = uigetfile(...
    {'*.jpg; *.JPG; *.jpeg; *.JPEG; *.img; *.IMG; *.tif; *.TIF
       ; *.tiff, *.TIFF','Supported Files (*.jpg,*.img,*.tiff
       ,)'; ...
    '*.jpg','jpg Files (*.jpg)';...
    '*.JPG','JPG Files (*.JPG)';...
    '*.jpeg','jpeg Files (*.jpeg)';...
    '*.JPEG','JPEG Files (*.JPEG)';...
    '*.img','img Files (*.img)';...
    '*.IMG','IMG Files (*.IMG)';...
    '*.tif','tif Files (*.tif)';...
    '*.TIF','TIF Files (*.TIF)';...
    '*.tiff','tiff Files (*.tiff)';...
    '*.TIFF','TIFF Files (*.TIFF)'},...
    'MultiSelect', 'on', 'Select reference images');

%choosing the experiment photos
[filename, pathname] = uigetfile(...
    {'*.jpg; *.JPG; *.jpeg; *.JPEG; *.img; *.IMG; *.tif; *.TIF
       ; *.tiff, *.TIFF','Supported Files (*.jpg,*.img,*.tiff
```

```
        ,)'; ...
25      '*.jpg','jpg Files (*.jpg)';...
26      '*.JPG','JPG Files (*.JPG)';...
27      '*.jpeg','jpeg Files (*.jpeg)';...
28      '*.JPEG','JPEG Files (*.JPEG)';...
29      '*.img','img Files (*.img)';...
30      '*.IMG','IMG Files (*.IMG)';...
31      '*.tif','tif Files (*.tif)';...
32      '*.TIF','TIF Files (*.TIF)';...
33      '*.tiff','tiff Files (*.tiff)';...
34      '*.TIFF','TIFF Files (*.TIFF)'},...
35      'MultiSelect', 'on', 'Select images');
36  num=length(filename);
37  images=cell(1,num);
38
39  %a function is created to import log file
40  [file, path] = uigetfile2(...
41      {'*.log','log files (*.log)';},...
42      'MultiSelect', 'on', 'Select .log file');
43  logdata=importfile(file);
44  x = size(logdata);
45
46  logdata_9 = table2array(logdata(1:(x-1),9)); % 9th column of
       log data
47  time =vertcat(time_ref,logdata_9);
48
49  %creating the video writer with a specified fps
50  writerObj = VideoWriter(file);
51  writerObj.FrameRate = 10;
52  open(writerObj);
53  im_length=length(images);
```

```
54 %reading the reference image
55 images_reference=imread(sprintf(filename_ref));
56 images_ref=rgb2gray(images_reference);
57
58 %Converting images to binary images
59 I_reversed_ref = uint8(255) - images_ref;
60 level_ref= graythresh(I_reversed_ref);
61 BW_ref = imbinarize(I_reversed_ref,level_ref);
62 img_fill_ref = imfill(BW_ref,'holes');
63 img_ref = bwareafilt(img_fill_ref, 1);
64
65 %feret diameter calculation for reference images
66 [out2_ref,LM2_ref] = bwferet(img_ref,'MaxFeretProperties');
67 ref_FD = table2array(out2_ref(1,1));
68
69 %reading the images
70 for i=1:length(images)
71 images_raw{i}=imread(sprintf('0001_0%03d_Exp_.tif',i));
72 images{i}=rgb2gray(images_raw{i});
73
74 %Converting images to binary images
75 I_reversed{i} = uint8(255) - images{i};
76 level{i}= graythresh(I_reversed{i});
77 BW{i} = imbinarize(I_reversed{i},level{i});
78 img_fill{i} = imfill(BW{i},'holes');
79 img{i} = bwareafilt(img_fill{i}, 1);
80
81 %feret diameter calculation
82 [out2{i},LM2{i}] = bwferet(img{i},'MaxFeretProperties');
83
84 %max feret diameter calculation
```

```
85  k=imshow(images_raw{i});
86  axis2{i} = k.Parent;
87  maxLabel = max(LM2{i}(:));
88      xmax{i} = [out2{i}.MaxCoordinates{1}(1,1) out2{i}.
            MaxCoordinates{1}(2,1)];
89      ymax{i} = [out2{i}.MaxCoordinates{1}(1,2) out2{i}.
            MaxCoordinates{1}(2,2)];
90
91  %creating frames of the video
92  fer_diam_1{i} = out2{1,i}(:,1);
93  fer_diam_2(i)= table2array(fer_diam_1{i});
94  fer_diam(i)= calib*fer_diam_2(i);
95
96  cetvel=imdistline(axis2{i},xmax{i},ymax{i});  % distance tool
97  setLabelVisible(cetvel,false)   % turn off showing distance in
        terms of pixel
98
99  txt=sprintf('%0.2f um', fer_diam(i));
100 hold on;
101 p1=(xmax{1,i}(1)+xmax{1,i}(2))/2;  %position
102 p2=(ymax{1,i}(1)+ymax{1,i}(2))/2;
103 text(p1,p2,txt,'FontSize',18,'FontWeight','Bold');
104
105 frame2 = getframe;
106 writeVideo(writerObj,frame2);
107 MaxDiam(1,i) = (out2{1,i}(:,1));
108 end
109  close(writerObj);
110
111 FD_matrix =table2array(MaxDiam);
112 init_FD =  FD_matrix(1);
```

```
113 [max_FD,idx_2]  =  max(FD_matrix);
114
115 %To find min FD after relaxation, idx_1 is defined
116 FD_relax_data = FD_matrix(:,idx_2:end);
117 min_FD_relax = min(FD_matrix(:,idx_2:end));
118
119 FD_ref_um = ref_FD*calib;
120 FD_max_um =  max_FD* calib ;
121 FD_min_relax_um =  min_FD_relax *calib;
122
123 %Deformability index with Calibrated lengths
124 DeformIndex = (FD_max_um - FD_ref_um) / FD_ref_um;
125 dlmwrite('DeformIndex.txt', DeformIndex);
126
127 %permanent deformation or Hysteresivity
128 h = FD_min_relax_um / FD_ref_um;
129
130 %FD vs. time
131 initial_cond = [time_ref FD_ref_um];
132 a=time(2:end,1);
133 b=FD_matrix'*calib;
134 c = [a b];
135 t_vs_FD= vertcat(initial_cond,c);
136
137 f1 = figure();
138 plot(t_vs_FD(:,1),t_vs_FD(:,2), '*')
139 xlabel('t(s)')
140 ylabel('Max Feret Diameter (um)')
141 savefig(f1,'t_vs_FD.fig')
142
143 %speed and acceleration calculation
```

```
144 x=t_vs_FD(:,1);
145 y=t_vs_FD(:,2);
146
147 for i=1:(length(t_vs_FD)-1)
148 time_interval(i)= x(i+1)- x(i);
149 space_interval(i) = abs(y(i+1)- y(i));
150 speed(i) = space_interval(i)/time_interval(i);
151 acceleration(i) = speed(i)/(x(i+1)- x(i));
152 end
153
154 speed_acc = [speed' acceleration'];
155
156 f2 = figure();
157 plot(x(2:end,:),speed,'*')
158 xlabel('time (s)')
159 ylabel('speed (um/s)')
160 savefig(f2,'speed.fig')
161
162 f3=figure();
163 plot(x(2:end,:),acceleration,'*')
164 xlabel('time (s)')
165 ylabel('acceleration(um/s^2)')
166 savefig(f3,'acceleration.fig')
167
168 %Result excel
169 ZeroMat = zeros((im_length+2),9);
170 ZeroMat(2:end,1)=t_vs_FD(:,1);
171 ZeroMat(2:end,2)=t_vs_FD(:,2);
172 ZeroMat(2,3)=DeformIndex;
173 ZeroMat(2,4)=h;
174 ZeroMat(2,5)=FD_ref_um;
```

```
175 ZeroMat(2,6)=FD_min_relax_um;
176 ZeroMat(2,7)=FD_max_um;
177 ZeroMat(2:end-1,8)= 'speed';
178 ZeroMat(2:end-1,9)= 'acceleration';
179
180 col_header={'Time','Max Feret Diameter','DI','h','FD_ref_um','
    FD_final_um','FD_max_um', 'speed (um/s)', 'acceleration (um
    /s2)'};
181 file(find(file == '.',1,'last'):end) = [];
182 xlswrite(file,ZeroMat);
183 xlswrite(file,col_header);
```

APPENDIX C:

In this thesis, the texts and images, produced by the author, whose copyrights belong to the publisher, were re-used according to the editorial policy of the publisher.